Dissertation zur Erlangung des Doktorgrades der Fakultät für Chemie und Pharmazie der Ludwig-Maximilians-Universität München

Structure of the *Vibrio cholerae* Type VI secretion tubule at sub-nanometer resolution

Sebastian Alexander Kube

aus

Augsburg, Deutschland

2014

Erklärung:

Diese Dissertation wurde im Sinne von §7 der Promotionsordnung vom 28. November 2011 von Frau Dr. Petra Wendler betreut.

Eidesstattliche Versicherung:

Diese Dissertation wurde eigenständig und ohne unerlaubte Hilfe erarbeitet.

München, _____

Sebastian Kube

Dissertation eingereicht am	03. 12. 2014
1. Gutachterin:	Dr. Petra Wendler
2. Gutachter:	Prof. Dr. Roland Beckmann
Mündliche Prüfung am	06. 02. 2015

Parts of this thesis have been published in:

Sebastian Kube, Nicole Kapitein, Tomasz Zimniak, Franz Herzog, Axel Mogk, Petra Wendler: Structure of the VipA/B Type VI Secretion Complex Suggests a Contraction-State-Specific Recycling Mechanism.

Cell Reports, Volume 8, Issue 1, Pages 20-30, 10 July 2014

Contents

Abstract

The bacterial type VI secretion system is a multicomponent molecular machine directed against eukaryotic host cells and competing bacteria. It consists of a contractile tubule that is attached to a membrane protein complex. Upon tubule contraction, a needle is ejected into target cells to translocate toxic effectors into the cell. Due to structural and functional homologies of several proteins of the secretion system to proteins of contractile bacteriophage tails, the system is generally described as an inverted phage tail. Following this analogy, the secretion process is driven by energy stored in the elongated conformation of the Type VI secretion tubule for which also partial structural homology to bacteriophage tail sheath proteins has been predicted. However, this prediction has not been corroborated by structural data so far. The AAA+ ATPase ClpV plays an important role in the secretion process, as it disassembles the contracted tubule, putatively for recycling of the complex. Even though the binding site for ClpV has been identified in VipB, the molecular mechanism which recruits the ATPase specifically to the contracted tubule is not known yet.

In a collaborative project with PD Dr. Axel Mogk and colleagues at the DKFZ Heidelberg and the group of Dr. Franz Herzog at the Gene Center Munich, we investigate the structure of the *Vibrio cholerae* Type VI secretion tubule consisting of the proteins VipA and VipB. We employ a hybrid methods approach of cryo electron microscopic 3D reconstruction and electron microscopic and biochemical labeling techniques supported by cross-linking mass spectrometry to develop a structural model of VipA and VipB in the tubule. We are able to resolve the three-dimensional structure of the helical VipA/B tubule up to 6 Å which allows us to locate secondary structure elements. We describe the arrangement of VipA and VipB in the asymmetric unit and show that the architecture of the tubule is mainly defined by contacts between C-terminal domains of VipB which are structurally similar to domain IV of viral tail sheath proteins. By comparison to the T4 bacteriophage tail sheath, we suggest that these structurally homologous parts mediate the common function of contraction. Additionally, the VipA/B tubule has been adapted towards efficient recycling of contracted Type VI secretion systems. VipB is equipped with a specific four-helix bundle N-terminal domain which carries the ClpV binding motif. Also for VipA, no correspondency to any other known structural part of a phage-like contractile system is found. We propose that it serves as a chaperone for VipB. Based on the observed structural homologies between the T4 phage tail sheath protein and VipB, we model the elongated state of the VipA/B tubule using known low resolution structures of the elongated T4 phage tail. Furthermore, we suggest a molecular mechanism for Type VI secretion tubule recycling. In the elongated state of the tubule, the VipB N-terminal domain is hidden in the tubule wall, making the ClpV binding motif inaccessible for the ATPase. Therefore, ClpV-mediated recycling of the tubule is restricted to its contracted state.

Zusammenfassung

Das bakterielle Typ-VI-Sekretionssystem ist eine aus vielen unterschiedlichen Teilen bestehende molekulare Maschine, die gegen eukaryotische Wirtszellen und konkurrierende Bakterien gerichtet ist. Sie besteht aus einem kontraktionsfähigen Tubulus, welcher mit einem Komplex aus Membranproteinen verbunden ist. Durch Kontraktion des Tubulus wird eine Nadel in eine Zielzelle gestoßen, um Gifte in die Zelle zu injizieren. Aufgrund von strukturellen und funktionalen Homologien von einigen Proteinen des Sekretionssystems zu Proteinen des kontraktionsfähigen Bakteriophagenschwanzes wird das System allgemein als umgedrehter Phagenschwanz beschrieben. In dieser Analogie wird der Sekretionsprozess durch die in der elongierten Konformation des Typ-VI-Sekretionstubulus gespeicherte Energie angetrieben. Für ihn wurde auch eine teilweise strukturelle Homologie zum Mantelprotein des Bakteriophagenschwanzes vorhergesagt, aber nie durch strukturelle Daten belegt. Die AAA+ ATPase ClpV spielt eine wichtige Rolle im Sekretionsprozess, da sie den kontrahierten Tubulus zerlegt, vermutlich zur Wiederverwertung des Komplexes. Obwohl die ClpV-Bindestelle in VipB bereits identifiziert wurde, ist der molekulare Mechanismus, der die ATPase ausschließlich an kontrahierten Tubuli binden lässt, unbekannt.

In einem Kollaborationsprojekt mit PD Dr. Axel Mogk und Mitarbeitern am DKFZ Heidelberg und der Gruppe von Dr. Franz Herzog am Gen-Zentrum München, untersuchen wir die Struktur des Typ-VI-Sekretionstubulus aus *Vibrio cholerae*, welcher aus den Proteinen VipA und VipB besteht. Wir verbinden in unserem Ansatz die 3D-Rekonstruktion aus kryo-elektronenmikroskopischen Bildern mit elektronenmikroskopischen und biochemischen Markierungsmethoden und entwickeln ein Strukturmodell von VipA und VipB im Tubulus, welches durch den massenspektrometrischen Nachweis chemisch quervernetzter Peptide gestützt wird. Wir können die dreidimensionale Struktur des helikalen VipA/B-Tubulus bis auf 6 Å auflösen, was es uns ermöglicht, Sekundärstrukturelemente zu lokalisieren. Wir beschreiben die Anordnung von VipA und VipB in der asymmetrischen Untereinheit und zeigen, dass die Architektur des Tubulus hauptsächlich durch Kontakte zwischen C-terminalen Domänen von VipB bestimmt wird, welche strukturell der Domäne IV der Mantelproteine des Bakteriophagenschwanzes ähneln. Der Vergleich mit dem Mantel des T4 Bakteriophagenschwanzes, führt uns zu dem Vorschlag, dass diese struktur-homologen Bestandteile die gleiche Funktion in der Kontraktion besitzen. Zusätzlich ist der VipA/B-Tubulus einer effizienten Wiederverwertung des Typ-VI-Sekretionssystems angepasst. VipB besitzt eine spezielle N-terminale Domäne, die aus einem Bündel aus vier Helices besteht und das Erkennungsmotiv für ClpV trägt. Für VipA finden wir ebenfalls keine Entsprechung zu anderen phagen-ähnlichen kontraktionsfähigen Systemen. Unserer Ansicht nach dient es als Chaperon für VipB. Basierend auf den beobachteten Strukturhomologien zwischen dem Mantelprotein des T4 Bakteriophagenschwanzes und VipB, entwerfen wir unter der Ver-

wendung von niedrig aufgelösten Strukturen des elongierten T4 Phagenschwanzes ein Modell des elongierten Zustands des VipA/B-Tubulus. Des Weiteren schlagen wir einen molekularen Mechanismus für die Wiederverwertung des Typ-VI-Sekretionstubulus vor. Im elongierten Zustand des Tubulus ist die N-terminale Domäne von VipB in der Wand des Tubulus versteckt. Daher ist das ClpV-Erkennungsmotiv für die ATPase nicht zugänglich und der Abbau des Tubulus durch ClpV auf seinen kontrahierten Zustand beschränkt.

Acknowledgements

This work would not exist without the guidance, work and support of many people and now it's time to say thank you (many times)!

First of all, I would like to thank Petra Wendler for providing the project for my thesis and for the excellent supervision during the last four years. You are a great mentor and taught me a lot - not only single particle reconstruction but also on scientific life in general. You take a great effort in supporting your students in every way and prepare them well for a scientific career.

Next, it's time to say a big thank you to my fellow PhD students in the Wendler group: Susanne Ciniawsky, Anindya Gosh Roy and Malte Kock. I appreciated the relaxed and open working atmosphere. You always had time for advice and discussions on EM handling and processing and of course also the occasional chat. Not to forget: no lab would ever run without dedicated technicians, therefore a great thanks to Kai Hempel and Julia Wittmann. Also, I have had the opportunity to supervise three students during my thesis, who contributed to this project with great effort - thank you Jana Albrecht, Tobias Hassler and Alexander Schmidt!

The work presented here originated from a collaboration with Axel Mogk, Aleksandra Pietrosiuk and Nicole Kapitein from the DKFZ Heidelberg who provided not only strains and proteins tagged at every imaginable position, but also much intellectual input into the success of this project - thank you very much! I am also grateful to Franz Herzog and Tomasz Zimniak for their excellent mass spectrometry data to support our results.

I thank Roland Beckmann for giving access to the microscopes and the cryo cluster and his whole group, especially Caro Haas, Stephan Wickles and Martin Turk for occasional advice on computational and biochemical issues. Otto Berninghausen and Charlotte Ungewickell took care of the microscopes, provided technical support and most importantly wonderful Titan datasets. A big thank you also to you!

I am grateful to my thesis advisory committee members Roland Beckmann, Daniel Wilson and Naoko Mizuno who accompanied my thesis. Naoko Mizuno also helped a lot to cope with the helical symmetry, thank you very much for this. My special thanks go to Elena Orlova for discussing the processing results and giving valuable advice on improving the resolution of the reconstruction.

My parents and grandparents supported me a lot financially as well as morally during my studies and thesis, for which I am very grateful. Last but not least, I thank Gertrud, for sharing her life with me, cheering me up, when things don't work out and calming me down when I'm stressed out.

1 Introduction

Bacteria employ a variety of secretion systems to interact with their environment and co-inhabiting species. There are seven secretion systems known, with Type I-VI being mainly present in Gram-negative bacteria, while the Type VII secretion system is only used by Gram-positives (Fig. 1.1).

The secretion systems in Gram-negative bacteria can be distinguished on whether they dependent on the contact with another cell (Type III-IV), or if they are contact-independent (Type I-II). The Type I secretion system consists of three components: an ATP binding cassette, a membrane fusion protein in the inner membrane, and an outer membrane protein. They act together to transport substrates, that are recognized by a C-terminal signal sequence [Thomas et al., 2014]. Oppositely, the Type II secretion machinery is rather complex and substrates are transported via the bacterial SecYEG or Tat pathway into the periplasm, before they enter the Type II secretion system. The system itself consists of a bell-shaped outer membrane complex and an inner membrane complex with an associated ATPase [Nivaskumar and Francetic, 2014]. Also, the Type III secretion system is a complex nano-machine employed by pathogenic bacteria to inject effector proteins in an one-step mechanism into eukaryotic cells. It is anchored in both the outer and the inner membrane and proteins are recognized by a N-terminal signaling sequence before being transported in an unfolded state driven by an ATPase [Burkinshaw and Strynadka, 2014, Puhar and Sansonetti, 2014]. In contrast, substrates are not necessarily translocated in an one-step mechanism in the Type IV secretion (T4S) system, as here a small subset of effectors bear N-terminal Sec signal sequences instead of T4S-specific ones and putatively enter the Type IV secretion system in the periplasm. It consists of two membrane protein complexes in the inner and outer membrane that are connected by a stalk, and is energized by three different ATPase complexes [Christie et al., 2014]. The family of Type V secretion systems is heterogenous. All five subclasses have in common that they rely on the Sec translocon to reach the periplasm and the Bam complex is involved in the transport across the outer membrane. The Bam complex helps the proteins to fold into a β barrel shape in the outer membrane. Four of the five subclasses are otherwise autotransporters except Type Vb, which is a two-partner secretion system [van Ulsen et al., 2014]. The Type VI secretion (T6S) system was first characterized in 2006 by Pukatzki et al. and Mougous et al.. It consists of a needle complex inside a contractile

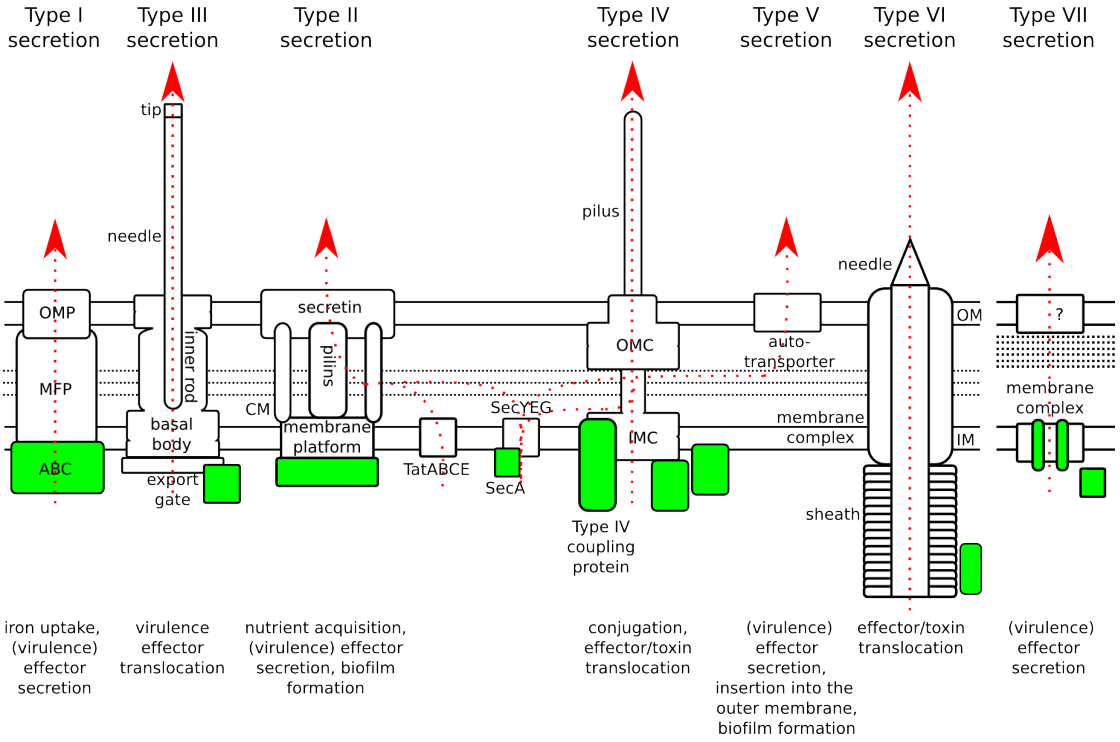

Fig. 1.1: Schematic representation of architecture and function of bacterial secretion systems I - VII. *from left to right:* The Type I secretion system consists of an ATP-binding cassette transporter (*ABC*), a membrane fusion protein (*MFP*) and an outer membrane protein (*OMP*). The Type III secretion system involves a needle complex inside a basal body anchored in the inner (*IM*) and outer membrane (*OM*). Secretion is controlled by an export gate and powered by an ATPase. In the Type II secretion system, a secretin forms a channel across the outer membrane. Translocation involves pilins situated upon an inner membrane complex which is connected by a connecting module (*CM*) to the secretin. Secretion is energized by an ATPase and is Sec or Tat pathway dependent. The Type IV secretion system is formed by an inner membrane complex (*IMC*), an outer membrane / core complex (*OMC*) and a pilus secreted from it to the cell exterior. Some Type IV secretion substrates are Sec-dependent. Three ATPases are associated with the system. Type V secretion system acts via the Sec pathway and an autotransporter activity of secreted substrates or associated proteins. The Type VI secretion system consists of contractile tubule holding a needle complex. The tubule is attached to a membrane complex crossing both membranes and an ATPase is associated to the system. In Typ VII secretion, substrates are transported across the inner membrane by a membrane complex with ATPase activity. Additionally, a cytosolic ATPase is involved. The channel across the outer membrane is not known. ATPase functions are marked in green and secretion pathways are indicated. The main functions of the secretion system are listed underneath.

tubule which is attached to a membrane complex. The system has been investigated functionally and structurally since then. A summary of the current functional and structural data is presented in the following chapter. For the Type VII secretion system which is employed in Gram-positive bacteria, it is not clear whether substrates are translocated in a one-step mechanism directly from the cytoplasm to the cell exterior or if the two membrane are crossed in two steps. Here, secretion is likely energized by an ATPase and substrates are recognized by a helix-turn-helix domain followed by a YxxxD/E motif. [Houben et al., 2014].

1.1 Distribution and organization of the Type VI secretion locus

T6S systems have been found in a quarter of all available genomes of gram-negative bacteria [Das and Chaudhuri, 2003, Schlieker et al., 2005, Bingle et al., 2008, Boyer et al., 2009]. One third of those carry more than one copy of the T6S locus [Boyer et al., 2009]. T6S loci can be divided into three phylogenetically distinct groups present in the Bacteroidetes phylum, in *Francisella* species and in other Proteobacteria [Bingle et al., 2008, Boyer et al., 2009, Bröms et al., 2010, Russell et al., 2014b]. The general proteobacterial T6S system consists of 13 conserved genes [Zheng and Leung, 2007, Bingle et al., 2008, Boyer et al., 2009, Zheng et al., 2011, Lin et al., 2013], which are usually named according to the *tss (type six secretion)* nomenclature *tss*(*A*-*M*), and a subset of *tss-associated genes tag*(*A*-*P*) [Shalom et al., 2007]. However, some parts of the secretion system are referred to by their generic names in the literature and also in this work (see table 1.1). Bioinformatic analysis separates the 13 core genes into two clusters which encode essential proteins that form a membrane complex and a phage-related complex (Fig. 1.2). [Boyer et al., 2009, Zoued et al., 2014].

Table 1.1: Tss/Tag nomenclature and corresponding generic names.

Nomenclature	Generic Name
TssB	VipA
TssC	VipB
TssD	Hcp
TssH	ClpV
TssI	VgrG
TagE	PpkA
TagF	PppA
TagH	Fha

The membrane complex cluster consists of the genes *tssJ*, *tssK*, *tssL* and *tssM*. TssL and TssM are homologues of inner membrane proteins DotU and IcmF of the *Legionella* Type IV secretion system, whereas TssK is a cytoplasmic protein that interacts with members of the membrane and the phage-related complex [Zoued et al., 2013]. TssJ is located in the outer membrane [Felisberto-Rodrigues et al., 2011]. The remaining genes form the phage-related

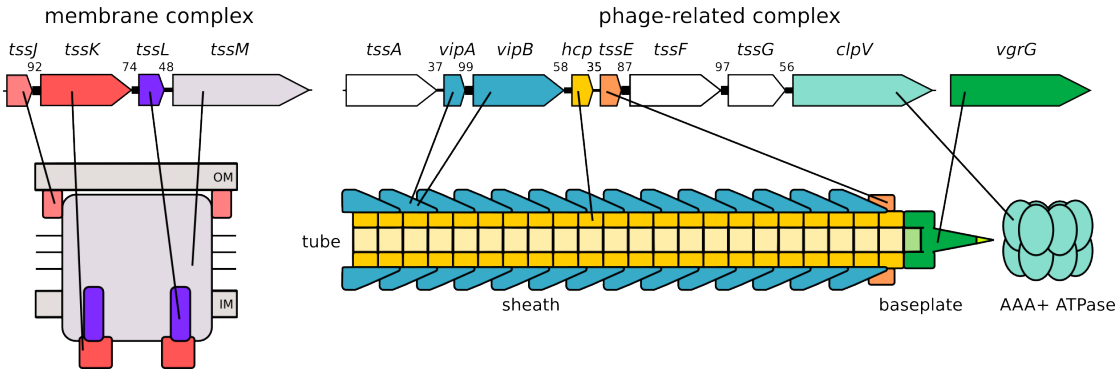

Fig. 1.2: The T6S locus. The 13 T6S core genes can be functionally divided into a membrane (*left*) and a phage-related complex (*right*). The localization of the encoded proteins in the T6S membrane or phage-related complex is indicated; *IM*: inner bacterial membrane, *OM*: outer bacterial membrane. Genes in white color-code have not been functionally characterized yet. The genes are represented according to the consensual genomic organization of the locus as defined by Boyer et al. [2009]. Genes which have a conserved relative transcriptional orientation are connected. The thickness of the connecting line corresponds to the indicated conservation frequency in per cent. The figure has been partially adopted from Boyer et al. [2009].

complex based on homologies of VipB to bacteriophage tail sheath proteins [Lossi et al., 2013], of Hcp to phage tail tube proteins gp19 of T4 phage [Leiman et al., 2009] and gpV_N of λ phage [Pell et al., 2009], of VgrG to the T4 baseplate/tail spike proteins gp27-gp5 [Leiman et al., 2009], and of TssE to T4 baseplate wedge protein gp25 [Leiman et al., 2009, Lossi et al., 2011]. The class II AAA+ ATPase ClpV is not related to phage proteins but is functionally connected to the complex [Schlieker et al., 2005, Bönemann et al., 2009, Basler et al., 2012] and no functional data is available for TssA, TssF and TssG apart from being essential for the system [Zheng and Leung, 2007, Boyer et al., 2009, Zheng et al., 2011, Lin et al., 2013].

The *Francisella* Type VI secretion system ($T6S^{II}$) encoded in the *Francisella* pathogenecity island is clearly distinct from the general proteobacterial Type VI secretion system ($T6S^{I}$) [Bingle et al., 2008, Bröms et al., 2010]. It contains homologues for VipA (IglA), VipB (IglB), Hcp (IglC), VgrG, TssA, TssK, TssF , TssL (DotU) and TssM (IcmF/PdpB) [Bingle et al., 2008, Boyer et al., 2009, Bröms et al., 2010, de Bruin et al., 2011, Russell et al., 2014b]. However, IglF, which has been proposed to take over the role of the AAA+ ATPase ClpV, lacks Walker A and B motifs, and *Francisella* VgrG comprises only the very C-terminus of the gp27-like part (phage baseplate) but the whole gp5-like (phage tail spike) part of regular VgrG proteins [Barker et al., 2009, Bröms et al., 2010]. Recently, a T6S system has been found in the Bacteroidetes phylum which also forms its own phylogenetic group ($T6S^{III}$). Here, homologues for TssA, TssJ, TssM and TssL have not been found which comprises almost the complete membrane complex of the secretion system [Russell et al., 2014b].

1.2 Structural biology of the T6S system

As described before, the T6S apparatus can be divided into a membrane complex part (Fig. 1.3) and a phage-like tubulus [Zoued et al., 2014]. The available structural and functional data suggests that the secretion system resembles an inverted phage tail which is integrated into the outer and the inner bacterial membrane.

1.2.1 The membrane complex

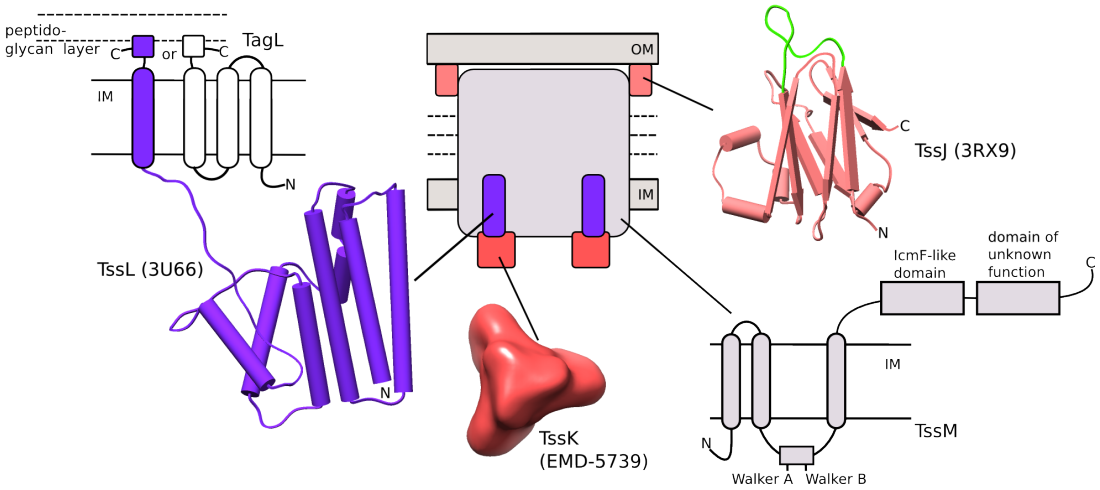

Fig. 1.3: Available structural data of the T6S membrane complex. The membrane complex consists of the proteins TssJ, TssK, TssL and TssM. The lipoprotein TssJ has been crystallized (3RX9). It is anchored in the outer membrane (*OM*) and interacts with TssM via a N-terminal loop (green). TssK is a trimeric cytoplasmic protein (EMD-5739) which interacts with the membrane complex as well as with the phage-like complex. The cytoplasmic domain of TssL (3U66) is anchored via a C-terminal transmembrane domain which is extended in some cases with a periplasmic peptidoglycan binding motif. It is suggested that protein TagL acts as an adaptor to the peptidoglycan layer when this binding motif is not present in TssL. Periplasmic protein TssM interacts with TssJ and is anchored with three transmembrane helices into the inner membrane (*IM*). It carries a Walker A and a Walker B motif in the loop region between transmembrane helix 2 and 3.

The T6S locus encodes for three membrane proteins, TssJ, TssL and TssM. TssJ is a lipoprotein with a transthyretin fold located in the outer membrane and extends into the periplasm [Aschtgen et al., 2008, Felisberto-Rodrigues et al., 2011, Rao et al., 2011, Robb et al., 2013]. It oligomerizes *in vivo* [Rao et al., 2011]. Furthermore it interacts with the periplasmic domain of TssM in an 1:1 ratio via a N-terminal loop region [Felisberto-Rodrigues et al., 2011]. TssM itself is located in the inner membrane, with three N-terminal transmembrane helices and

a big C-terminal periplasmic domain which self-interact in yeast-two-hybrid studies [Ma et al., 2009b]. The *Agrobacterium tumefaciens* TssM contains Walker A and B motifs in between the second and the third transmembrane helix [Ma et al., 2009b, 2012]. The motifs are essential for T6S activity in *A. tumefaciens*, but not in *Edwardsiella tarda* [Zheng and Leung, 2007]. TssM forms a complex with TssL in the membrane [Ma et al., 2009b], which itself is not stable without its binding partner [Bröms et al., 2012]. TssL is anchored with a C-terminal transmembrane helix in the membrane, the N-terminal part faces the cytoplasm [Aschtgen et al., 2012]. In *A. tumefaciens* the C-terminus is extended by an OmpA peptidoglycan-binding motif [Ma et al., 2009b], while in enteroaggregative *Escherichia coli* (EAEC) TssL, such a domain is missing [Durand et al., 2012b]. However, it is suggested that this function is taken over by an adaptor protein called TagL [Aschtgen et al., 2010a,b]. TssL transmembrane helices mediate dimerization of the protein [Durand et al., 2012b]. The cytoplasmic domain consists of two three-helix bundles that are arranged in a hook-like shape [Durand et al., 2012b, Robb et al., 2012]. Negatively charged residues are situated in the cleft of the hook, which are essential for T6S function in *F. tularensis* [Bröms et al., 2012]. Due to the oligomerization properties of all the membrane proteins TssJ, TssL and TssM, it is hypothesized, that they form a channel-like structure across both membranes [Zoued et al., 2014]. The membrane and the phage-related complex is proposed to be connected by the cytoplasmic protein TssK [Zoued et al., 2013]. It forms trimers and interacts with the cytoplasmic part of TssM and TssL as well as with TssA, VipA/B and Hcp.

1.2.2 The phage-like complex

The phage-like complex consists of a hollow needle formed by Hcp, which is surrounded by a contractile sheath consisting of VipA and VipB and which is spearheaded by VgrG and a PAAR repeat protein (Fig. 1.4). A baseplate complex composed of TssE and VgrG is attached to the membrane complex [Zoued et al., 2014]. Hcp oligomerizes into hexameric rings of 85 Å diameter *in vitro* forming a 24-stranded β-barrel on the inside. It is structurally homologous to the tail tube protein of λ phage and T4 phage [Mougous et al., 2006, Leiman et al., 2009, Pell et al., 2009]. *P. aeruginosa* Hcp3 hexamers form tubules *in vitro* and it has been shown that EAEC Hcp1 rings assemble in a head-to-tail fashion *in vivo* [Leiman et al., 2009, Brunet et al., 2014, Douzi et al., 2014]. However, binding between Hcp rings is weak, the k_D was measured to be approximately 7 µM [Douzi et al., 2014]. Hcp directly interacts with VgrG-1 in *A. tumefaciens* [Lin et al., 2013].

A VgrG trimer forms the tail spike. The N-terminal fragment (1-483 aa) of *E. coli* c3393 VgrG has been crystallized [Leiman et al., 2009]. The first 370 residues are structurally homologous to T4 baseplate protein gp27. They fold into four domains of which the first and

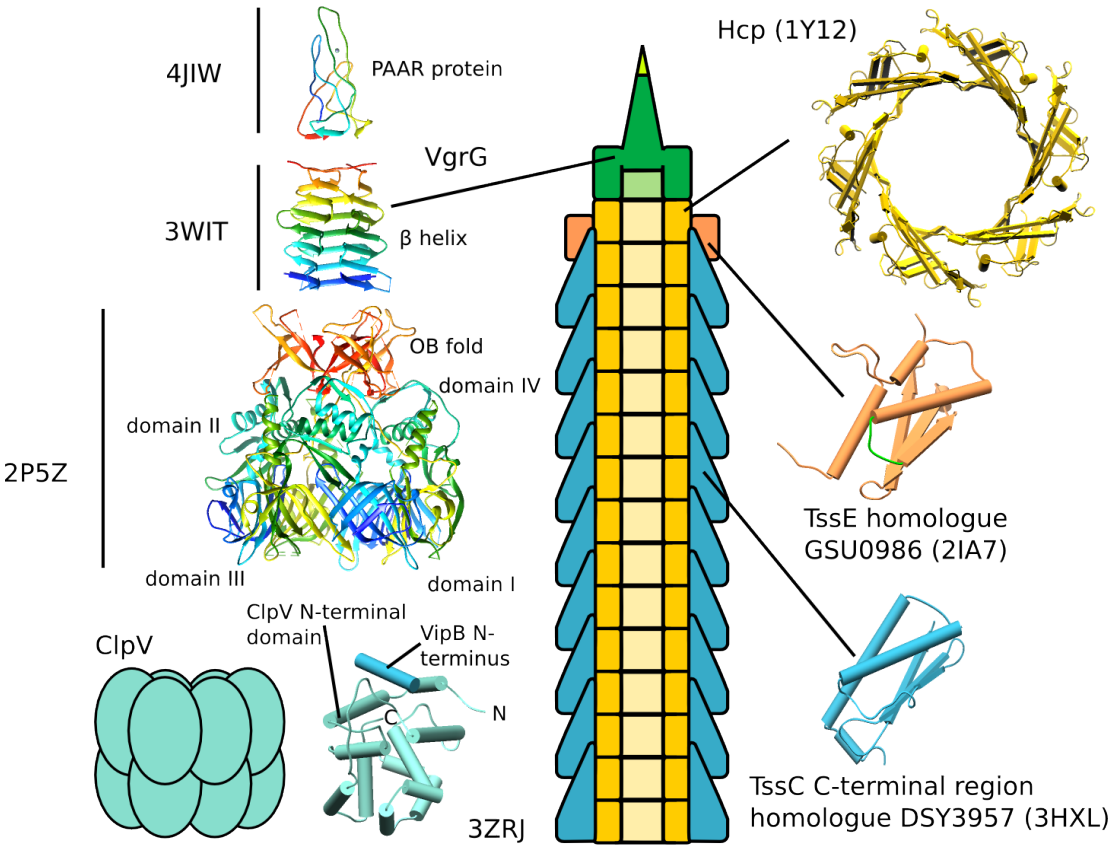

Fig. 1.4: Available structural data of the T6S phage-like complex. The phage-like complex consists of the proteins VipA, VipB, Hcp, VgrG and TssE and putatively also TssA, TssF and TssG. For VipA no structural data is available, but it is predicted that the C-terminal region of VipB is structurally homologous to viral tail sheath proteins, e. g. DSY3957 (3HXL). Hcp (1Y12) is structurally homologous to viral tail tube proteins and forms hexameric rings. The tip of the tube is formed by VgrG which is structurally homologous to proteins forming the baseplate and the tail tip in bacteriophages. Crystal structures of the N-terminal five domains (2P5Z) and a C-terminal β helical fragment (3WIT) have been solved. The tip is sharpened by a PAAR repeat containing protein (4JIW). TssE is structurally homologous to the tail sheath initiator proteins gp25 (2IA7).

the third one are seven-stranded β barrels that assemble into a pseudohexamer in the VgrG trimer. Thereby, they serve as an adapter between the hexameric Hcp ring and the trimeric spike complex. The other two domains connect the adapter to a fifth domain that resembles the oligosaccharide/oligonucleotide-binding (OB)-fold domain of T4 gp5 tail spike protein. However, a lysozyme domain, which directly follows the OB-fold domain in the T4 gp5 protein, is missing in VgrG. The remaining C-terminal part of VgrG trimerizes into a β helical structure with a triangular outline which is capped and sharpened by a PAAR repeat protein with a coordinated zinc ion resembling VCA0105 in *Vibrio cholerae* [Leiman et al., 2009, Shneider et al., 2013, Uchida et al., 2014]. Another protein with homologies to the bacteriophage baseplate is the gp25-like protein TssE [Leiman et al., 2009]. According to structure predictions, it consists of a 3-stranded anti-parallel β sheet with three N-terminal α helices wrapped around it on one side. A conserved glutamate situated in a loop between the third α helix and the first β strand is essential for T6S [Lossi et al., 2011].

In contractile bacteriophages, the needle complex is surrounded by a contractile sheath. This role is taken over by the contractile VipA/B tubule in the T6S system. VipA and VipB stabilize each other and form large tubular complexes [Bönemann et al., 2009, Bröms et al., 2009, Lin et al., 2013]. Heterologously expressed, the tubules are 300 Å wide and have a 12-meric cog-wheel outline when seen from top [Bönemann et al., 2009]. For a homologue in *P. aeruginosa*, also 13-meric top views have been observed [Lossi et al., 2013]. *In vivo,* the VipA/B tubules exist in two conformations, an elongated one with a diameter of 240 Å and a contracted one with right-handed helical ridges (according to a tomogram average) and a diameter similar to the heterologously expressed T6S tubules [Basler et al., 2012]. The findings are reminiscent of the contractile tail of the bacteriophage and indeed, the C-terminal 150 aa of VipB are weakly homologous to the C-terminus of T4 tail sheath protein gp18 [Lossi et al., 2013]. The VipB C-terminal region is also essential for tubule formation but not necessary for interaction with VipA [Aubert et al., 2010]. This interaction is mediated by a long α helix in the C-terminal half of VipA which carries a hydrophobic motif resembling a leucin-zipper [Bröms et al., 2009, Zhang et al., 2013].

V. cholerae VipB has a specific binding motif LLDEIM for the AAA+ ATPase ClpV on an α helix at its N-terminus [Kapitein et al., 2013]. ClpV binds to the motif with its specifically adapted N-terminal domain which carries an additional α0 helix compared to other Hsp100 ATPases. Helices α0 and α1 form a hydrophobic groove into which the N-terminal LLDEIM motif carrying VipB α helix binds. However, in the *P. aeruginosa* H1-T6S system and others, neither the ClpV binding motif is present on VipB nor the hydrophobic groove in the N-terminal domain of ClpV. In these cases, recruitment of ClpV to the tubule is suggested to be mediated by TagJ which binds to the VipA N-terminus [Forster et al., 2014].

1.3 Related phage tail-like structures

Apart from the T6S system and contractile bacteriophages, other phage tail-like structure have been identified in prokaryotes: R-type pyocins, rhapidosomes, the *Photorhabdus luminescens* virulence cassette, the *Serratia entomophila* anti-feeding prophage, the metamorphosis-associated contractile structure (MAC) of *Pseudoalteromonas luteoviolacea.* The latter three are combined phylogenetically in the PLTS (phage-like protein translocation structure) cluster [Sarris et al., 2014].

1.3.1 The minimal contractile bacteriophage tail

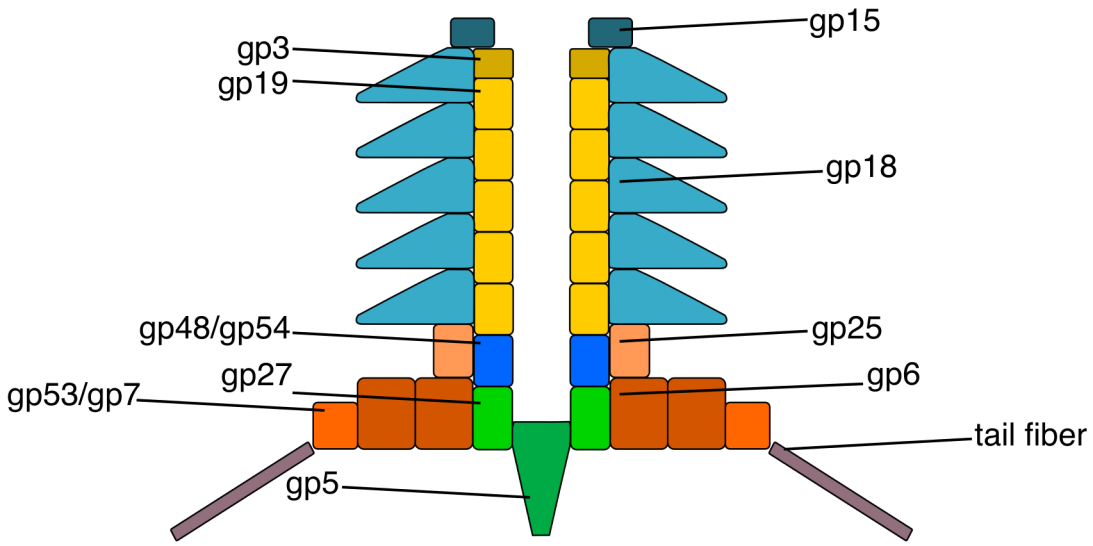

Fig. 1.5: The minimal contractile bacteriophage tail according to Leiman and Shneider [2012]. Proteins gp5 and gp27 form the baseplate hub (green) around which the other baseplate proteins (orange) gp6, gp53/gp7 and gp25 assemble. Tail fibers (brown) are attached to the baseplate. The tail tube (gp19, yellow) assembly is initiated by gp48/gp54 (blue). A tail sheath consisting of gp18 proteins (light blue) wraps around it. Assembly of the tube and the sheath is terminated by gp3 (dark yellow) and gp15 (dark blue), respectively.

Leiman and Shneider [2012] describe a theoretical minimal bacteriophage tail structure (Fig. 1.5). Gp27 and gp5 trimers form a hub-like structure. The gp27 trimer has a donut-like shape with pseudo-hexameric symmetry into which the gp5 trimer is inserted as the needle spike. The hub is surrounded by gp6, gp25 and gp53. Since the structure of gp25 is similar to domain IV of tail sheath protein gp18, it is suggested, that they interact, and that gp25 might even serve as a primer for tail sheath assembly. A hexamer of gp25 surrounds the hub, followed in concentric

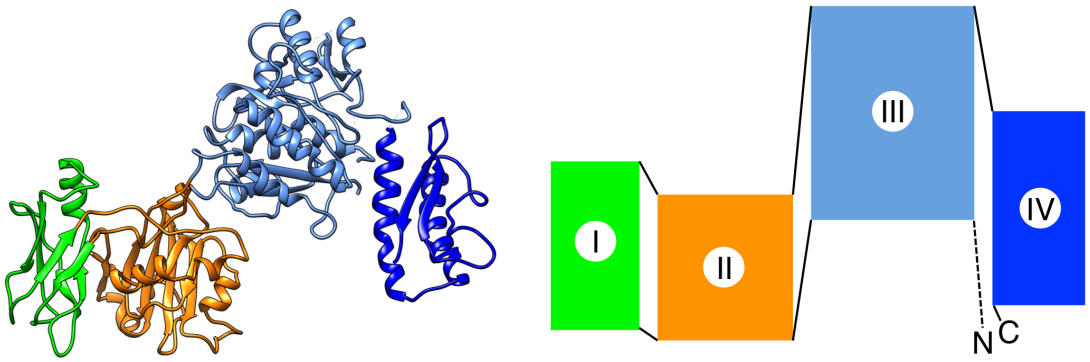

Fig. 1.6: Gp18 fold with three insertion domains. *left:* gp18 structure 3J2N; domain I is colored in green, domain II in orange, domain III in light blue and domain IV in blue. *right:* schematic representation of gp18 fold adapted from Leiman and Shneider [2012].

hexagonal layers by six gp6 dimers and six proteins orthologous to gp53/gp7. The tail fibers are attached to the baseplate. For polymerization of the tube, a tail tube initiator complex consisting of proteins gp48 and gp54 forms upon the gp27 trimer. A tape measure protein with an elongated α helical conformation extends from the initiator complex and determines the length of the tail. The tail tube is formed by hexameric gp19 rings and the tail sheath wraps in six right-handed helical protofilaments around it. All viral tail sheath proteins have a similar fold. They consist of up to four domains. Domain IV is formed by the C-terminal 120 to 150 aa and the N-terminal 20 to 30 aa. Domain III is inserted into domain IV, domain II into III and I into II (Fig. 1.6) [Aksyuk et al., 2011]. Tail tube and sheath are capped by the terminator complex consisting of tube terminator protein gp3 and sheath terminator protein gp15.

1.3.2 R-type pyocins

R-type pyocins resemble head-less contractile bacteriophages [Ishii et al., 1965, Michel-Briand and Baysse, 2002, Leiman and Shneider, 2012], do not contain DNA [Ishii et al., 1965, Michel-Briand and Baysse, 2002, Leiman and Shneider, 2012], and are related to P2 phage tails [Nakayama et al., 2000]. They possess just one tail sheath protein with around 40 kDa molecular weight [Nakayama et al., 2000, Gebhart et al., 2012]. The pyocin gene cluster is present in the genomes of *P. aeruginosa* and other gram-negatives and also gram-positive bacteria and expression is activated via RecA upon DNA damage [Matsui et al., 1993, Williams et al., 2008, Leiman and Shneider, 2012]. Once expression of pyocin genes is induced, one bacterial cell produces up to 200 pyocin particles, which are released by lysis [Scholl et al., 2009]. The target of the released pyocin are determined by their tail fibers as it is the case in bacteriophages [Williams et al., 2008,

Scholl et al., 2009]. When attached to the membrane of their bacterial target, they contract and kill the cell by membrane depolarization [Uratani and Hoshino, 1984]. Pyocins are highly potent toxins as one pyocin particle is sufficient to kill a bacterium. Usually, the *P. aeruginosa* strain that carries the pyocin genes, is resistant to its own toxins [Leiman and Shneider, 2012].

1.3.3 Rhapidosomes

Rhapidosomes have been first described by Lewin [1963] as rod-shaped ribonucleoprotein particles reminiscent of bacteriophage tails in *Saprospira grandis.* They appear in two kinds, as hollow cylinders or cylinders of a similar diameter filled with a smaller cylindrical core. Later rhapidosomes haven been found in *Photobacterium*, *Proteus* and *Pseudomonas,* whereas for some rhapidosomes in *Saprospira* and *Pseudomonas,* a "brush-like end" was observed, that might represent a baseplate complex with tail fibers [Yamamoto, 1967]. For *P. fluorescens*, appearance of rhapidosomes coincided with R-type pyocin production, and those structures co-agglutinated with the pyocin when treated with antiserum. This lead to the conclusion that they represent in fact polysheath structures from pyocin tail sheath protein [Amako et al., 1970]. A more in-depth analysis of rhapidosomes in *Aquaspirillum itersonii* showed that they are formed by at least two proteins of 53 kDa and 29 kDa molecular weight with an additional protein of 18 kDa that co-purified depending on the lysis method [Pazirandeh and Campbell, 1993, Bönemann et al., 2010]. However, the diameter of these rhapidosomes of 170 Å is smaller than the diameter of those described earlier which ranged between 200 and 330 Å [Lewin, 1963, Yamamoto, 1967]. Hence, the term "rhapidosome" might describe a variety of different phage tail-like structures with different function and origin [Leiman and Shneider, 2012].

1.3.4 Phage-like protein translocation structures

Other phage-like structures related to the P2 phage tail are summarized in the PLTS cluster [Sarris et al., 2014]. The anti-feeding prophage (Afp) in *Serratia entomophila* and its homologue in the *Photorhabdus* virulence cassette (PVC) are both pyocin-like toxins which are secreted and directed against insects [Rodou et al., 2010, Leiman and Shneider, 2012]. PVC leads to actin cytoskeleton rearrangements in insect and mammalian haemocytes, while to date Afp only acts on the New Zealand grass grub *Costelytra zealandica* leading to cessation of feeding in larvae [Yang et al., 2006, Hurst et al., 2007]. The gene cluster encode for three tail sheath orthologues with sizes between 40 and 50 kDa, two Hcp orthologues, and orthologues to baseplate proteins, an AAA+ ATPase and a terminator protein [Hurst et al., 2004, Yang et al., 2006, Hurst et al., 2007].

The *S. entomophila* anti-feeding prophage has been characterized biochemically and electron microscopically. The AAA+ ATPase is absolutely necessary for any Afp particle formation, while in the absence of the terminator protein only the baseplate and the tail tube of the particle but no sheath is formed. Furthermore, C-terminal truncation of the terminator protein leads to aberrant tail sheath formation. Finally, the tail sheath contains stoichiometric amounts of two major tail sheath proteins and a third protein in a smaller amount [Rybakova et al., 2013]. The tail sheath shows six-fold rotational symmetry, a unit rise of 8.14 nm and a unit twist of 40.5 ° in a low-resolution cryo EM reconstruction of the elongated Afp particle. When the needle is segmented from the EM density, it demonstrates a unit rise of 4.06 nm and a unit twist of 20.1 °. The isolated needle density can accommodate Hcp rings. Interestingly, a combination of two tail sheath proteins fit into a segmented sheath subunit, even though all of them show approximately ~40 % sequence similarity in the C-terminal regions to T4 tail sheath protein gp18 [Heymann et al., 2013].

The recently described metamorphosis-associated contractile structures (MACs) in *Pseudoalteromonas luteoviolacea* possess just one tail sheath protein of around 62 kDa [Shikuma et al., 2014]. They also resemble pyocins and are released by cell lysis, but in contrast, they form huge hexameric arrays in the cell by connecting with their tail fibers. MACs can induce metamorphosis in marine tube worms by an unknown mechanism.

1.4 T6S effectors

Bacteria can deploy effector proteins directed against bacteria or eukaryots, or in some cases both, via their T6S system. The majority of characterized effectors targets bacteria, only a few types of anti-eukaryotic effectors have been described so far. However, many pathogens are known to mediate virulence against their host by their T6S systems [Coulthurst, 2013]. There is no general signal sequence known, that determines whether an effector is translocated via the T6S, but PAAR repeats and and conserved residue pattern at the N- or C-termini of effectors have been connected to T6S translocation [Shneider et al., 2013, Salomon et al., 2014]. T6S effectors and their use in interbacterial or pathogen-host interactions have been reviewed recently [Durand et al., 2014, Russell et al., 2014a].

Certain VgrG proteins carry C-terminal toxin domains, such as the VgrG1 protein of *V. cholerae* which carries a C-terminal domain homologous to the actin cross-linking domain (ACD) of the *V. cholerae* toxin RtxA and cross-links actin *in vivo* after endocytosis of *V. cholerae* cells [Pukatzki et al., 2007, Ma et al., 2009a]. The ACD is connected to the VgrG1 via a 100 aa disordered linker and cross-links G-actin in the presence of ATP and magnesium ions [Durand et al., 2012a]. By reducing the amount of G-actin in the cell, less bacteria can be phagocy-

tosed by macrophages, until phagocytosis is completely inhibited. As a consequence, with the sacrifice of few bacterial cells, the main *V. cholerae* population is saved from the phagocytic cell [Satchell, 2009]. An *Aeromonas hydrophila* CTD of VgrG1 also interferes with the actin cytoskeleton. The CTD is a vegetative insecticidal protein (VIP-2) domain that causes ADP-ribosylation of actin. HeLa cells cultivated in direct contact with *A. hydrophila* with a functional T6S show cell rounding and ectopic expression of VgrG1 in those cells causes apoptosis [Suarez et al., 2010]. *V. cholerae* VasX is an VgrG-independent effector with anti-eukaryotic activity and putatively secreted directly via the Hcp needle. It possibly targets phosphaditylinositol phosphate-dependent pathways as it contains a N-terminal pleckstrin homology domain and interacts with acidic phospholipids and phosphaditylinositol phosphates [Miyata et al., 2011]. Furthermore, it is also an antibacterial toxin, which forms pores in the inner membrane when present in the periplasm [Zheng et al., 2011, Miyata et al., 2013b]. Other bifunctional T6S toxins are PldA and PldB of *Pseudomonas aeruginosa* with phospholipase D (pld) activity [Russell et al., 2013, Jiang et al., 2014]. PldA is delivered by the H3-T6S and PldB by the H2-T6S system of *P. aeruginosa*, both attack the inner bacterial membrane from the periplasmic side by hydrolyzing phospholipids into the head group and phosphatidic acid. However, PldA and PldB are also promoting bacterial invasion of eukaryotic cells by activation of the PI3K/Akt pathway without being cytotoxic themselves [Jiang et al., 2014].

Antibacterial T6S effectors are far better characterized. Generally they are distinguished by their known target, which is to date the cell wall, the membrane or the DNA, and their enzymatic activity. In the bacterial genome, they are generally bicistronically encoded as toxin-antitoxin pairs to protect bacteria from their own effectors [Russell et al., 2011, Durand et al., 2014]. However, orphan antitoxin (immunity) proteins are often retained in the bacterial genome [Russell et al., 2012]. The first antibacterial effectors have been identified in *P. aeruginosa* as either muramidases/glycoside hydrolases ($Tge1^{PA}$) and or amidases ($Tae1^{PA}$) that degrade the periplasmic murein layer [Hood et al., 2010, Russell et al., 2011, Whitney et al., 2013]. In this case, the corresponding immunity proteins do not protect the cell from the produced toxins, but from T6S attacks of their own species, as $Tge1^{PA}$ and $Tae1^{PA}$ are directly exported from the cytoplasm of the attacker into the target periplasm [Russell et al., 2011]. Tge family enzymes can be divided into three, the Tae family into four phylogenetic clades with differing enzymatic activity [Russell et al., 2012, Whitney et al., 2013]. Also CTDs of VgrG proteins can possess peptidoglycan hydrolysis activity. VgrG3 of *V. cholerae* is equipped with a chitosanase CTD and additionally with a peptidoglycan binding domain which putatively retains the protein attached to the murein layer [Brooks et al., 2013, Dong et al., 2013, Jiang et al., 2014].

Complementary to effectors attacking the murein layer, there are also enzymes targeting the bacterial membrane translocated by the T6S system. They form five phylogenetic clades, of

which the first four (Tle1-4) possess a GXSXG motif common for lipases and esterases and the fifth one (Tle5) a dual HxKxxxxD motif typical for phospholipase D enzymes [Russell et al., 2013]. Some of them do not only target the inner bacterial membrane but also act as anti-eukaryotic effectors (see above). This is also the case for VasX, which is predicted to resemble pore-forming colicin and causes leakage of the inner membrane when artificially targeted to the periplasm of VasX-producing cells [Miyata et al., 2013b].

Apart from those described before, there are also T6S effectors which are active in the cytoplasm [Hood et al., 2010, Fritsch et al., 2013]. Two Type VI effectors RhsA and RhsB in *Dickeya dadanti* target bacterial DNA with their C-terminal nuclease domains [Koskiniemi et al., 2013]. They also contain rearrangement hot-spot/tyr-asp (Rhs/YD) repeats that are associated with other toxic effectors such as the ABC toxin complexes where they are proposed to act as a protective capsule for an unfolded cytotoxic effector domain [Busby et al., 2013]. Furthermore, the Tde effector family in *A. tumefaciens* possesses DNase activity *in vivo,* that confers an intra- and interspecies competitive advantage in plant colonization [Ma et al., 2014]. Nuclease domains are also predicted in other T6S effectors [Salomon et al., 2014, Whitney et al., 2014].

1.5 Regulation of T6S expression

Bacteria often tightly control the expression of T6S genes depending on e. g. quorum sensing [Ishikawa et al., 2009], biofilm formation [Aubert et al., 2008], iron [Brunet et al., 2011], temperature [Pieper et al., 2009, Zhang et al., 2011], osmolarity and salinity [Ishikawa et al., 2012], and pH [Chakraborty et al., 2010]. A more comprehensive list can be found in Miyata et al. [2013a]. Two of the more prominent pathways regulating T6S expression are described in detail: the activation of alternative transcriptional initiator σ^{54} /RpoN by VasH in *V. cholerae* and the Gac/Rsm pathway in *P. aeruginosa* [Silverman et al., 2012].

VasH is encoded by the T6S cluster in *V. cholerae* and essential for T6S mediated killing of amoebae ([Pukatzki et al., 2006] and bacterial cells [Zheng et al., 2011]. Furthermore, transposon insertion in the *rpoN* locus attenuates virulence against amoebae [Pukatzki et al., 2006]. RpoN binds together with VasH to T6S promotor sequences and is required for transcription. Additionally, VasH shows auto-phosphorylation *in vitro* which is indicative for phosphorylation by sensor kinases *in vivo* [Bernard et al., 2011]. To act as a bacterial enhancer binding protein, VasH must hydrolyze ATP to remodel the RNA-Polymerase-RpoN holoenzyme [Bush and Dixon, 2012]. Kitaoka et al. [2011] showed that both Walker A and B motifs, and a C-terminal DNA-binding helix-turn-helix domain of VasH is needed for transcriptional activation. However, there is a discrepancy, whether VasH controls the large T6S cluster and the smaller *hcp* operons [Bernard et al., 2011] or only the latter ones [Dong and Mekalanos, 2012].

In *P. aeruginosa ΔretS* strain expression of T6S cluster HSI-1 is activated [Mougous et al., 2006]. RetS inhibits auto-phosphorylation of GacS in the GacS/GacA two-component system [Goodman et al., 2004, 2009, Silverman et al., 2012]. GacA activates expression of sRNA RsmZ that sequesters the protein RsmA, which otherwise would inhibit translation of T6S transcripts [Ventre et al., 2006, Lapouge et al., 2008, Silverman et al., 2012].

Considering the expression of the T6S system, there are bacteria with a constitutive active expression of T6S genes such as *V. cholerae* strain V52 while others such as *P. aeruginosa* tightly regulate the system and signaling pathways have to be impaired to get T6S protein expression in the lab. It is postulated, that bacteria with a constitutively expressed T6S have evolved to employ the system mainly in inter-bacterial interactions while a regulation of T6S is needed when interacting inside a host with eukaryotic cells [Miyata et al., 2013a].

1.6 The secretion process

Based on the model of the inverted phage tail and time-lapse fluorescence microscopy of tagged T6S complexes *in vivo* [Basler and Mekalanos, 2012, Basler et al., 2012, Brunet et al., 2013, Kapitein et al., 2013], the T6S secretion process is generally described as a cycle of secretion apparatus assembly, rapid contraction and effector translocation, and at least partial secretion apparatus disassembly (Fig. 1.7).

1.6.1 Tubule assembly

The elongated T6S tubule with the needle complex is attached to a baseplate complex which is located in the membrane. Whether this baseplate exists preformed in the membrane or assembles together with the tubule complex, as well as the signal, which leads to its formation, is not known.

However, a post-translational control mechanism for site-specific T6SS assembly and contraction is proposed for *P. aeruginosa* [Ho et al., 2014]. Here, T6SS formation and activity is dependent on phosphorylation of protein Fha1 (forkhead-associated 1) at Thr-362 by the serine/threonine kinase PpkA. De-phosphorylation by the antagonist phosphatase PppA inhibits T6SS activity [Mougous et al., 2007]. Deletion of Fha inhibits T6SS tubule formation [Kapitein et al., 2013]. PpkA is a membrane-spanning kinase located in the inner membrane which becomes active after auto-phosphorylation and dimerization. Its activity is dependent on the presence of the periplasmic protein TagR and outer membrane lipoprotein TagQ, to which TagR is associated [Hsu et al., 2009, Silverman et al., 2011, Casabona et al., 2013]. Additionally, a complex in the inner membrane reminiscent of bacterial ABC transporters consisting of transmembrane protein TagS and the ATPase TagT is needed for PpkA activation [Casabona et al.,

2013]. "T6S dueling" has been observed in *P. aeruginosa,* in which cells, that have been attacked by another cell with a T6S system, retaliate with their own T6S system in the precise direction of the attack in solid culture [Basler and Mekalanos, 2012]. It is therefore proposed that this temporal and spatial sensing of an assault is conferred by a TagQRST-PpkA/PppA-Fha1 signaling cascade, as co-cultivated *V. cholerae* and *A. baylyi* with an active T6S system are attacked by P. aeruginosa dependent on the expression of TagT [Basler et al., 2013]. How the attack is actually integrated into the system is not known, but the *P. aeruginosa* T6S system is also activated TagT-dependently upon *E. coli* Type IV secretion system mediated conjugation independent of actual gene transfer and by the presence of membrane-disrupting polymyxin B [Ho et al., 2013]. This points towards a disruption of the outer membrane as the initial signal that activates the phosphorylation cascade. In *Serratia marcescens*, the T6S system is also regulated via PpkA/PppA-Fha, but proteins TagQRST are not part of its secretion system which is also the case for many other species [Fritsch et al., 2013]. Furthermore, the T6S system is activated via this pathway in planktonic growth, as a consequence, T6S activation is also independent from cell contacts. Hence, also other signals than membrane rupture seem to be integrated over the PpkA/PppA-Fha cascade (Fig. 1.7 a).

Interestingly, PpkA also directly phosphorylates baseplate complex protein TssL which greatly increases T6S activity in *A. tumefaciens.* Afterwards, Fha binds to the phosphorylated protein, a conformational change is induced in the interacting baseplate complex protein TssM and Hcp recruitment to TssL is greatly enhanced [Lin et al., 2014]. ATP binding to TssM induces a conformational switch and its ATPase activity leads to TssM-TssL-Hcp complex formation [Ma et al., 2009b, 2012]. However, in *E. tarda*, binding of ATP by TssM is not essential for T6S activity [Zheng and Leung, 2007].

The baseplate/tube tip proteins VgrG and VCA0105, need to be present for T6S secretion, presumably as a starting point for the T6S assembly (Fig. 1.7 b) [Shneider et al., 2013, Brunet et al., 2014]. Additionally, Hcp is needed for a proper assembly of VipA and VipB in the elongated form of the T6S tubule [Kapitein et al., 2013, Brunet et al., 2014]. Furthermore, gp25 homologue TssE might be necessary as a primer as it has been discussed for the phage tail [Leiman and Shneider, 2012]. Hcp hexamers form stacks in a head-to-tail fashion and impairment of stack formation inhibits also VipA/B tubule formation [Brunet et al., 2014]. VipA and VipB cannot be stably expressed on their own or when VipA/B binding is impaired, so it is reasonable to assume that the two proteins are incorporated into the tubule as a dimer [Bönemann et al., 2009, Bröms et al., 2009, Aubert et al., 2010]. It is proposed that the needle serves as a template for proper assembly of the T6S sheath. Additionally, the loaded complex is most likely formed in a coordinated fashion in which Hcp hexamers are included into the complex shortly before VipA/B protomers are recruited to the same layer of the growing complex (Fig. 1.7 c,

d) [Zoued et al., 2014]. This is supported by the observation by cryo ET of a putative assembly intermediate of a short loaded T6SS complex [Chang et al., 2014]. T6S tubule assembly is fast, Basler et al. [2012] measured 20 - 30 s µm^{-1} in time lapse fluorescence microscopy recordings. The length of bacteriophage tails is controlled by tape measure proteins [Davidson et al., 2012], but a homologue in the T6S system is not known. Also, observations of T6S systems *in situ* do not argue for a length control as the contractile tubule can span the whole cell diameter [Basler et al., 2012, Kapitein et al., 2013]. The postulation, that T6S needs a tail termination protein like bacteriophages [Zoued et al., 2014], might not be necessary if one assumes a wave-like contraction mechanism in which the contraction moves processively from the cell membrane to the end of the T6S tubule as it is suggested for the T4 phage tail [Leiman et al., 2010].

1.6.2 Contraction and effector translocation

In analogy to *Myoviridae*, the contraction of the T6S tubule is thought to be triggered by a conformational change in the baseplate complex which is also the end point of the described signaling pathway [Leiman et al., 2010, Zoued et al., 2014]. Subsequently, the tubule contracts within at least 5 ms, thereby reducing its length by 45 % and extending its diameter from approximately 240 Å to 300 Å [Basler et al., 2012]. The conserved domains IV and III of viral tail sheath proteins are mainly involved in the contraction process [Aksyuk et al., 2009, Leiman et al., 2010]. Since the VipB C-terminus is predicted to share structural homology with domain IV, it is likely that the contraction of the T6S tubulus resembles that of the bacteriophage tail [Aksyuk and Rossmann, 2011, Lossi et al., 2013]. Here, the contraction process can be described as rigid-body movements of the individual subunits [Aksyuk et al., 2009, Leiman and Shneider, 2012]. However, so far only low resolution structures are available for elongated and contracted phage tails, which makes it difficult to judge whether this postulation holds true [Leiman et al., 2004, Kostyuchenko et al., 2005, Aksyuk et al., 2009, 2011, Effantin et al., 2013, Leiman and Shneider, 2012].

During T4 phage tail contraction, the subunits of one disc of the tubule move radially outwards and rotate approximately 45 ° clockwise in a trajectory parallel to the baseplate. By this movement, the subunits of a subsequent disc get inserted in between the subunits of the first one which widens the inner diameter of the tail sheath. Domain IV of gp18 maintains connectivity in the protofilament during contraction, while the other domains form new contacts increasing the contact area four-fold. The additional contacts provide the enthalpy gain which drives the contraction movement [Aksyuk et al., 2009]. However, there is indirect evidence from spectroscopic data, that the tail sheath secondary structure content changes during contraction of the T4 tail and also of the *P. aeruginosa* R1 pyocin [Venyaminov et al., 1975, Uratani, 1982]. Furthermore, protomers in a protofilament in the viral contractile tail sheath might be linked by

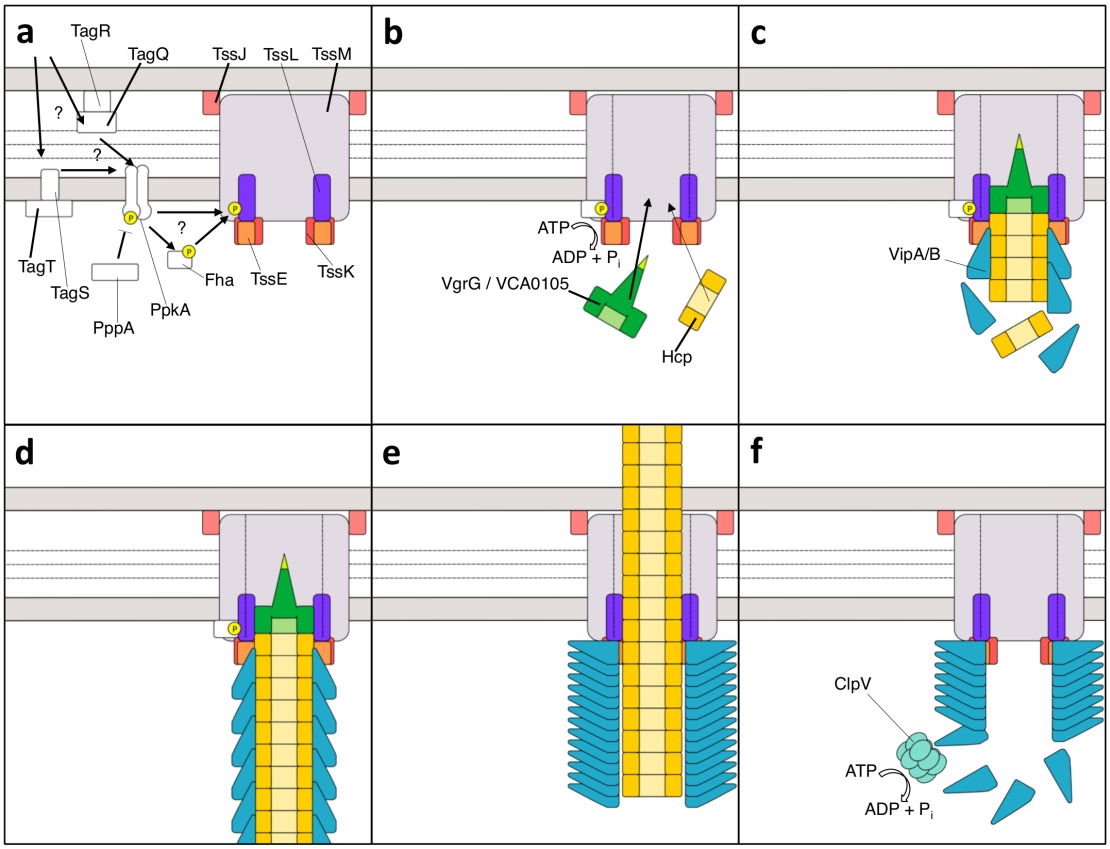

Fig. 1.7: Model for the T6S secretion process. (**a**) Activation of PpkA/PppA-Fha signaling cascade leads to phosphorylation of TssL and binding of Fha. (**b**) This activates ATP hydrolysis in TssM thereby inducing a conformational change and recruitment of VgrG/VCA0105 as well as Hcp to the baseplate complex. (**c**) Needle and VipA/B tubule are assembled in a coordinated manner. (**d**) The loaded complex is ready to contract. (**e**) Contraction of the VipA/B tubule leads to ejection of the needle complex. (**f**) The contracted VipA/B tubule is disassembled by the AAA+ ATPase ClpV.

so called “chain-swapping” in the C-terminal domains of gp18-like proteins as it is observed in a crystal of gp18-like protein DSY3957 (3HXL) [Aksyuk et al., 2011, Leiman and Shneider, 2012]. Here, the N-terminus forms a β sheet with the C-terminal β strands in domain IV of a neighboring DSY3957 protein. By linking the protomers, the contractile machine should gain more stability. Due to the predicted structural homology of domain IV to the VipB-C domain, a similar mechanism has also been suggested for the T6S system [Zoued et al., 2014]. The contraction of the sheath leads to ejection of the needle (Fig. 1.7 e). How the contraction movement is transferred from the T6S tubule to the Hcp needle is not known, yet, mutation of conserved residues at C-terminus of *E. tarda* Hcp, that would be located at the interface between the needle and the surrounding sheath, abrogates T6S secretion [Jobichen et al., 2010].

Effectors are thought to be translocated via the needle complex. The Hcp hexamer has an inner diameter of 40 Å, enough to accommodate small folded or large partially unfolded proteins [Mougous et al., 2006, Zoued et al., 2014]. A putative effector protein co-immuno-precipitated with Hcp in *E. tarda* [Zheng and Leung, 2007] and Silverman et al. [2013] showed that Hcp can act as chaperone and substrate receptor for T6S effectors. Additionally, the tail tip protein VgrG can be functionalized with a C-terminal effector domain [Pukatzki et al., 2007, 2009]. Furthermore, the finding of the PAAR- repeat protein VCA0105 forming the very tip of the T6S needle lead to the Multiple Effector tRanslocation VgrG model (MERV) [Shneider et al., 2013]: T6S effectors are delivered by translocation through the Hcp needle, or the needle proteins VgrG and VCA0105 are functionalized either covalently or non-covalently by additional effector domains or proteins.

1.6.3 Disassembly

The AAA+ ATPase ClpV is recruited to the T6S tubule upon contraction [Basler and Mekalanos, 2012, Kapitein et al., 2013]. It recognizes a special binding motif on VipB and disassembles the VipA/B tubule under ATP consumption within 30 - 60 s (Fig. 1.7 f) [Bönemann et al., 2009, Basler and Mekalanos, 2012, Pietrosiuk et al., 2011, Kapitein and Mogk, 2014]. Also, alternative disassembly pathways mediated by TagJ and VipA homologues are suggested (see 1.2.2). Only VipB is targeted by the ATPase, but the VipA/B protomer quickly re-assembles or the complex is just partially unfolded [Bönemann et al., 2009]. Currently it is not clear, whether individual protomers are recycled into a new loaded T6S tubule or are degraded, but the observation that more than one T6S tubule is formed in a cell, suggests a recycling of protomers [Basler and Mekalanos, 2012, Basler et al., 2012]. Deletion of *clpv* leads to a 90 % loss of T6S antibacterial activity in *V. cholerae*, but the ATPase is not essential [Zheng et al., 2011, Basler et al., 2012]. For example, the *Campylobacter jejuni* T6S lacks ClpV completely [Lertpiriyapong et al., 2012, Bleumink-Pluym et al., 2013].

1.7 Motivation

The current model of the Type VI secretion system is the inverted *Myoviridae* phage tail [Basler et al., 2012]. It is based on the structural homology of the T6S core components Hcp, VgrG, VCA0105 and TssE to contractile bacteriophage proteins forming the tail tube, the needle tip and the baseplate complex [Leiman et al., 2009, Pell et al., 2009, Lossi et al., 2011, Shneider et al., 2013]. Furthermore, the VipA/B tubule which is a functional homologue of the viral contractile tail sheath [Basler et al., 2012], is assumed to be also structurally homologous to the tail sheath protein. This assumption is based on the similar appearance of VipA/B tubules [Bönemann et al., 2009] and the T4 tail sheath [Moody, 1967] in negative stain micrographs of tubule top views [Leiman et al., 2009] and in negative stain side view class averages, on a computational structural homology prediction of the C-terminal part of VipB [Lossi et al., 2013], and on a low resolution cryo-ET average of the contracted VipA/B tubule with right-handed helical ridges [Basler et al., 2012]. The exact architecture of the VipA/B tubule, as well as the structure and arrangement of VipA and VipB in the asymmetric unit are not known yet.

One hallmark of Type VI secretion system is the AAA+ ATPase ClpV [Schlieker et al., 2005]. It is dedicated to the disassembly of contracted VipA/B tubules for recycling by interacting with VipB [Bönemann et al., 2009, Pietrosiuk et al., 2011, Basler and Mekalanos, 2012, Basler et al., 2012, Kapitein et al., 2013]. Generally, a loss of ClpV leads to a reduced Type VI secretion activity and tubule mislocalization [Zheng et al., 2011, Basler and Mekalanos, 2012, Basler et al., 2012, Kapitein et al., 2013].

Additionally, the Type VI secretion system plays an important role in inter-bacterial competition[Basler et al., 2013, Ho et al., 2013, Russell et al., 2014b], thereby enhancing host colonization [Fu et al., 2013, Ma et al., 2014], and can also be directed against eukaryotic cells [Pukatzki et al., 2006, Bröms et al., 2009, Ma et al., 2009a, Aubert et al., 2010, Ma and Mekalanos, 2010, Bröms et al., 2012]. Furthermore, other phage tail-like structures are employed by bacteria in virulence such as the PVC/Afp structures [Yang et al., 2006, Hurst et al., 2007, Rybakova et al., 2013] and R-type pyocins [Michel-Briand and Baysse, 2002]. And finally, there is also little high-resolution structural data on the assembly of phage tails themselves available [Leiman et al., 2004, Kostyuchenko et al., 2005, Aksyuk et al., 2009, 2011, Effantin et al., 2013, Leiman and Shneider, 2012]. This makes the proteins in the contractile machinery an interesting target for research and - in the case of pathogens - drug targeting for which structural data is vital.

Since VipA and VipB proteins could not be crystallized so far due to their tubule-forming nature, their structure is elucidated in the tubule complex by cryo EM. Therefore, *V. cholerae* VipA/B tubules are heterologously expressed in *E. coli* and purified after a protocol established by Bönemann et al. [2009]. The tubules are vitrified and cryo EM data collected which is the

basis for a single particle reconstruction employing helical symmetry [Egelman, 2007b, Clare and Orlova, 2010]. The VipA/B protomer is isolated from the EM density and a structural model obtained in which the ClpV interaction site is localized. The structural model is used to gain insights into the mechanisms behind tubule contraction and recycling.

2 Material and Methods

2.1 Material

2.1.1 Chemicals and reagents

Chemicals and reagents used in this work have been purchased from Carl Roth GmbH & Co. KG (Karlsruhe, Germany), Sigma Aldrich (St. Louis (MO), USA), Merck KGaA (Darmstadt, Germany), Serva Electrophoresis GmbH (Heidelberg, Germany) or VWR (Radnor (PA), USA) unless stated otherwise. Cell culture media components have been purchased from ForMedium (Norfolk, UK).

2.1.2 Strains and plasmids

The genetic background of *E. coli* strains used in this work is listed in table 2.1. *E. coli* strains are presented in table 2.2. Strains provided by the group of A. Mogk at the DKFZ Heidelberg are indicated (*).

Table 2.1: Genotype of *E. coli* strains used in this work.

Strain	Genotype	Source
BL21-DE3	F^- ompT gal dcm lon $hsdS_B(r_B^- m_B^-)$ λ(DE3 [lacI lacUV5-T7 gene 1 ind1 sam7 nin5])	Studier and Moffatt, 1986
DH5α	F^- endA1 glnV44 thi-1 recA1 relA1 gyrA96 deoR nupG Φ80d*lacZ*ΔM15 Δ(*lacZYA-argF*)U169, $hsdR17(r_K^- m_K^+)$, λ–	Grant et al., 1990
MC4100	F^- $[araD139]_{B/r}$ Δ(argF-lac)169* &lambda$^-$ e14-flhD5301 Δ(fruK-yeiR)725 (fruA25)‡ relA1 rpsL150(strR) rbsR22 Δ(fimB-fimE)632(::IS1) deoC1	Peters et al. 2003
XL1	endA1 gyrA96(nal^R) thi-1 recA1 relA1 lac glnV44 F'[::Tn10 $proAB^+$ $lacI^q$ Δ(lacZ)M15] $hsdR17(r_K^- m_K^+)$	Stratagene

Table 2.2: *E. coli* strains used in this work. Indicated (*) strains have been provided by the group of A. Mogk at the DKFZ Heidelberg.

Background	Plasmid	Description	Source
BL21-DE3	pQE21-*N-clpV-vipA-vipB(E375C)*	pQE31 with 5'-region of *clpV* (N-terminal domain), *vipA* and *vipB(E375C)*	Kube et al., 2014
BL21-DE3	pQE21-*N-clpV-vipA-vipB(Q429C)*	pQE31 with 5'-region of *clpV* (N-terminal domain), *vipA* and *vipB(Q429C)*	Kube et al., 2014*
BL21-DE3	pQE21-*N-clpV-vipA-vipB(E375C/Q429C)*	pQE31 with 5'-region of *clpV* (N-terminal domain), *vipA* and *vipB(E375C/Q429C)*	Kube et al., 2014
BL21-DE3	pQE21-*N-clpV-vipA-vipB(P390I)*	pQE31 with 5'-region of *clpV* (N-terminal domain), *vipA* and *vipB(P390I)*	this study
MC4100	pDS56-*clpV*	pDS56 with *clpV*	Bönemann et al., 2009*
XL1	pQE31-*N-clpV-vipA-vipB,* pLacIQ	pQE31 with 5'-region of *clpV* (N-terminal domain), *vipA* and *vipB*	Bönemann et al. 2009*
XL1	pQE31-*N-clpV-vipA-vipB-yfp,* pLacIQ	pQE31 with 5'-region of *clpV* (N-terminal domain), *vipA* and *vipB-yfp*	Kapitein et al. 2013*
XL1	pQE31-*N-clpV(A86C)-vipA-vipB(T27C)*	pQE31 with 5'-region of *clpV(A86C)* (N-terminal domain), *vipA* and *vipB(T27C)*	Kube et al., 2014*
XL1	pQE31-*his-vipA-ha-vipB,* pLacIQ	pQE31, *his-vipA-ha* and *vipB*	Kube et al., 2014*
XL1	pQE31-*N-clpV-vipA-vipBΔC*^{210}, pLacIQ	pQE31, *vipA* and *vipBΔC*^{210}	Kube et al., 2014*
XL1	pQE31-*N-clpV-vipA-vipBΔC*^{367}, pLacIQ	pQE31, *vipA* and *vipBΔC*^{367}	Kube et al., 2014*

2.1.3 DNA primer sequences

DNA primer sequences have been purchased from metabion GmbH (Planegg, Germany) and are presented in table 2.3.

Table 2.3: DNA primer sequences and their annealing temperatures used in the PCR experiment.

name	sequence	annealing temperature
E375C_for	5′- CCA AAT ACC AAA TGT GGC AAA GAA GCG -3′	55°C
E375C_rev	5′- CGC TTC TTT GCC ACA TTT GGT ATT TGG -3′	55°C
P390I_for	5′- TTG GGT ACC CAG CTG ATC TAC ATG ATG ATC -3′	53°C
P390I_rev	5′- GAT CAT CAT GTA GAT CAG CTG GGT ACC CAA -3′	53°C

2.1.4 Antibodies

Antibodies used for Western blot detection and labeling experiments are listed in table 2.4.

Table 2.4: Antibodies used in this work.

antibody	manufacturer
αHis (mouse)	dianova GmbH, Hamburg, Germany
αHA High Affinity	Roche Diagnostics Deutschland GmbH, Mannheim, Germany
α-mouse, HRP-conjugated (rabbit)	Santa Cruz Biotechnology, Inc., Dallas (TX), USA

2.1.5 Proteins

V. cholerae proteins that have been purified by our collaborators A. Mogk and colleagues are presented in table 2.5.

Table 2.5: Proteins from A. Mogk and colleagues used in this study.

Protein	Source
ClpV	Bönemann et al., 2009
His_6-VipA-HA/VipB	Kube et al., 2014
ClpV-N(A86C)/VipA/VipB(T27C)	Kube et al., 2014
VipA/VipB(E375C)	Kube et al., 2014
VipA/VipB(Q429C)	Kube et al., 2014
VipA/VipB(E375C/Q429C)	Kube et al., 2014

2.2 Methods

2.2.1 Cell culture methods

Proteins are expressed in *E. coli*. Cultivation methods are described below. All media are autoclaved before use and supplemented with antibiotics dependent on the selection markers (see table 2.6) unless stated otherwise. Antibiotics are dissolved in ddH_2O, sterile filtrated and stored at -20 °C.

Table 2.6: Antibiotic supplement according to plasmid used.

plasmid	antibiotic	final concentration
pQE31	Ampicillin	100 µg/mL
pLacIQ	Spectinomycin	50 µg/mL

2.2.1.1 Cultivation of *E. coli* strains

For plasmid isolation, 2 mL of 2YT medium (see table 2.7) are inoculated with a single bacterial colony picked from a LB agar plate (see table 2.8). The culture is incubated at 37 °C and 120 rpm overnight on a shaker.

For protein purification, 25 mL of 2YT medium per 1 L of expression culture is inoculated with the *E. coli* protein expression strain. The starter culture is incubated at 37 °C and 120 rpm overnight. The expression culture is inoculated with starter culture and incubated at 37 °C and 120 rpm until an OD_{600} between 0.6 to 0.8 is reached. Then, protein expression is induced by adding IPTG to a final concentration of 1 mM. The cells are harvested after 3 h incubation at 37 °C and 120 rpm by centrifugation for 10 min at 4,000 rpm (3.501 x g) and 4 °C on a Sorvall RC Evolution centrifuge (Thermo Fisher Scientific, Inc., Waltham (MA), USA) using the SCL-6000 rotor. The cell pellet is resuspended in 20 mL to 40 mL of supernatant and centrifuged at 4,000 rpm (5,063 x g) for 20 min and 4 °C. The supernatant is discarded and cell pellets are stored at -80 °C until further use.

Table 2.7: 2YT medium.

16 g	Bacto trypton
10 g	yeast extract
5 g	NaCl
ad 1L	dH_2O
adjust to pH 7.5	

Table 2.8: LB medium for agar plates.

10 g	Bacto trypton
5 g	yeast extract
6 g	NaCl
15 g	agar
ad 1L	dH_2O

2.2.1.2 Cryo conservation of *E. coli* strains

1 mL of *E. coli* overnight culture is mixed thoroughly with 400 µL of autoclaved 80% glycerol. Cells are stored at -80 °C.

2.2.2 Molecular biology methods

DNA is treated according to the methods described below.

2.2.2.1 Plasmid isolation

Plasmids are isolated from overnight cultures of DH5α cells using the QIAGEN Spin Miniprep kit (QIAGEN, Venlo, Netherlands) according to instructions provided by the manufacturer.

2.2.2.2 Site-directed mutagenesis

Mutations are introduced into DNA sequences by site-directed mutagenesis in a PCR reaction with mismatch primers. A 50 µL reaction is composed as follows:

0.2 - 3.0 µL	30 -80 ng/µL DNA template
5 µL	10x Pfu buffer supplemented with 20 mM $MgSO_4$ (Thermo Fisher Scientific, Inc., Waltham (MA), USA)
0.5 µL	forward primer 25 pmol/µL
0.5 µL	reverse primer 25 pmol/µL
1 µL	10 mM dNTP mix (Thermo Fisher Scientific, Inc., Waltham (MA), USA)
1 µL	2.5 U/µL Pfu DNA Polymerase (Thermo Fisher Scientific, Inc., Waltham (MA), USA)
ad 50 µL	ddH_2O (autoclaved)

PCR reactions are incubated on a Biometra T1 Thermocycler (Analytik Jena AG, Jena, Germany) using the following program:

lid temperature:	110 °C		preheating on
1x	95 °C	30 s	
18x	95 °C	30 s	
	55 °C	1 min	adapt annealing temperature to primer (see table 2.3)
	68 °C	11 min 20 s	
1x	68 °C	1min	
store at 4 °C			

The PCR product is checked by electrophoresis on a 0.8 % agarose gel (see 2.2.2.6) and 30 µL of the PCR reaction are digested with FastDigest DpnI (Thermo Fisher Scientific Inc.,

Waltham (MA), USA) overnight at 37 °C. After digestion, *E. coli* DH5α cells are transformed using 10 µL of the digestion reaction (see 2.2.2.3) and as a control 10 µL of the PCR reaction, respectively. Then, the plasmid is isolated from single clones (see 2.2.2.1) and positive clones are identified by Sanger sequencing (GATC Biotech AG, Constance, Germany). In the case of the mutant P390I, in which also an additional PvuII restriction site is introduced, positive clones are also investigated by restriction digestion (see 2.2.2.4) using the enzymes PvuII-HF (NEB Inc., Ipswich (MA), USA) and HindIII (NEB Inc., Ipswich (MA), USA).

2.2.2.3 Transformation of chemo-competent *E. coli* strains

Chemo-competent *E. coli* cells are transformed following an adapted protocol by Hanahan [1983]. 50 µL of DH5α cells are incubated with 5 - 10 µL of plasmid DNA for 15 min on ice. Afterwards, the cells are heat-shocked at 42 °C for 2 min and cooled down for 2 min on ice. 500 µL of pure 2YT medium are added to the cells. After an incubation period of 1 h at 37 °C and 120 rpm, the cells are pelleted by centrifugation for 1 min at 13,000 rpm (15,871 x g). The pellet is resuspended in 50 µL of the supernatant and plated on LB agar plates supplemented with ampicillin. The plates are incubated overnight at 37 °C. For transforming BL21-DE3 cells, the protocol is modified. 100 µL of competent cells are incubated with 5 µL of plasmid DNA for 30 min on ice, 900 µL of 2YT are added after the cool-down, and the cells are subsequently incubated for 30 min at 37 °C.

2.2.2.4 Restriction digestion

A 20 µL restriction preparation is composed as follows:

3 µL	30 -80 ng/µL DNA
2 µL	10x buffer as indicated by the manufacturer
1 U	of each restriction enzyme
ad 20 µL	ddH_2O (autoclaved)

The sample is incubated for at least 2 h at 37 °C.

2.2.2.5 DNA concentration determination

DNA concentration and purity is determined by measuring absorption at 260 nm and 280 nm using a NanoDrop 1000 Spectrometer (Thermo Fisher Scientific Inc., Waltham (MA), USA).

2.2.2.6 Agarose gel electrophoresis

DNA samples are electrophoretically separated on a 0.8 % agarose gel stained with DNA Stain G (Serva Electrophoresis GmbH, Heidelberg, Germany) in 1x TBE running buffer (see table 2.9). DNA samples are mixed with 5x DNA loading buffer (see table 2.10) before the run. Electrophoresis is run at 120 V for 45 min on a PerfectBlue gel system Mini M (Peqlab Biotechnologie GmbH, Erlangen, Germany). Gels are documented on a SafeLab Imager (Intas Science Imaging Instruments GmbH, Göttingen, Germany). Gene Ruler DNA ladder (Thermo Fisher Scientific Inc., Waltham (MA), USA) is used as a size marker for DNA fragments.

Table 2.9: 10x TBE buffer.

900 mM	Tris-HCl pH 8.0
900 mM	boric acid
10 mM	EDTA

Table 2.10: 5x DNA loading buffer.

10 % (v/v)	glycerol
50 % (v/v)	10x TBE buffer
a pinch of	bromophenol blue

2.2.3 Protein biochemistry methods

Proteins are purified and analyzed using the methods described below.

2.2.3.1 SDS polyacrylamid gel electrophoresis

Table 2.11: Stacking and separating gels composition. Volumes are sufficient for two gels.

	stacking gel	12 % separating gel	15 % separating gel
ddH_2O	3.05 mL	3.5 mL	2.35 mL
0.5 M Tris pH 6.8	1.25 mL	-	
1.5 M Tris pH 8.8	-	2.5 mL	
10 % (w/v) SDS	50 µL	100 µL	
acrylamid	650 µL	4 mL	5 mL
10 % (w/v) APS	50 µL	50 µL	
TEMED	5 µL	5 µL	

SDS polyacrylamid gel electrophoresis (SDS-PAGE) is performed following a modified protocol by Laemmli [1970]. Stacking and separating gels are composed as presented in table 2.11 and polymerized for 30 min before usage. Protein samples are mixed with 4x Laemmli loading buffer (see table 2.12) incubated at 95 °C for 5 min before electrophoretic separation at 200 V for 1 h in 1x Laemmli running buffer (see table 2.13) on a Mini-Protean Tetra Cell system (Bio-Rad Laboratories, Inc. Hercules (CA), USA). NEB Prestained Protein Marker Broad Range (NEB, Inc., Ipswich (MA), USA) and Roti-Mark Standard (Carl Roth GmbH & Co. KG, Karlsruhe,

Germany) are used as a size marker for proteins. In case of a non-reducing SDS-PAGE, DTT is omitted from the 4x Laemmli loading buffer.

Table 2.12: 4x Laemmli loading buffer.

200 mM	Tris-HCl pH 6.8
50 % (v/v)	glycerol
4 % (w/v)	SDS
10 mM	DTT
a pinch of	bromophenol blue

Table 2.13: Laemmli running buffer.

25 mM	Tris-HCl
200 mM	glycin
0.1 % (w/v)	SDS

2.2.3.2 Protein precipitation with trichloroacetic acid and SDS

For SDS-PAGE followed by Western blotting, protein samples are precipitated with trichloroacetic acid (TCA) and SDS. Each Protein sample is mixed gently with each 100 µL of 72 % (w/v) TCA and 0.15 % (w/v) of SDS, respectively. Subsequently, it is incubated for 15 min at room temperature and then centrifuged for 10 min at 13,200 rpm (16,363 x g) and 4 °C. The pellet is washed with 500 µL of chilled acetone and centrifuged for 5 min at 13,200 rpm (16,363 x g) and 4 °C. Afterwards, the supernatant is discarded and the pellet is dried at room temperature, before it is resuspended in 20 - 50 µL volume of 1x Laemmli loading buffer.

2.2.3.3 Coomassie Brilliant Blue stain

Polyacrylamid gels that are not used for Western blotting are stained with Coomassie Brilliant blue. The gel is shortly boiled in 20 mL Coomassie staining solution (see table 2.14) and subsequently incubated for 20 min at room temperature on a shaker. Afterwards, the gel is destained in destaining solution (see table 2.15) at room temperature on a shaker until bands are clearly visible.

Table 2.14: Coomassie staining solution.

45 % (v/v)	methanol
10 % (v/v)	acetic acid
0.25 % (w/v)	Coomassie Brilliant Blue R-250
filter before use	

Table 2.15: Destaining solution.

45 % (v/v)	methanol
10 % (v/v)	acetic acid

2.2.3.4 Silver stain

For the chemical cross-link titration experiments, polyacrylamid gels are stained with colloidal silver. The gel is incubated in 50 % (v/v) ethanol for 20 min, followed by another 20 min in

5 % (v/v) ethanol. Then, it is soaked in 35 µM DTT solution for 5 min and in 40 mL of freshly prepared silver nitrate solution (see table 2.16) for 10 min. Afterwards the gel is rinsed twice with ddH_2O and twice with 25 mL of chilled developing solution (see table 2.17). Gel bands are developed to the desired darkness by incubating the gel in 50 mL of chilled developing solution. The reaction is stopped by adding citric acid powder until the solution is saturated. The gel is soaked in this solution for 10 min.

Table 2.16: Silver nitrate solution.

0.1 % (w/v)	silver nitrate
0.0037 (v/v)	formaldehyde

Table 2.17: Developing solution.

283 mM	Na_3CO_3
0.0185 % (v/v)	formaldehyde

2.2.3.5 Amido black stain

Protein on nitrocellulose membranes is unspecifically stained with Amido black 10B. The blot membrane is soaked with 45 mL of ddH_2O supplemented with 5 mL of amido black staining solution (see table 2.18) for 5 min at room temperature. The membrane is subsequently rinsed with ddH_2O to remove excess stain.

Table 2.18: Amido black staining solution.

0.1 % (w/v)	Amido black 10B
40 % (v/v)	methanol
10 % (v/v)	acetic acid

2.2.3.6 Western blot

Protein from unstained SDS-PAGE gels are electrophoretically transferred onto nitrocellulose membranes by semi-dry Western blotting (modified after Burnette, 1981). For a description of the antibodies used in the experiments please see table 2.4. The nitrocellulose membrane (Whatman Protran BA 85, GE Healthcare, Little Chalfont, UK) and four filter papers (MN 218 B, Macherey-Nagel GmbH & Co. KG, Düren, Germany), all cut to the size of the separating gel, are soaked in blotting buffer (see table 2.19). Two filter papers are placed on top of each other onto the anode plate of a PerfectBlue semi-dry electroblotter (Peqlab Biotechnologie GmbH, Erlangen, Germany), above which the nitrocellulose membrane followed by the gel, two layers of filter paper and the cathode plate are placed. Proteins are transferred onto the membrane for 90 min in a electric current of 400 mA. Afterwards, the membrane is stained with amido black (see 2.2.3.5) and an image of the stained membrane is taken. Unspecific binding of protein is blocked by incubating the membrane for 30 min at room temperature in 5 % (w/v) milk powder solution. Then, primary αHis antibody is added to the milk powder solution (final dilution 1:1,000) and the membrane is incubated overnight at 4 °C. This step is omitted when αHA

antibody is detected in gradient profiles directly with secondary α-mouse antibody conjugated to HRP. The membrane is washed three times with 20 mL of TST buffer (see table 2.20) and then incubated with secondary antibody diluted 1:10,000 in 5 % (w/v) milk powder solution for 2 h at room temperature followed by another three washing steps with 20 mL of TST buffer. Finally, the membrane is rinsed with ddH_2O. HRP chemiluminescence activity is detected on hyperfilm (Amersham Hyperfilm ECL, GE Healthcare, Little Chalfont, UK) after incubating the membrane for 1 min in a mixture of 10 mL of ECL solutions A and B (see tables 2.21 and 2.22), respectively.

Table 2.19: Blotting buffer.

12.5 mM	Tris
100 mM	glycine
20 % (v/v)	methanol *p.a.*
0.05 % (w/v)	SDS

Table 2.20: TST buffer.

50 mM	Tris-HCl pH 7.4
150 mM	NaCl
0.1 % (v/v)	Tween 20

Table 2.21: ECL solution A.

100 mM	Tris-HCl pH 8.5
0.4 mM	coumaric acid
2.5 mM	luminol

Table 2.22: ECL solution B.

100 mM	Tris-HCl pH 8.5
0.007 % (w/v)	H_2O_2

2.2.3.7 Cell lysis by microfluidization

For the lysis, the *E. coli* cell pellet is resuspended in 10 mL of freshly prepared lysis buffer (see table 2.23) per 5 g of cell mass. The lysis buffer is supplemented with cOmplete EDTA-free protease inhibitor tablets according to the instructions of the manufacturer (Roche Diagnostics Deutschland GmbH, Mannheim, Germany). The cells are mechanically disrupted in 3 to 4 cycles in a microfluidizer (Microfluidics, Westwood (MA), USA) operated at 103 MPa.

Table 2.23: Lysis buffer

50 mM	NaH_2PO_4 pH 8.0
300 mM	NaCl
5 mM	β-mercapto-ethanol

2.2.3.8 Immobilized metal ion chromatography (IMAC)

VipA/B tubules are co-purified with the poly-histidine tagged N-terminal domain of ClpV as established by Bönemann et al. [2009]. The cell lysate is centrifuged for 25 min at 18,000 rpm (38,724 x g) and 4 °C on a Sorvall RC Evolution centrifuge (Thermo Fisher Scientific Inc.,

Waltham (MA), USA) using the SS-34 rotor, while 1.5 mL of Ni-NTA agarose bead slurry (QIAGEN, Venlo, Netherlands) per 5 g of initially used cell pellet are equilibrated with lysis buffer (see table 2.23). After the centrifugation, the supernatant is incubated with the equilibrated Ni-NTA agarose for 1 h at 4 °C on a spinning wheel. The suspension is transferred to an Econo-Pac chromatography column (Bio-Rad Laboratories, Inc. Hercules (CA), USA) and washed twice with 10 mL of lysis buffer. Proteins are eluted from the column using five bed volumes of lysis buffer supplemented with 250 mM imidazole. After the elution, the Ni-NTA agarose is washed with 20 mL of 1 M imidazole, of ddH_2O and of 20 % (v/v) ethanol, respectively. The packed column is stored at 4 °C.

2.2.3.9 Size exclusion chromatography

The ClpV N-terminal domain is separated from the VipA/B tubules by size exclusion chromatography (SEC) on an equilibrated HiLoad 16/600 Superdex^{TM} 200 column (S-200, GE Healthcare, Little Chalfont, UK) in SEC buffer (see table 2.24). The combined IMAC elution fractions are centrifuged for 10 min at 13,000 rpm (15,871 x g) and 4 °C before being loaded onto the column. SEC is run on an Äkta P-900 system (GE Healthcare, Little Chalfont, UK) at a flow rate of 0.5 mL/min and a maximum pressure of 0.3 MPa in an 8 °C environment. UV absorption at 250 nm and 280 nm is recorded. Void fractions are collected and analyzed by SDS-PAGE. For vitrification, fractions are concentrated on Millipore Amicon Ultra centrifugal filters with a molecular weight cut-off of 100 kDa (Merck KGaA, Darmstadt, Germany). After use, the Äkta system and the column is washed with 2 column volumes of ddH_2O and 2 column volumes of 20 % (v/v) ethanol. The column is stored in 20 % ethanol. All buffers and solutions are sterile-filtered and degassed before use.

Table 2.24: SEC buffer.

50 mM	Tris pH 7.5
150 mM	KCl
20 mM	$MgCl_2$
2 mM	DTT

2.2.3.10 Analytical ultracentrifugation

Alternatively, VipA/B tubules are purified from IMAC fractions by analytical ultracentrifugation on a 10 - 40 % (v/v) glycerol gradient (see table 2.25). The gradients are prepared in 13 x 51 mm Seton open top Polyclear^{TM}tubes (Science Services GmbH,

Table 2.25: Gradient for VipA/B purification.

50 mM	HEPES pH 7.5
150 mM	KCl
10 % (v/v) or 40 % (v/v)	glycerol

Munich, Germany) and 400 µL of combined IMAC elution fractions are applied. The samples are ultracentrifuged for 16 h at 33,000 rpm (132,335 x g) and 4 °C in a Beckman L80 Ultracentrifuge (Beckman Coulter, Inc., Pasadena (CA), USA) using a SW 55 Ti rotor. Afterwards, the pellet fraction is resuspended in gradient buffer without glycerol.

2.2.3.11 Protein concentration determination

Protein concentrations are determined using a bicinchomic acid assay (BCA, Thermo Fisher Scientific Inc., Waltham (MA), USA)) according to the instructions provided by the manufacturer. Protein concentration references are prepared using bovine serum albumin (Sigma Aldrich, St. Louis (MO), USA) and absorbance at 562 nm is recorded using a Infinite M1000 microplate reader (Tecan Group Ltd., Maennedorf, Switzerland).

2.2.3.12 Protein cross-linking using Di-sulfo-succinimidyl-glutarate

Before cross linking wild-type VipA/B tubules, VipA/VipB$\Delta C^{210}$and VipA/VipBΔC^{367}in batch for mass-spectrometric analysis, cross-linking conditions are optimized in cross-linker titration experiments. For this, 3 µg of protein are thoroughly pipette-mixed with isotope-labelled H6/D6 Di-sulfo-succinimidyl-glutarate (DSSG, Creative Molecules, Inc., Victoria, Canada) dissolved in ddH_2O. The final cross-linker concentration is varied. Samples are incubated for 30 min at 30 °C. Cross-linking reactions are quenched by pipette-mixing with ammonium bicarbonate solution to a final concentration of 100 mM and incubating them for another 30 min at 30 °C. For mass-spectrometric analysis, 180 µg/mL of wild-type tubules are cross-linked in batch with 0.1 mM and 0.4 mM of DSSG. The truncation mutants (180 µg/mL) are cross-linked with 0.4 mM DSSG. To further increase the protein concentration of the truncation mutant for the analysis, truncation mutant samples are concentrated twice on Millipore Amicon Ultra centrifugal filters (Merck KGaA, Darmstadt, Germany) with a 10 kDa molecular weight cut-off.

2.2.3.13 Analysis of protein cross-links by mass-spectrometry

Cross-link mass spectrometry (XL-MS) is performed by T. Zimniak and F. Herzog as described in Herzog et al., 2012. Cross-linked peptides are analyzed from a tryptic digest of the samples by LC-MS/MS.

2.2.3.14 Protein cross-linking using glutardialdehyde

Proteins are cross-linked with glutaraldehyde following the GraFix method [Kastner et al., 2008]. A glycerol gradient is prepared as described (see 2.2.3.10) but additionally glutaraldehyde (Carl Roth GmbH & Co. KG, Karlsruhe, Germany) is added to the heavier gradient buffer

to a final concentration of 0.025 %. Thus, a glutaraldehyde gradient from 0.0 % to 0.025 % is created. A reference gradient without cross-linker is included into each run to control the migration of the protein in the gradient. The ultracentrifugation is performed as described above. The cross-linked sample in the pellet fraction is resuspended in gradient buffer without glycerol and quenched with Tris-HCl pH 8.0 to a final concentration of 100 mM.

2.2.3.15 Cystein cross-linking of proteins

Cysteine cross-linking experiments are performed by N. Kapitein and A. Mogk at the DKFZ Heidelberg as described in Kube et al., 2014. Cross-linked cystein mutants ClpV-N(A86C) and VipA/VipB(T27C) are co-purified without DTT. Mutant complexes VipA/VipB(E375C), VipA/VipB(Q429C) and VipA/VipB(E375C/Q429C) (each 1 - 5 µM) are reduced with 50 µM Tris(2-Carboxyethyl)Phosphine) (TCEP) for 30 min at 30 °C. The reducing agent is removed in PD-10 desalting columns (GE Healthcare, Little Chalfont, UK). Cysteins are cross-linked by adding copper phenanthroline to a final concentration of 25 - 500 µM and incubating the sample for 30 min at 20 °C . The reaction is quenched by adding Laemmli loading buffer supplemented with 5 mM EDTA and 20 mM iodoacetamide. Cross-linked samples are analyzed on a non-reducing polyacrylamid gradient gel.

2.2.3.16 Analytical protein digestion

Analytical digestion of wild-type VipA/B tubules are performed by N. Kapitein and A. Mogk as described in Kube et al., 2014. 30 µg of VipA/B are digested in SEC buffer with 8 µg in a 100 µL reaction volume for 90 min at room temperature. Protein fragments from SDS-PAGE gels are identified by mass spectrometry and Edman sequencing of protein N-termini (Toplab, Munich, Germany).

2.2.4 Electron microscopy methods

Various high and low resolution electron microscopic methods are used to investigate the structure of the VipA/B complex.

2.2.4.1 Glow discharging of EM grids

Carbon coated electron microscopy grids are glow-discharged prior to use in a plasma cleaner (Harrick Plasma, Ithaca (NY), USA) at a pressure below 29.3 Pa. Grids used for negative stain are glow-discharged for 45 s, while grids used for cryo EM are glow-discharged for 30 s.

2.2.4.2 Negative stain

Samples are stained either with 2 % uranyl acetate (Ted Pella, Inc., Redding (CA), USA) or Nano-W (Nanoprobes, Inc., Yaphank (NY), USA). 3.5 µL of protein sample diluted to a concentration of 20 - 50 µg/mL are incubated for 45 s at room temperature on a grid coated with continuous carbon film (Quantifoil Micro Tools GmbH, Jena, Germany or Plano GmbH, Wetzlar, Germany). Excess sample is carefully blotted off using the tip of a circle sector shaped piece of Whatman #1 filter paper (GE Healthcare, Little Chalfont, UK). 3.5 µL of stain are applied and blotted off immediately afterwards followed by another 3.5 µL of stain which are incubated for 15 s on the grid before being blotted off. In the case of Nano-W, a residual volume of stain is left on the grid which is then air-dried to create a deeper stain.

2.2.4.3 Sample vitrification for cryo EM

Approximately 0.3 mg/mL of protein solution are vitrified in liquid ethane on glow-discharged Quantifoil R 3/3 holey carbon grids with 2 nm carbon support film (Quantifoil Micro Tools GmbH, Jena) using a Vitrobot Mark VI (FEI, Hillsboro (OR), USA). Grids are cleaned prior to use by incubating them for at least 15 min in chloroform. The sample is incubated on the grid for 45 s at 4 °C and 100 % humidity, and then blotted away with a blot force of 0 for 3.5 s using two layers of Munktell grade 4b filter paper (Munktell & Filtrak GmbH, Bärenstein, Germany).

2.2.4.4 Labeling of poly-histidine tags by Ni-NTA Nanogold

Wild-type and poly-histidine tagged protein complexes are incubated with Ni-NTA Nanogold (Nanoprobes, Inc, Yaphank (NY), USA) at a final dilution of 1:50 for 5 min at room temperature. Afterwards, the sample is stained with uranyl acetate as described in 2.2.4.2.

2.2.4.5 Antibody labeling of HA-tags

3.3 µM of wild-type and HA-tagged protein complexes are incubated overnight with 0.09 µM of αHA antibody in a volume of 100 µL at 4 °C. Free antibody is subsequently removed by ultracentrifugation in a 10 - 40 % glycerol gradient (see table 2.26) as described . Resuspended pellet fractions are stained with Nano-W.

Table 2.26: Gradient for antibody removal.

50 mM	HEPES pH 8.0
150 mM	KCl
10 mM	$MgCl_2$
10 or 40 %	glycerol

2.2.4.6 Binding of ClpV to VipA/B

0.9 µM of ClpV are incubated for 5 min at 37 °C with 2.5 µM of VipA/B in the presence of 2.5 mM ATPγS. The sample is stained with uranyl acetate.

2.2.4.7 Collection of negative stain data

Single micrographs are collected on a FEI Morgagni transmission electron microscope (FEI, Hillsboro (OR), USA) at 80 keV with a SIS Megaview 1K CCD camera. The nominal magnification is 60,000x. Images of antibody labelled tubules and micrographs used for further computational analysis are collected on Tecnai G2 Spirit transmission electron microscope (FEI, Hillsboro (OR), USA) at 120 keV under low-dose conditions with an Eagle 2,048 x 2,048 pixel CCD camera (FEI, Hillsboro (OR), USA). The nominal magnification is 96,774 which results in pixel size of 3.1 Å at the specimen level. The under-focus is varied between 200 - 1,500 nm. Micrographs of ClpV bound to VipA/B are taken semi-automatically in spot scan series of 4 micrographs per hole using EM-TOOLS software (TVIPS GmbH, Gauting, Germany).

2.2.4.8 Collection of cryo EM data

A total of 12,271 micrographs of vitrified VipA/B are collected on a Titan Krios TEM (FEI, Hillsboro (OR), USA) with a 4,096 x 4,096 pixel (scan pixel size 15.6 µm) TemCam-F416 CMOS camera (TVIPS GmbH, Gauting, Germany). Images are semi-automatically collected using the EM-Tools software (TVIPS GmbH, Gauting, Germany) taken under low-dose conditions at 200 keV in spot scan series of 7 micrographs per hole and the under-focus is varied between 1,000 - 4,500 µm. The pixel size is calibrated to 1.0698 Å using the layer line pattern of tomato mosaic virus.

2.2.5 Electron microscopy data processing

EM images are further analyzed employing 2D and 3D methods to reconstruct the VipA/B tubule and to interpret the EM map.

2.2.5.1 Preprocessing of electron micrographs

Contrast transfer functions (CTF) are determined on two times decimated micrographs using CTFFIND3 [Mindell and Grigorieff, 2003]. Micrographs with more than 16 % astigmatism, too much contamination or more than 5,000 nm defocus are sorted out automatically or by visual inspection. Finally, the phases in each image are corrected for the effects of the CTF in SPIDER [Frank et al., 1996]. Individual images of single particles are selected manually

in BOXER [Ludtke et al., 1999] with an overlap of 60 % when more than one box could be placed on a tubule, or semi-automatically in FINDEM [Roseman, 2004] when class averages from multi-variate statistical analysis are available as a template. For this, micrographs are two times decimated, filtered between 15 Å and 150 Å and a cross-correlation peak width of 12 Å was used. The minimal stay away between particle centers was set to 12 Å.

2.2.5.2 Multi-variate statistical analysis and 2D multi reference alignment

Generally, multi-variate statistical analysis and 2D multi reference alignment is done in IMAGIC-5 [van Heel et al., 1996]. First, images are high-pass filtered to 300 Å, masked, and normalized. Single particles representing side views of the VipA/B tubule are centered by aligning them to a centered single image while top views are iteratively centered to their rotational sum. Rounds of multi-variate statistical analysis and 2D multi reference alignment to selected homogenous class averages are repeated until alignments are not improving anymore.

2.2.5.3 Determination of the helical symmetry of the VipA/B tubule

Seven long intact tubular sections are extracted from cryo EM micrographs and padded into 4,096 x 4.096 boxes in SPIDER. They are Fourier-transformed and the Fourier-transforms are summed up. The sum was analyzed by Fourier-Bessel analysis in IMAGEJ [Diaz et al., 2010, Schneider et al., 2012] giving initial estimates of the helical symmetry parameters. The parameters are refined in an IHRSR++ 1.4 run [Egelman, 2007a, Parent et al., 2010] with 2,424 manually selected and two times decimated images as an input. The start parameters 21.7 Å unit rise, 30 ° unit twist and an additional C6 symmetry are refined to 22.2 Å and 29.55 ° after 30 iterations with an angular search increment of 0.1 ° and a translational increment of 0.1 Å. The refined parameters and the six-fold symmetry are used to obtain an initial 3D reconstruction of the tubule from class averages of a twice decimated dataset of 7,939 manually selected particles that are band-pass filtered between 2.2 Å and 320 Å using an adapted protocol of Clare and Orlova [2010].

2.2.5.4 Reconstruction of the VipA/B tubule

The initial 3D reconstruction (see 2.2.5.3) is used as a starting model for the iterative refinement of the orientations of 19,954 particles, that have been manually selected from 6,489 micrographs, by projection matching in SPIDER. Throughout the refinement, the angular sampling is stepwise reduced to 0.5 ° using C6 symmetry. After each alignment round, 70 - 80 % of all particles are selected based on their cross correlation coefficient and back-projected using interpolation in Fourier space (SPIDER command BP 3F). In the last refinement rounds the volume is filtered

between 15 Å and 5 Å before creating reference projections. Images are classified after multivariate statistical analysis when 90 % of the assigned angles are stable. Classes are selected based on their Fourier transform and their 2,328 members are used for the reconstruction resulting in a resolution of 8.8 Å after the $FSC_{0.5}$ criterion with a loose mask applied.

Additional particles are picked semi-automatically from the remaining micrographs and 108,016 particles are selected after multiple rounds of class-editing [Arbeláez et al., 2011]. The images are pretreated as described and added to the dataset. The merged dataset is refined by projection matching in SPIDER up to an angular sampling of 0.5 °. Undecimated data is used for the last refinement rounds and back-projection is performed in real space (SPIDER command BP RP). Before the last round, the dataset is classified using multivariate statistical analysis and the best classes were selected based on the amount of high resolution information in their Fourier transform. 16,394 particles are symmetrized as described [Clare and Orlova, 2010] and used for the final reconstruction at 5.8 Å resolution ($FSC_{0.5}$ criterion) which is filtered for display between 3 Å and 15 Å.

2.2.5.5 "Gold standard " refinement by regularized likelihood optimization

To check for potential over-refinement of the data, the final dataset of 16,394 particles is two times decimated and reprocessed according to the "gold-standard" in Relion [Henderson et al., 2012, Scheres and Chen, 2012, Scheres, 2012a,b]. The dataset is separated into two half-datasets which are refined independently from each other using regularized likelihood optimization with a reconstruction from IHRSR as a initial reference. In the first round, the refinement is limited to 30 Å and only a 6-fold rotational symmetry is employed. Helical parameters are searched in 3D by cross-correlation for both reconstructions independently and the reconstructions are symmetrized in 3D.

2.2.5.6 Resolution determination

Except for the "gold standard" reconstructions, the resolution is calculated by determining the cross-correlation between Fourier shells of volumes reconstructed from half-datasets that are separated after the last alignment round. The volumes are masked with hollow-cylinders with the height of one or more ring sections of the VipA/B tubule. Optionally they are additionally masked with a loose binary mask. An FSC of 0.5 is used as a resolution threshold.

"Gold standard" resolution is determined by calculating FSC between independent reconstructions. The FSC resolution threshold is 0.143.

2.2.5.7 Determination of handedness

The hand of the reconstruction is determined by overlaying the homologous C-terminal domain of the crystal structure 3J2N and the predicted model of the VipB C-terminal domain with the filtered EM map using the "Fit in Map" function in Chimera [Pettersen et al., 2004]. The overlay is evaluated visually and by cross-correlation between the structures and the map. Additionally the Fourier transform sum (see 2.2.5.3) is compared to published Fourier transforms of the T4 phage polysheath [Moody, 1967].

2.2.5.8 Map segmentation and atomic structure fitting

The EM map is segmented manually into protomers using Segger in Chimera [Pettersen et al., 2004, Pintilie et al., 2010] based on the location of protein termini, the overlay of VipA and VipB with the density and on the comparison to homologous viral tail sheath structures, 3J2N, 3LML and 3HXL.

3J2N is also used as a template to manually build the secondary structure model of the VipA/B protomer in Chimera. The C-terminal and middle segment of the structure is overlaid with the filtered EM map based on the best cross correlation. VipB secondary structure elements as predicted by PredictProtein [Rost et al., 2004] are built using standard rotamer libraries as provided by Chimera and placed into the EM density based on correspondences between them and the gp18 structure. Secondary structure elements of VipA are built accordingly and positioned into the remaining unfilled density guided by the characteristic helical density attributed to helix HA3.

2.2.5.9 Map visualization

All EM maps and structures are visualized in UCSF Chimera [Pettersen et al., 2004] except for figure 3.14 d which is created in PyMol (The PyMol Molecular Graphics System, MacPyMol, Schrödinger).

2.2.6 Protein structure prediction

VipB structural elements are predicted from their amino acid sequence using HHPred [Söding, 2005] and Quark [Xu and Zhang, 2012]. For HHPred, the C-terminal sequences of VipB (334 - 492 aa), 3J2N (511 - 646 aa), 3LML (307 - 454 aa) and 3HXL (301 - 439 aa) are used as an initial query resulting in a model of VipB C-terminal region (389 - 492 aa) created in Modeller [Eswar et al., 2007]. Quark is used to predict the N-terminal 4-helix bundle of VipB (1 - 85 aa).

3 Results

3.1 Purification of wild-type VipA/B tubules after over-expression in *E. coli*

Images for single particle reconstruction need to be acquired from a homogenous and ordered protein sample. Two purification protocols for VipA/B tubules are tested for their suitability.

3.1.1 Purification by immobilized metal ion affinity chromatography (IMAC) and size exclusion chromatography (SEC)

The purification protocol for VipA/B tubules expressed heterologously in *E. coli* has been established by A. Mogk and colleagues who also provided all *E. coli* strains [Bönemann et al., 2009]. It is based on the binding of the T6S-specific AAA+ ATPase ClpV to VipB via its N-terminal domain [Pietrosiuk et al., 2011]. The N-terminally poly-histidine tagged N-terminal domain (1-178 aa) of ClpV (ClpV-N) is co-purified from cell lysate together with VipA and VipB by IMAC (Fig. 3.1 a) on a Ni-NTA column. Afterwards, selected elution fractions (*) are further purified in a SEC step on a sephacryl S-200 column (GE Healthcare Life Sciences). Tubular complexes formed by VipA (18.5 kDa) and VipB (55.6 kDa) elute in the void volume (*1*), while ClpV-N (approx. 20 kDa) which constitutes the majority of the purified protein elutes in peak (*2*) (Fig. 3.1 b). The histidine-tag of the ClpV-N is detected in fractions of peak (2) but not in void fractions on a Western blot (Fig. 3.1 c). When stained with 2 % uranyl acetate, void fractions show fragmented short VipA/B tubules with a diameter of approximately 300 Å on electron micrographs (Fig. 3.1 d).

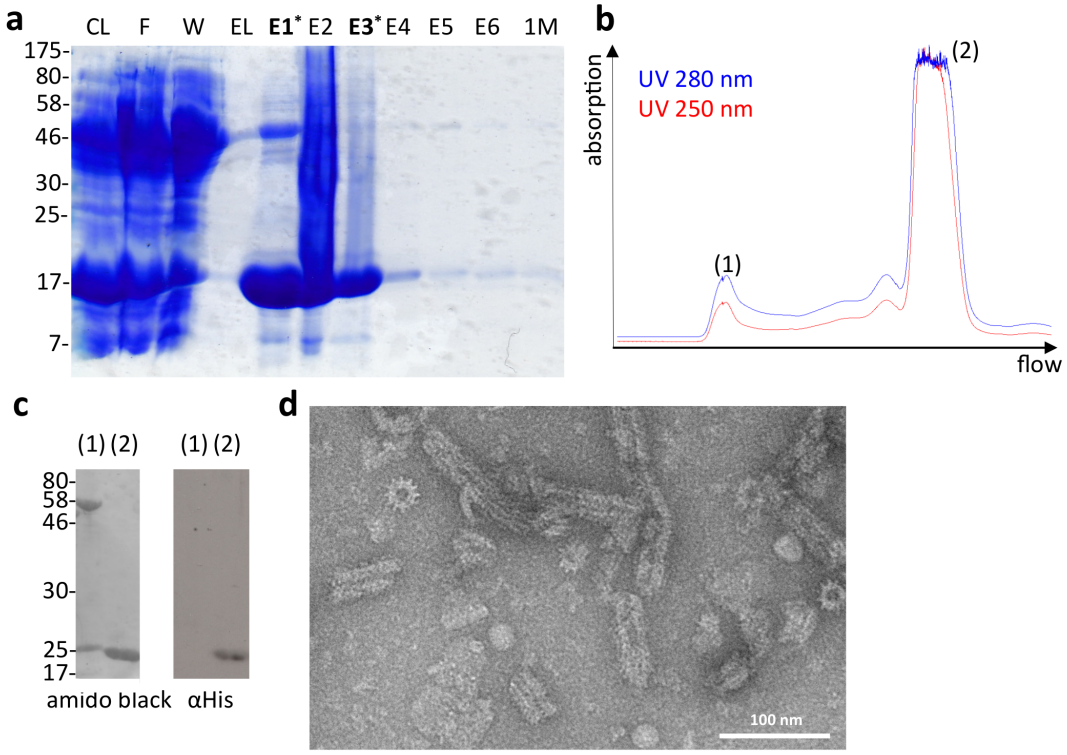

Fig. 3.1: Purification of wild-type VipA/B tubules by IMAC and SEC. (**a**) N-terminally poly-histidine tagged N-terminal domain of ClpV (ClpV-N) and VipA/B tubules are co-purified by IMAC on a Ni-NTA column; *CL*: cleared lysate, *F*: flow-through, *W*: wash fraction, *EL*: elution buffer (250 mM imidazole), *E1-E6*: elution fractions, *1M*: elution with 1M imidazole. Marked (*) elution fractions are treated by SEC on a S-200 column. (**b**) VipA/B tubules elute in the void fractions (*1*) while ClpV-N elutes in peak (*2*). (**c**) On a Western blot, the poly-histidine tag is not detected in the void fractions (*1*) but in fractions of peak (*2*). (**d**) A micrograph of a void fraction stained with 2 % uranyl acetate shows short VipA/B tubules.

3.1.2 Purification by IMAC and glycerol gradient ultracentrifugation

To separate fragmented VipA/B tubules, the SEC step was substituted by a ultracentrifugation step on a 10 - 40 % (v/v) glycerol gradient. Here, the histidine tag is detected on a Western blot of all precipitated fractions of the gradient (Fig. 3.2 a, b). Electron micrographs of the pellet fraction stained with 2 % uranyl acetate show longer and less fragmented tubules (Fig. 3.2 c).

To be able to employ the helical symmetry of the VipA/B tubule in the cryo EM reconstruction, either regular binding of ClpV-N to the tubule is needed, i . e. every binding site on the helical array is occupied, or ClpV-N needs to be completely separated from the tubules. Any irregular binding of ClpV-N disturbs the helical symmetry of the complex and artifacts are created during symmetrization. The ultracentrifugation protocol is time-efficient and more intact tubules

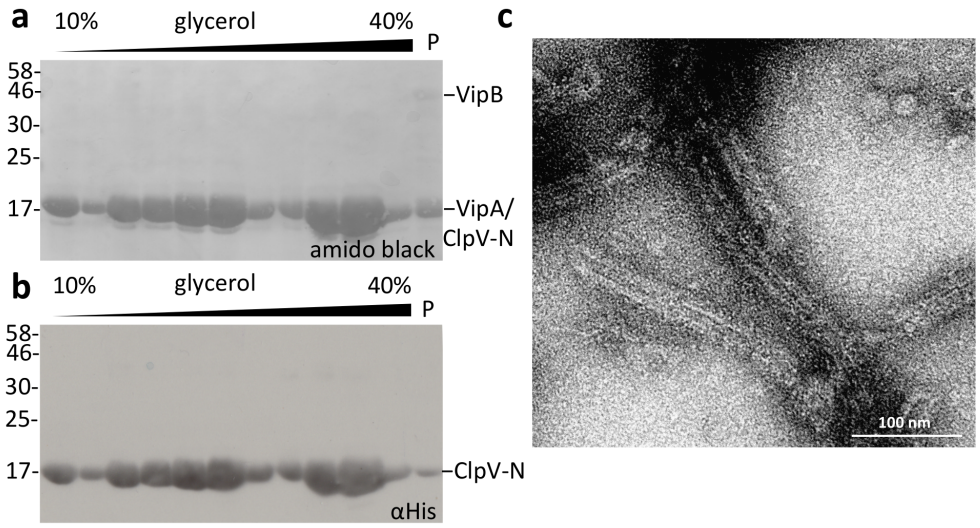

Fig. 3.2: Purification of wild-type VipA/B tubules by IMAC and glycerol gradient ultracentrifugation. (**a**, **b**) Co-purified N-terminally poly-histidine tagged ClpV-N and VipA/B tubules are treated by glycerol gradient ultracentrifugation. The poly-histidine tag is detected in all fractions and in the pellet (*P*) of a 10 - 40 % glycerol gradient. (**c**) A negative stain micrograph of the pellet fraction stained with 2 % uranyl acetate shows long intact VipA/B tubules. The experiment has been performed by J. Albrecht.

are obtained, but ClpV-N is still present in the sample and a regular binding of the domain on VipB cannot be guaranteed. Hence, VipA/B tubules purified by SEC are chosen for vitrification. In that sample, ClpV-N is not present and tubule fragments are still sufficiently long to allow a cryo EM reconstruction of the tubule by single particle methods.

3.2 Cryo EM reconstruction of the contracted VipA/B tubule

The VipA/B complex is purified as a helical tubule. Therefore, the exact symmetry of this complex has to be determined first before a volume is reconstructed from side view images.

3.2.1 Electron microscopy and symmetry determination of vitrified VipA/B tubules

Micrographs of VipA/B tubules vitrified on holey carbon film with an additional 2 nm carbon support film exhibit characteristic top (*T*) and side views (*S*, Fig. 3.3, left). The 12-meric cogwheel-like outline of the tubule top view class average (*T*, Fig. 3.3, right), which has been described for negatively stained single images previously [Bönemann et al., 2009], indicates a C12 or a C6 symmetry. The latter agrees with the tail sheath structures of contractile bacteriophages

(*Myoviridae*) which consist of six protofilaments. Contrarily to findings for the *P. aeruginosa* T6S system [Lossi et al., 2013], no 13-meric top views are observed. Side view class averages (*S*) present a periodic pattern of approx. 44 Å reminiscent of stacked rings.

Helical structures are defined by two symmetry parameters - a unit rise Δz defining the translation of the asymmetric unit along the helical axis and a unit twist $\Delta\varphi$ corresponding to its rotation around the axis. Projections of helical structures can be separated into two helical lattices defined by Δz and $\Delta\varphi$. The two lattices are mirror images, one is formed by the front side of the helical structure, the other one by the back side. In reciprocal space, the periodic lattices form a layer line pattern which is used to determine the helical parameters from projections of the structure. The more asymmetric units are included into a projection, the more layer lines become visible at higher frequencies as the signal-to-noise ratio increases.

Therefore, seven projections of long VipA/B tubules are Fourier-transformed and their transforms added up to further improve the signal (Fig. 3.4, *1*). Indexing the sum of transforms by Fourier-Bessel analysis gives initial estimates of the helical parameters (Fig. 3.4, *2*) [Diaz et al., 2010]. A strong meridional layer line l_3 indicates a unit rise of 22.1 Å while the Bessel orders $|n_1|$ = 11-12 and $|n_2|$ = 6-8 of layer lines l_1 and l_2 together with the 12-meric appearance of the VipA/B top views point towards a unit twist of approximately 30 °. The initial estimates are subsequently refined using the IHRSR method (Fig. 3.4, *3*) [Egelman, 2007b, Parent et al., 2010]. In this method, symmetry parameters are optimized iteratively in cycles of projection matching, followed by helical symmetry parameter determination by minimization of the mean square-deviation between symmetry-related density voxels and symmetrization of the reconstructed volume. After the parameter refinement, an initial model is reconstructed by assigning all symmetry-related positions defined by the optimized helical parameters of Δz = 22.2 Å and $\Delta\varphi$ = 29.44 ° and an additional C6 symmetry to copies of a single class average as described in Clare and Orlova, 2010 (Fig. 3.4, *4*).

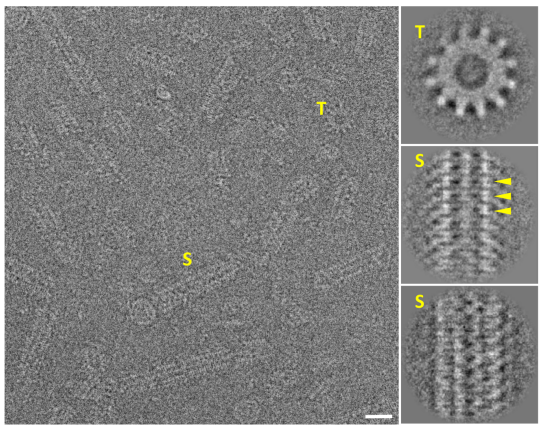

Fig. 3.3: Cryo electron microscopy of vitrified VipA/B tubules. *left:* Micrograph with inverted contrast of vitrified VipA/B tubules at approx. 2 µm under-focus. *right:* Class averages from multivariate statistical analysis of 12-meric top (*T*) and side views (*S*) presenting a periodic pattern of approx. 44 Å (*arrow heads*). *scale bar:* 300 Å.

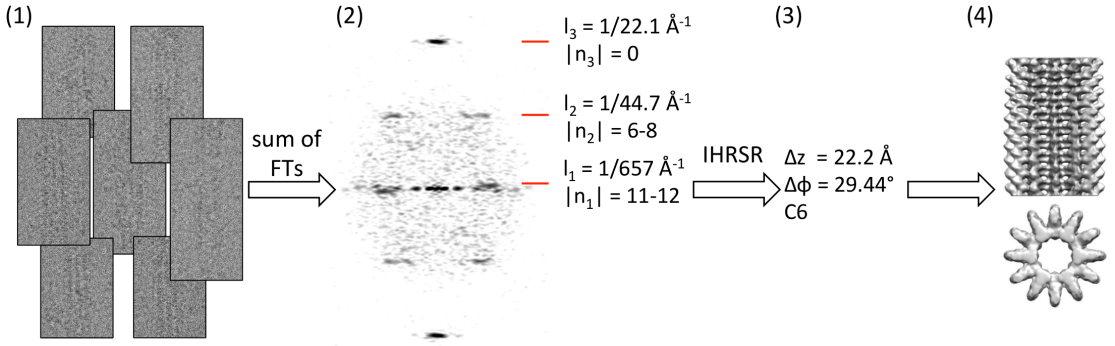

Fig. 3.4: Determination of the helical symmetry and initial model of VipA/B tubules. Seven long and intact helical sections (*1*) are cut out from cryo electron micrographs and their Fourier transforms (FT) summed up. Indexing the FT by Fourier-Bessel analysis [Diaz et al., 2010] (*2*) gives an initial estimate of the helical parameters unit rise (Δz) and unit twist ($\Delta\varphi$). (*3*) The estimates are refined using the IHRSR [Egelman, 2007b] method with an additional C6 symmetry. The parameters are applied to one class average from multivariate statistical analysis leading to the initial model (*4*) used for the refinement.

3.2.2 Cryo EM reconstruction

Starting from the model obtained as described in 3.2.1, the reconstruction is refined initially using 127,970 single images applying C6 symmetry. However, helical symmetry is used for the final reconstruction of the VipA/B tubule from the best 16,394 images (Fig. 3.5 a-d). Projections from the reconstructed volume are in good agreement with class averages from multi-variate statistical analysis of the dataset (Fig. 3.5 e).

Six right-handed protofilaments with a unit rise of 22.2 Å and a unit twist of 29.44 ° form the hollow VipA/B tubule with an inner diameter of 110 Å and an outer diameter of 290 Å. Alternatively, the VipA/B tubule can be described as a stack of hexameric rings with a height of 44.4 Å and six cogs protruding symmetrically from the rim of each ring. The rings are rotated by 29.44 ° against each other. Thus, each cog is placed in between the cogs of the neighboring rings giving the tubule a 12-meric outline when seen from the top. Since the unit twist is slightly smaller than 30 °, the surface ridges formed by the cogs on the outside of the tubule are left-handed with a pitch angle of 87 °. A previously published tomogram of the VipA/B tubule with right-handed surface ridges is contrasted by this finding [Basler et al., 2012],

Table 3.1: Helical parameters of the contracted VipA/B tubule and the T4 phage tail sheath [Aksyuk et al., 2011].

	Δz [Å]	$\Delta\varphi$ [°]	width [Å]
VipA/B contracted	22.2	29.4	290
T4 contracted	16.4	32.9	330
T4 extended	40.6	17.2	240

but earlier studies of polysheath-like structures in *Alcaligenes eutrophus* with a left-handed pitch angle of 86 ° are consistent with it [Walther-Mauruschat and Mayer, 1978].

The overall architecture of the VipA/B tubule is similar to that of the contracted T4 phage tail sheath which can be also seen from the comparison of the helical parameters as presented in table 3.1. Hence, it is assumed, that the reconstructed VipA/B tubule represents the contracted form. In fact, when T4 tail sheath protein gp18 is heterologously expressed without any other proteins of the phage, it assembles into long tubular structures called polysheaths that are very similar to the contracted form of the sheath [Kellenberger and De la Tour, 1964, Moody, 1967, Amos and Klug, 1975].

The resolution of reconstruction is determined by calculating the Fourier shell correlation (FSC) between reconstructions from half datasets separated after the last alignment round using a FSC of 0.5 as a cut-off. Depending on the masking and on the number of ring sections included into the analysis the resolution ranges between 5.4 - 6.3 Å (Fig. 3.6 a). As a control, the same dataset is two times decimated and reprocessed in RELION according to the "gold-standard" [Henderson et al., 2012, Scheres and Chen, 2012, Scheres, 2012a,b]. Following this procedure, a dataset is separated into two halves that are treated independently. FSC between the independent final models results in a resolution of 5.8 Å with a 0.143 cut-off (Fig. 3.6 b). The local signal resolution in the final map is additionally investigated in ResMap [Kucukelbir et al., 2014], showing a resolution range of approximately 4.4 - 6.4 Å in the ring body and of approximately 5 - 11 Å in the cogs of the cross section (Fig. 3.6 c). Finally, the sum of the Fourier transform of all images in the dataset exhibits layer lines at the expected locations in the spectrum up to a spatial resolution of 5.5 Å (Fig. 3.6 d). All in all, volume features until a resolution of 6 Å - i. e. secondary structure elements - can be reliably interpreted.

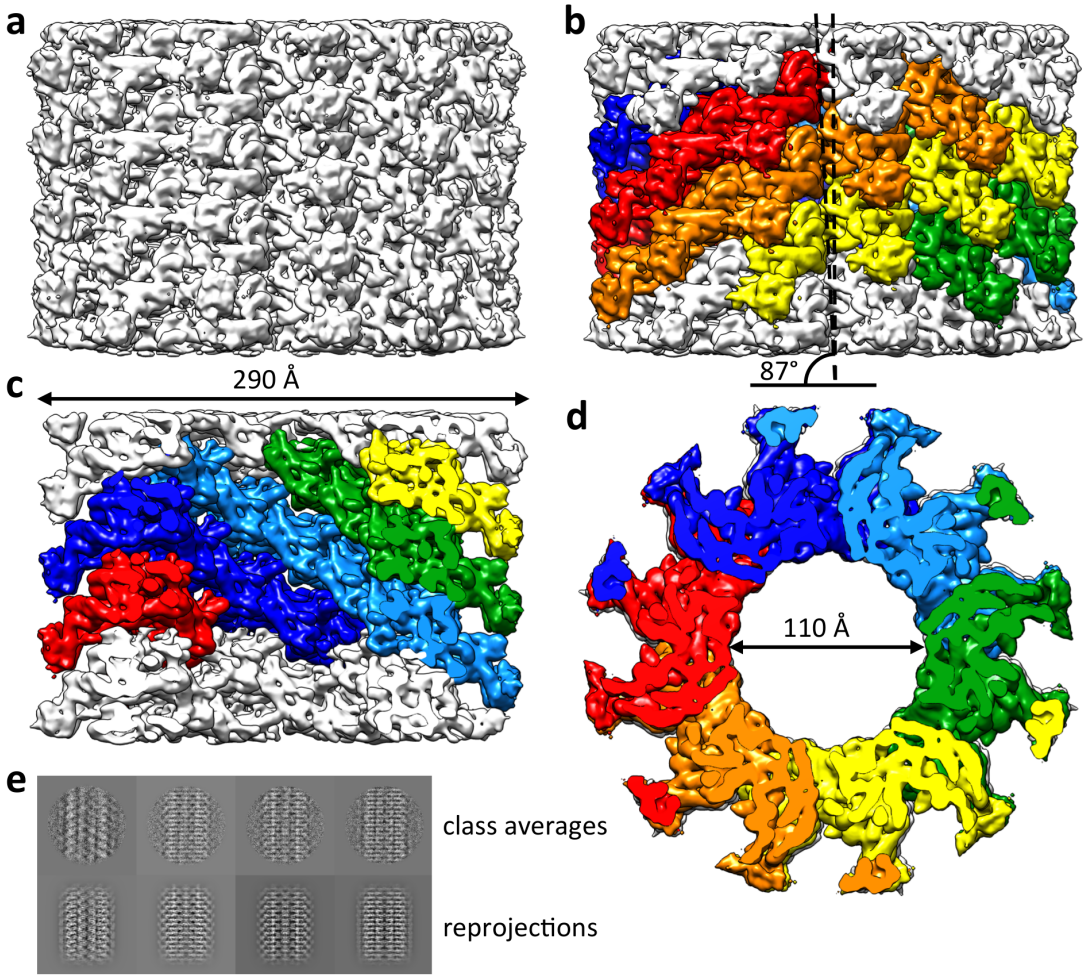

Fig. 3.5: Cryo EM reconstruction of the contracted VipA/B tubule. (**a**) The reconstructed map at a final resolution of 6.0 Å is filtered between 15 Å and 3 Å and segmented into six protofilaments (light blue, blue, red, orange, yellow and green) shown as a (**b**) side view, as a (**c**) cut-open, and as a (**d**) top view. (**e**) Class averages (approx. 30 members) from multivariate statistical analysis of the aligned dataset from the final reconstruction are juxtaposed to reprojections of the reconstruction into the Euler angle directions assigned to the class averages (adapted from Kube et al., 2014, please see also section 6.3 Reprints).

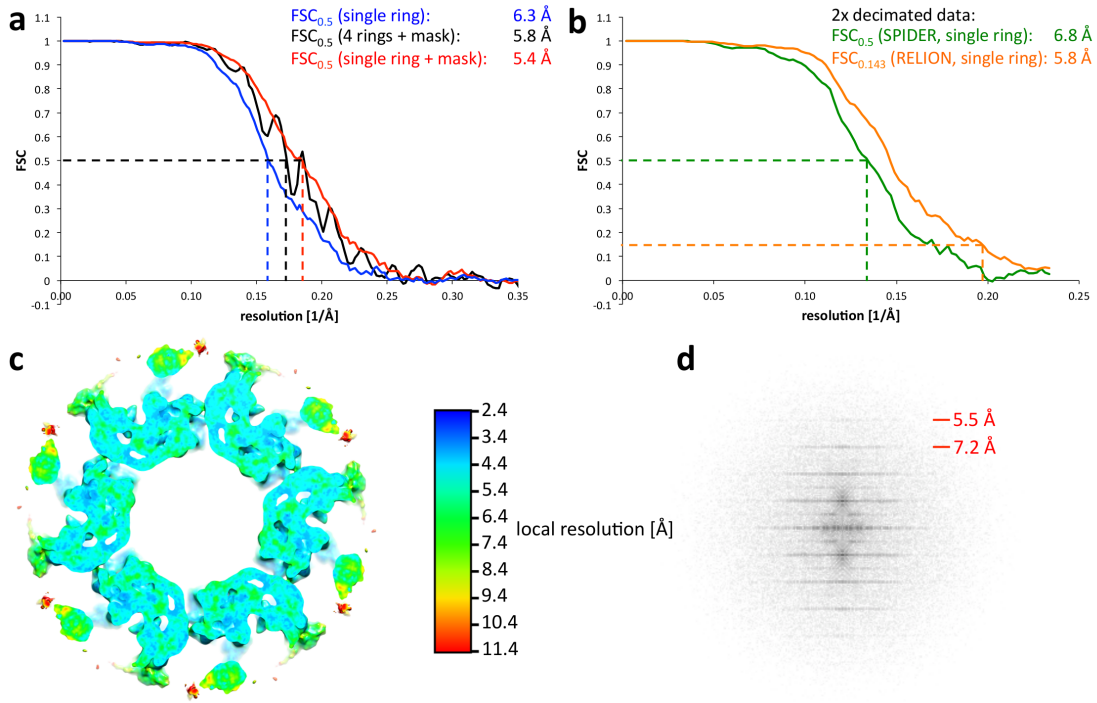

Fig. 3.6: Resolution of the reconstructed map. (**a**) The resolution of ~6 Å of the final reconstruction was determined by Fourier-shell correlation (FSC) between maps reconstructed from half-datasets separated after the last alignment and FSC determined between masked (black: 4 ring sections, red: one ring section) or unmasked ring sections (blue). (**b**) A "gold-standard" reconstruction in RELION using two times decimated data resulted in a final resolution of 5.8 Å (orange) compared to 6.8 Å after the described SPIDER protocol (green). (**c**) Local resolution determined in ResMap [Kucukelbir et al., 2014] of a ring section is represented in color code from 2.4 Å (blue) to 11.4 Å (red). (**d**) A sum of the Fourier transforms of all aligned particles selected for the final reconstruction shows layer lines visible up to 5.5 Å.

3.3 Modeling the structure of the protomer in the VipA/B tubule

There is little structural data on the VipA/B complex available that can be used to interpret the reconstruction. It is known that VipA and VipB are present in equimolar amounts in the tubule [Bönemann et al., 2009] and it has been shown in two-hybrid experiments that regions 100 - 122 aa in VipA and 63 - 163 aa in VipB are important for interaction between the proteins [Bröms et al., 2009, Aubert et al., 2010, Bröms et al., 2013]. However, no structure of homologues of the two proteins are available. Secondary structure elements can be safely identified in the EM map at 6 Å resolution, but it is not possible to segment the volume into individual protomers which is a prerequisite for Cα chain tracing of VipA and VipB in the protomer. Thus, additional information on the position of protein termini, on the domain topology, and on the individual structural motifs needs to be acquired in order to build a model of the protomer in a hybrid methods approach [Lander et al., 2012].

3.3.1 Localization of Protein Termini in the contracted tubule

Protein termini are localized in the tubule complex in two approaches. In a first experiment, which has been performed by N. Kapitein and A. Mogk (DKFZ Heidelberg), VipA/B tubules are analytically digested with trypsin. The time course experiment and subsequent identification of protein termini by mass spectrometry and Edman sequencing (Fig. 3.7 a) demonstrates that all protein termini except the VipB C-terminus are accessible for the protease. Especially the VipB N-terminus which is digested until residue 64 is protease-sensitive. Furthermore, a light-scattering recording shows that the turbidity increases during the digestion process (Fig. 3.7 b), which suggests that VipA/B are aggregating when treated with trypsin. This is confirmed by negative stain EM of VipA/B tubules before (Fig. 3.7 c) and after (Fig. 3.7 d) trypsin treatment.

In the second approach, protein termini are labeled in the VipA/B complex and the complex is investigated on negative stain electron micrographs. Tubules of N-terminally poly-histidine and C-terminally HA-tagged VipA and wild-type VipB provided by A. Mogk and colleagues show specific labeling of the poly-histidine tag with 5 nm Ni-NTA-Nanogold on the ring body of top views (Fig. 3.8 a). However, no labeling is observed on side views of intact tubules. Thus, the N-terminal tag of VipA is only accessible for Nanogold particles at the end of the tubules. The HA-tag of the complex is marked with αHA antibodies on the cogs of tubule top views (Fig. 3.8 b). Unspecifically bound antibody is separated from the sample by ultracentrifugation as described and the specific presence of the antibody in the pellet fraction of HA-tagged complexes is assured by detection with anti-αHA antibody on Western blots of precipitated gradient fractions. The orientation of the VipB C-terminus is investigated in VipA/VipB-YFP tubules.

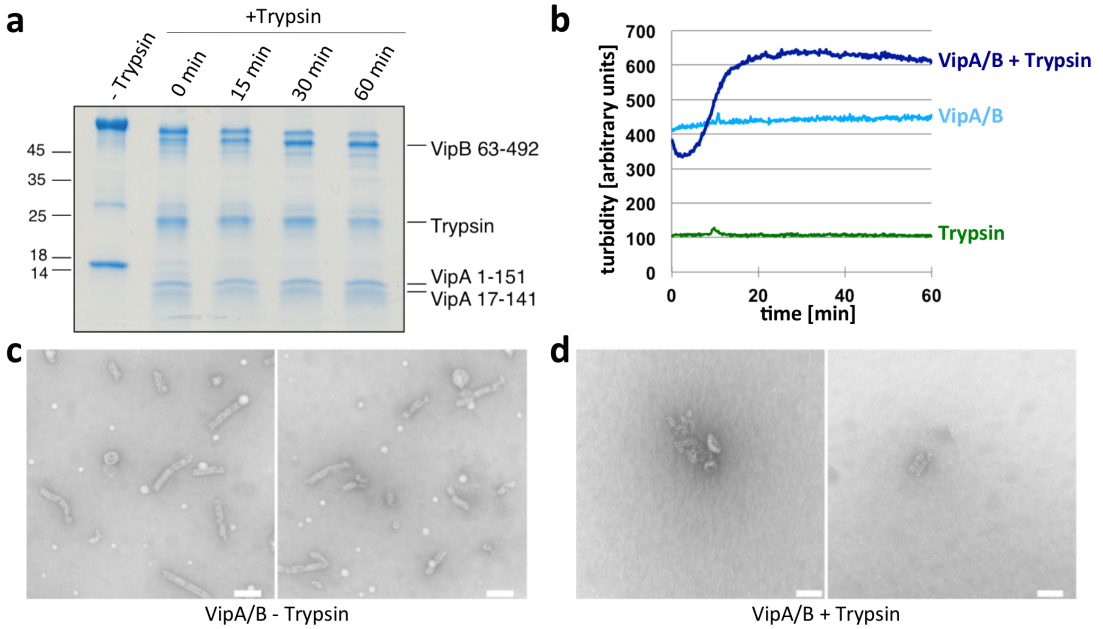

Fig. 3.7: Analytical tryptic digest of VipA/B tubules. (**a**) VipA/B tubules are digested with trypsin and samples are analyzed by SDS-PAGE at indicated time points. Identities of degradation products at 60 min are asserted by mass spectrometry and N-termini are identified by Edman-sequencing. (**b**) Turbidity of VipA/B +/- trypsin and trypsin alone is measured over time. (**c**, **d**) VipA/B tubules are analyzed by negative-stain electron microscopy before and after 90 min trypsin treatment. The experiments presented in this figure have been performed by Axel Mogk and Nicole Kapitein at the DKFZ Heidelberg. The figure is reproduced from Kube et al. 2014, please see also section 6.3 Reprints.

Class averages from multi-variate statistical analysis of top views of this complex show additional density in the central cavity attributed to the C-terminal YFP fusion of VipB (Fig. 3.8 c). As a summary of the experiments, VipA termini are accessible from the outside of the tubule while the C-terminus of VipB points into the central cavity of the tubule (Fig. 3.8 d).

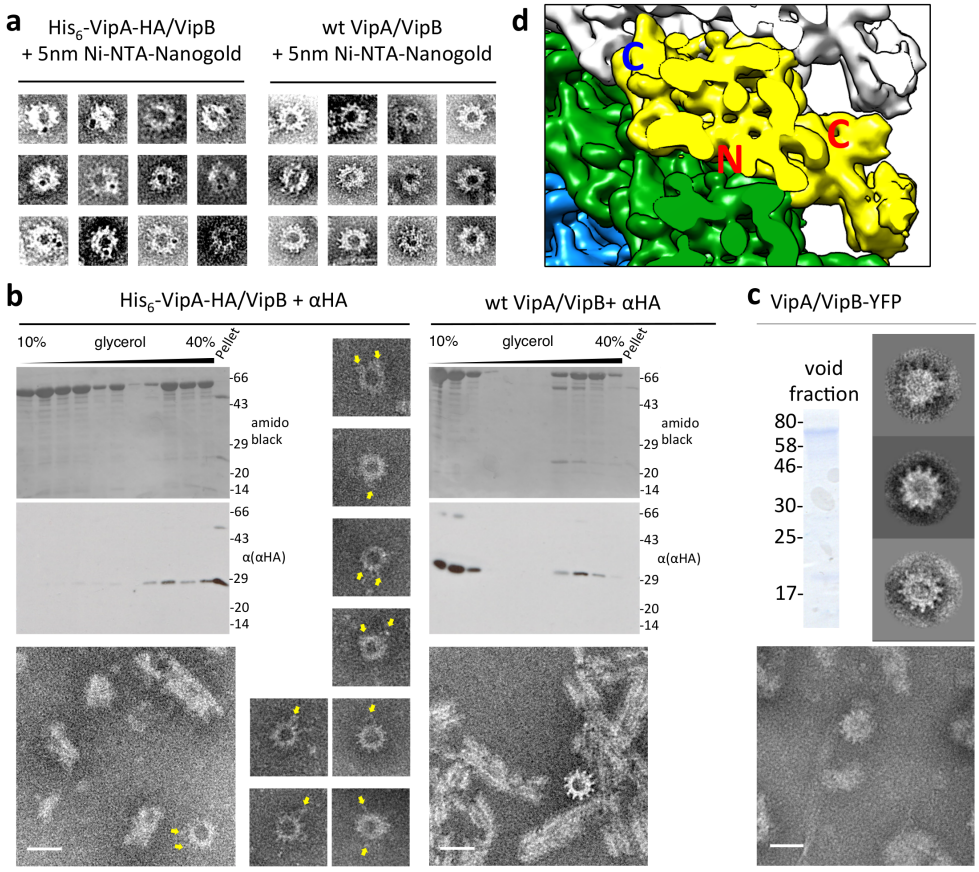

Fig. 3.8: Localization of protein termini in VipA/VipB tubules. (**a**) Wild-type and His_6-VipA-HA/VipB are labelled with 5 nm Ni-NTA-Nanogold (Nanoprobes Inc.) and investigated in negative stain electron microscopy. (**b**) Wild-type and His6-VipA-HA/VipB are labelled with αHA antibody (Roche Anti-HA High affinity) and pelleted by gradient ultracentrifugation. Proteins on Western blots of the centrifugation profiles are stained with Amido black and the antibody detected with Anti-αHA antibody. Micrographs are taken from the pellet fractions stained with Nano-W (Nanoprobes Inc.). αHA antibodies are marked with yellow arrows on the micrographs. Scale bars correspond to a length of 30 nm. (**c**) VipA/VipB-YFP are purified by gel filtration and void fraction analyzed by SDS-PAGE (upper left). Top views taken from micrographs (below) of negatively stained VipA/VipB-YFP are classified after multi-variate statistical analysis. Classes are represented as sums of class members (upper right). The experiment has been performed by J. Albrecht. (**d**) Approximate localization of VipA N- and C-terminus (red) and VipB C-terminus (blue) in the reconstruction as seen in a cut-open view. Figures a-c are adopted from Kube et al., 2014, please see also section 6.3 Reprints.

3.3.2 Homology modeling

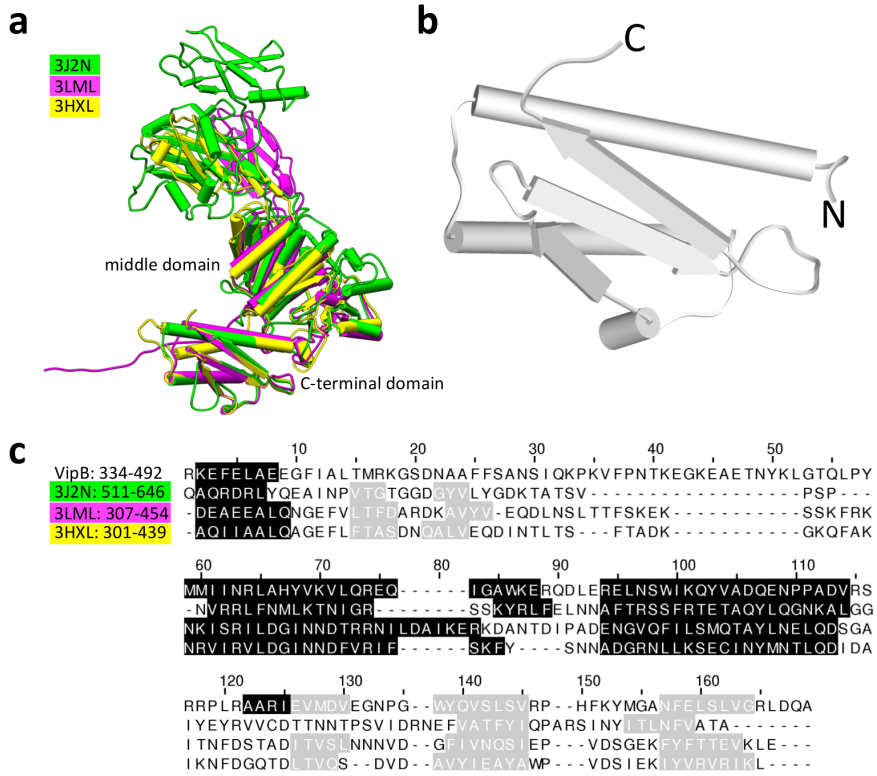

Fig. 3.9: Predicted homologies of the VipB C-terminal region to viral tail sheath proteins. (**a**) Known viral tail sheath protein structures 3J2N (green), 3HXL (magenta) and 3LML (yellow) are overlaid and show a conserved fold in the C-terminal and middle domains [Aksyuk et al., 2011]. This figure is adopted from Kube et al., 2014, please see also section 6.3 Reprints. (**b**) Structural homology prediction using HHpred [Söding, 2005] results in a homology model of the VipB C-terminal domain (389-492 aa) based on (c). (**c**) Alignment of C-terminal sequences of VipB (334-492 aa), 3J2N (511-646 aa), 3LML (307-454 aa) and 3HXL (301-439 aa). Helical regions in the structures and the model are underlaid in black and beta strand regions in gray.

Structural similarities have been detected between the C-terminal regions of VipB orthologues HsiC1-3 in *P. aeruginosa* and the gp18 family of viral tail sheath proteins which share a conserved fold in the C-terminal and middle domains [Aksyuk et al., 2011, Leiman and Shneider, 2012, Lossi et al., 2013]. Accordingly, based on an alignment of the C-terminal regions of VipB (334 - 492 aa) and the viral tail sheath proteins gp18 (511 - 646 aa, 3J2N), LIN1278 (307 - 454 aa, 3LML) and DSY3957 (301 - 439 aa, 3HXL), a homology model of the C-terminal domain of VipB (389 - 492 aa) is predicted in HHPred and Modeller (Fig. 3.9) [Söding, 2005, Webb and Sali, 2014]. The partial structural similarity of VipB to viral tail sheath proteins is

subsequently used to segment the EM map, to confirm the hand of the reconstruction and to build a full secondary structure model of the VipA/B protomer.

3.3.3 Hand confirmation

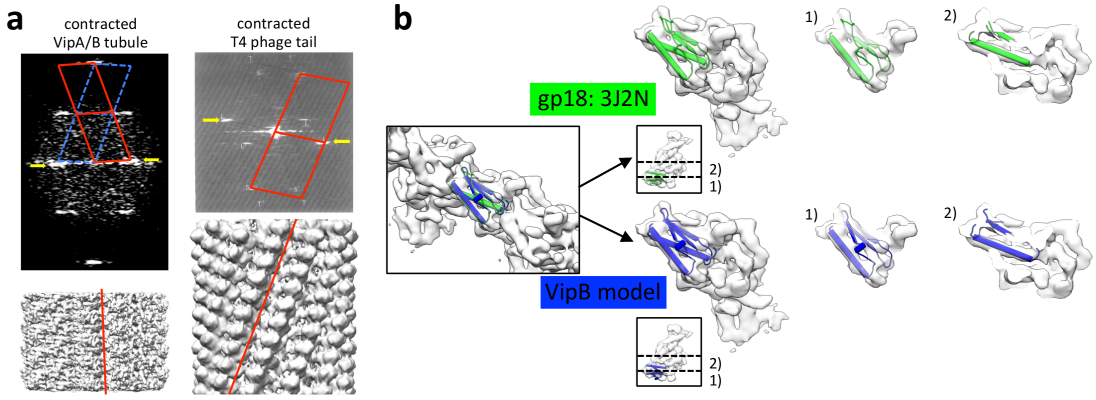

Fig. 3.10: Hand of the reconstruction. (**a**) The layer lines (*upper image,* yellow arrows) in the Fourier transform of VipA/B tubules (*upper left*) defining the left-handed helical ridges (*lower left:* red line) show opposite handedness to the corresponding reflections in Fourier transforms of images of the contracted T4 phage tail (*upper right*, adapted from Moody [1967], please see also section 6.3 Reprints) with right-handed helical ridges (lower right, EMD-5528). The Fourier transforms are overlaid by the near and the far side of the helical net marked in red and blue, respectively. (**b**) The C-terminal domain of gp18 (552-646 aa, green) and the structurally homologous C-terminal domain of VipB (389-492 aa, blue) fit equally well into the density corresponding to one VipA/B subunit of the right-handed VipA/B reconstruction shown in slices at the indicated positions.

As mentioned before, the surface ridges on the contracted VipA/B tubule show opposite handedness to a previously published tomogram. The correct hand of the reconstruction is confirmed by two observations. Firstly, the first layer line in the Fourier transform of the VipA/B tubules that defines the surfaces ridges is handed oppositely to the corresponding layer line in a Fourier transform of contracted T4 phage tails (Fig. 3.10 a, reproduced from Moody [1967]). Likewise, the surface ridges on both structures are handed oppositely - i. e. even though both structures are right-handed, the contracted VipA/B tubule bears left-handed surface ridges while the ridges on the contracted T4 phage tail are right-handed. Secondly, the C-terminal domain of gp18 fits only into the protomer density of the right-handed VipA/B reconstruction (Fig. 3.10 b).

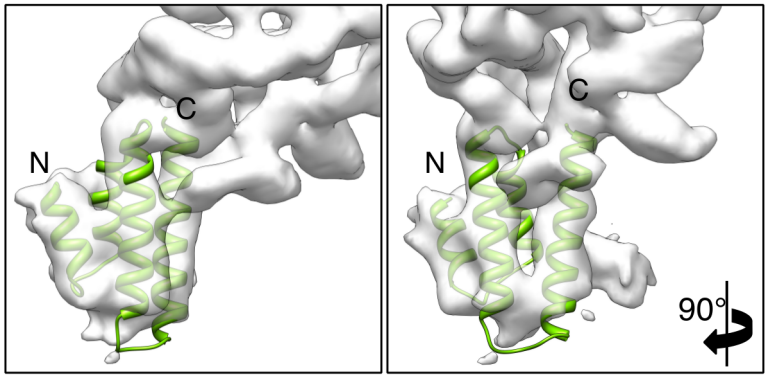

Fig. 3.11: Predicted structure of the VipB N-terminus. The N-terminal region of VipB (1 - 85 aa) forms a 4-helix bundle as predicted by Quark [Xu and Zhang, 2012] which fits well into the density formed by the cog of the density. The protomer is shown from the side (*left*) and as seen from inside of the tubule (*right*). This figure is adapted from Kube et al. 2014, please see also section 6.3 Reprints.

3.3.4 Secondary structure model

The density of one protomer is segmented from a protofilament by overlaying the gp18 structure 3J2N with the EM density based on the localization of the homologous C-terminal domains in the density. The protomer density measures approximately 90 Å from top to bottom and is approximately 55 Å wide (Fig. 3.12 a). Furthermore, the overlay shows that the structural similarity extends beyond the C-terminal domain in VipB (VipB-C). The gp18 middle domain (gp18-M) architecture resembles the middle region up to Helix HB6 of VipB (VipB-M) (Fig. 3.12 b, c). However, the protease-resistant insertion domains gp18-PRFI/II have no correspondence in VipB. As a consequence, the gp18 core structure including the gp18-C and gp18-M is used as a template to trace the VipB peptide chain of VipB-C and VipB-M (170 - 492 aa).

Ab initio modeling of the VipB N-terminus (VipB-N, 1 - 85 aa) using Quark [Xu and Zhang, 2012] results in a 4-helix bundle that fits very well into the density forming the cog region of the protomer (Fig. 3.11). A well defined α-helical density corresponding to helix HB5 connects VipB-M with VipB-N. Modeling of VipA into the remaining density is guided by the long helix HA3 that spans 25 residues. The only position that can hold this long helix is the large helical density above HB4 and HB5 crossing the connecting density between the core of VipB and the cog region. Following the trace of VipA, the β strand rich N-terminal region is in contact with HB11 and the central β sheet region of VipB-M consisting of strands SB4 to SB6.

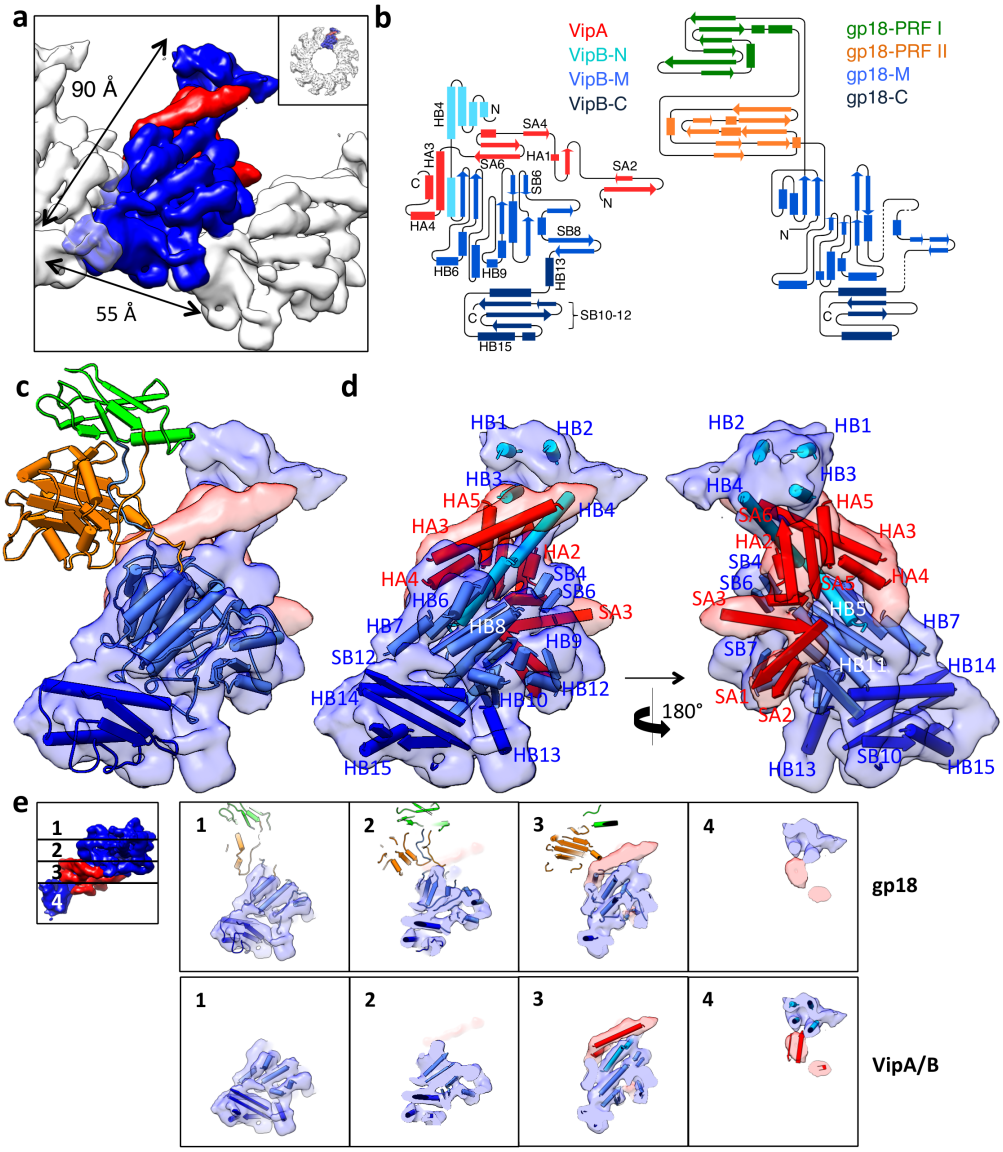

Fig. 3.12: Subunit architecture and secondary structure model of the VipA/B protomer. (**a**) One protomer in an isolated protofilament of the VipA/B tubule is segmented into densities attributed to VipA (red) and VipB (blue) as seen from the top. (**b**) The VipA/B protomer and gp18 (derived from 3J2N) are presented as topology diagrams. VipA and VipB are color-coded as follows: VipA, red; VipB N-terminal segment, cyan; VipB middle segment, blue; VipB C-terminal segment, dark blue. The color code for gp18 is as follows: protease-resistant fragment (PRF) I, green; PRF II, orange; middle segment, blue; C-terminal fragment, dark blue. This figure is adopted from Kube et al. 2014, please see also section 6.3 Reprints. (**c**) The secondary structure model of the VipA/B protomer is color-coded as in (b) and secondary structure elements are labeled as in figure 3.13. (**d**) gp18 (3J2N) is fitted into to the protomer density. (**e**) Slices of the VipA/B model (left) and gp18 (right) fitted into the density as depicted in the small inset.

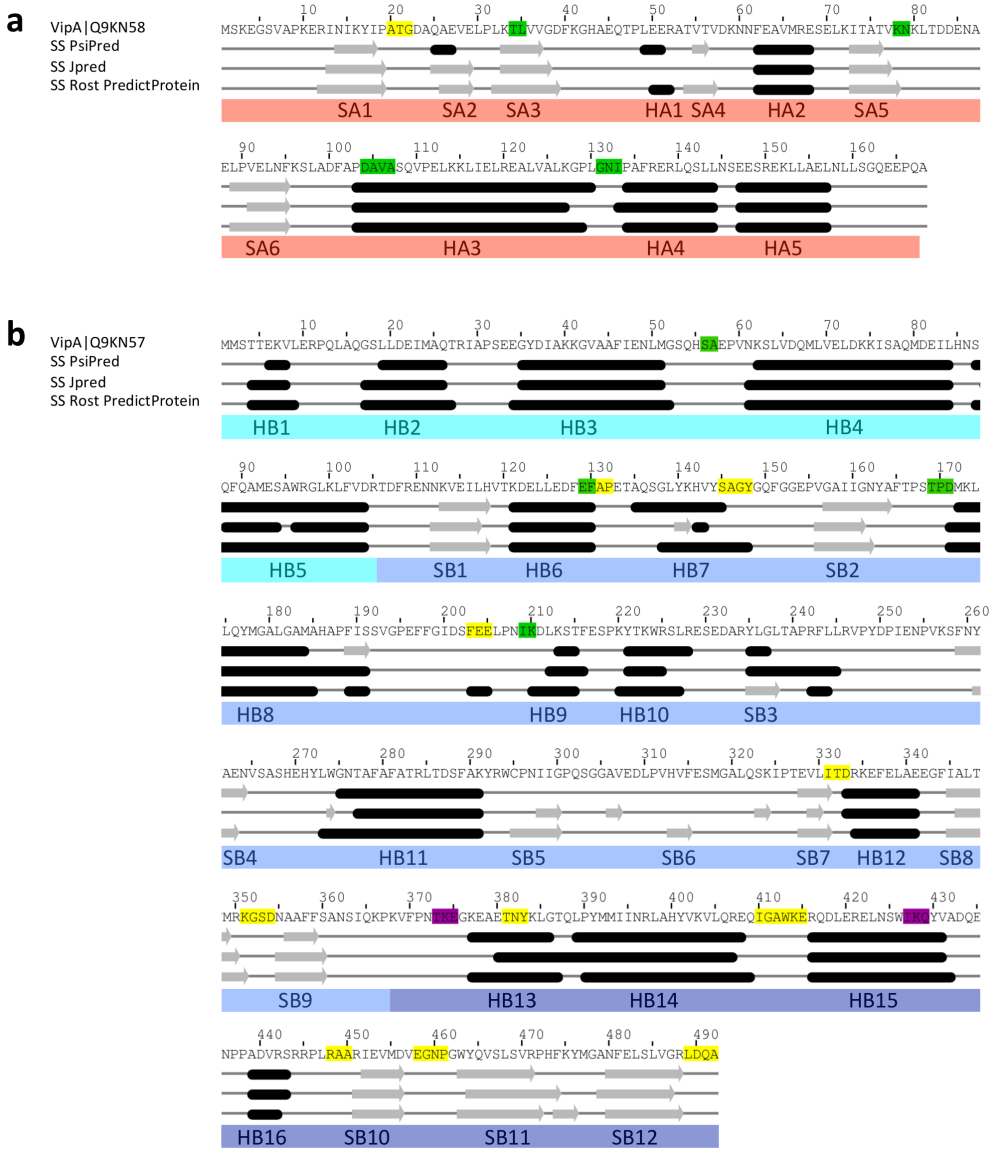

Fig. 3.13: Predicted secondary structure profiles of VipA and VipB. Secondary structure predictions for (**a**) VipA and (**b**) VipB are obtained from PsiPred [Buchan et al., 2013], JPred [Cole et al., 2008] and PredictProtein [Rost et al., 2004] prediction servers. β sheets are depicted in gray and α helices in black. Helices (H) and sheets (S) are numbered as Hx# and Sx# and color-coded as follows: VipA, red; VipB N-terminal segment, cyan; VipB middle segment, blue; VipB C-terminal segment, dark blue. Residues of the VipA and VipB sequences that are deduced to be involved in protomer-protomer contacts in the contracted VipA/B tubules are colored according to figure 3.15. Intra-protofilament contacts are colored in yellow, interprotomer contacts between consecutive rings in magenta and inter-protomer contacts between protomers that come to lie on top of each other in the contracted VipA/B tubule in green. This figure is adopted from Kube et al., 2014, please see also section 6.3 Reprints.

Helices HA4 and HA5 on the C-terminal region of HA3 are folded back underneath HA3 bringing the C-Terminus of VipA into close proximity to N-terminus of VipB. The close proximity of the C-terminus of VipA to the N-terminus of VipB is consistent with the existence of a fusion variant of the two proteins which is observed in some proteobacteria such as *Hylemonella gracilis* and *Burkholderia glumae*. Additionally, this fit also agrees with previously published interaction data between HA3 and VipB [Bröms et al., 2009, 2013, Zhang et al., 2013].

A full secondary structure model of the protomer (Fig. 3.11 d) is built placing secondary structure elements as predicted by PredictProtein [Rost et al., 2004](Fig. 3.13) following the traces of the two proteins. Comparing the model and gp18 in an overlay with the VipA/B protomer as presented in Fig. 3.12 e illustrates the similarities in domain architecture in the C-terminal and middle domains of the proteins which diminishes until the unique VipB-N and gp18-PRFI/II domains.

3.3.5 Model validation

The model is validated independently by chemically cross-linking lysines (VipA contains 14, VipB 29 lysines) with isotope-labelled Di-sulfo-succinimidyl-glutarate (DSSG) and mass spectrometric identification of cross-linked peptides (XL-MS) in wild-type VipA/B tubules and two C-terminal VipB truncation mutant complexes, VipA/VipBΔC^{210} and VipA/VipBΔC^{367}. In the truncation mutants, VipB still interacts with VipA but tubule formation is impaired. To find optimal cross-linking conditions in which most lysines form cross-links but few mono-links are formed, DSSG is titrated (Fig. 3.14 a-c) and samples investigated in SDS-PAGE and silver staining. With increasing cross-linking reagent concentration, indicated bands corresponding to monomers are disappearing, while bands at the expected molecular weight of VipA/VipB heterodimers (×) are appearing in case of the VipB truncation proteins. Multimeric wild-type VipA/B complexes do not form a significant amount of VipA/B heterodimers when cross-linked, as bands at the expected molecular weight are faint or non-existent. Here, the attenuation of the monomeric bands is taken as a criterium for the selection of cross-linking conditions. For the wild-type complex, cross-linking conditions with 0.1 mM and 0.4 mM DSSG are selected, while the truncation complexes are cross-linked with 0.4 mM DSSG.

Table 3.2: Summary of cross-link distances x in the secondary structure model of the VipA/B protomer.

distance x	# cross-links
x < 21 Å	36
21 Å < x < 31 Å	28
not consistent	1

XL-MS analysis performed by T. Zimniak and F. Herzog reveals that in VipA 13 out of 14 lysines react with the reagent in the form of mono- or cross-links and in VipB 24 of 26. In total, 83 cross-links are obtained, out of which 65 are distinct: 34 VipA-VipA, 19 VipA-VipB and 12 VipB-VipB cross-links. 36 cross-links correspond to Cα-Cα distances between cross-linked lysines below 21 Å which is consistent with the linker length of 7.7 Å plus two times the length of a lysine side chain (6.5 Å). Furthermore, 28 cross-links cover distances between 21 Å and 31 Å. This more tolerant distance threshold takes into account hat the VipA/B protomer model is based on a secondary structure prediction in which shifts in the register of individual elements are possible and lysines are occurring in flexible loop regions that cannot be placed reliably into the map. Only one VipA-VipA cross-link representing a homodimer of soluble VipA is not consistent with the model. Consequently, it is concluded, that the obtained cross-links generally support the presented secondary structure model. Especially, lysines K100 in HB5 and K291 in HB11 that form hubs in the cross-link network show multiple connections to lysines in the N-terminal region of VipA and the C-terminal regions of VipB (Fig. 3.14 d, left). Also, three cross-links between helix HA3 (103 - 127 aa) of VipA and HB3 and HB4 of VipB are consistent with a proposed interaction between HB3 and HB8 of VipB and VipA (Fig. 3.14 d, right) [Aubert et al., 2010]. Cross-link distances are summarized in table 3.2. A complete account of all detected cross-links and their corresponding distances in the protomer model is presented in section 6 Appendix, table 6.1.

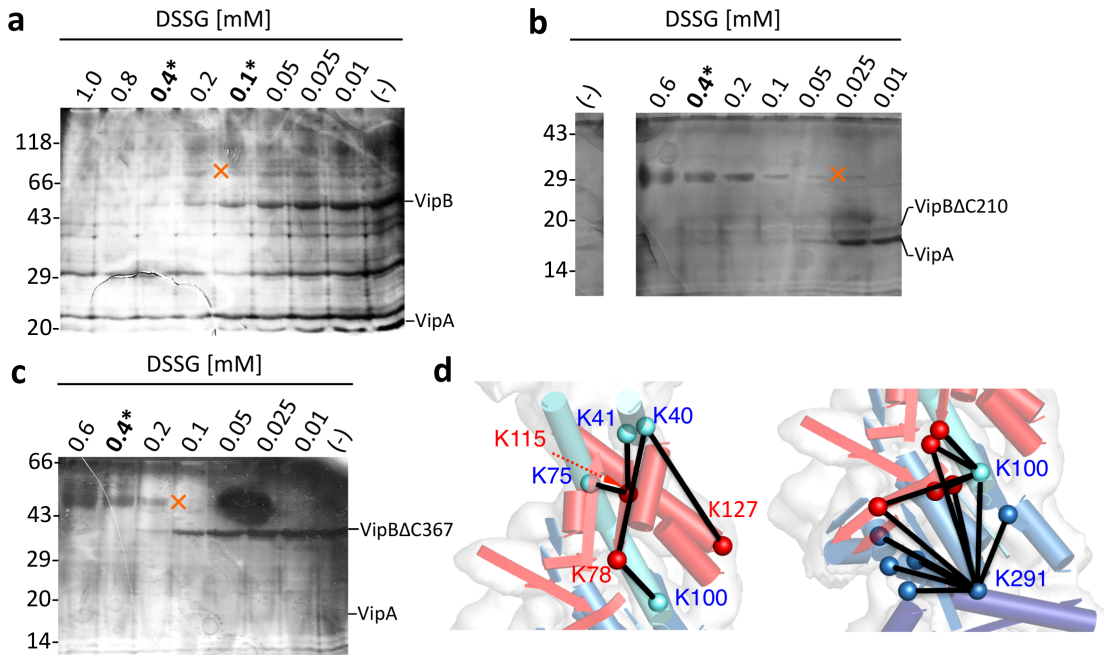

Fig. 3.14: Cross-link mass spectrometric (XL-MS) analysis of wild-type VipA/B tubules, VipA/VipBΔC^{210} and VipA/VipBΔC^{367}. (**a**) Wild-type VipA/B tubules, (**b**) VipA/VipBΔC^{210} and (**c**) VipA/VipBΔC^{367} are treated with DSSG H6/D6 at the indicated concentrations and analyzed by silver-stained SDS-PAGE. Cross-linked heterodimers are indicated (×). Marked samples (*) were subjected to XL-MS analysis. (**d**) *left*: Inter-protein cross-links between VipA and the N-terminal segment of VipB observed in either of the samples are depicted as black lines between Cα atoms of lysines shown as spheres. *right*: Inter- and intraprotein cross-links of VipB lysines K291 and K100 of the samples analyzed are depicted as described above. The secondary structure model of the VipA/B protomer is depicted as in Figure 3.12. This figure is adopted from Kube et al., 2014, please see also section 6.3 Reprints.

3.4 Interprotomer contacts in the contracted VipA/B tubule

Using the validated protomer model, interprotomer contacts are analyzed to elucidate the function of VipA and VipB in the contractile tubule (Fig. 3.15 a-c). Taking into account the total contact area, the architecture of the tubule is largely defined by contacts between neighboring VipB-C domains within a protofilament (yellow marks, Fig. 3.15 a, 3.13) thereby stabilizing the structure. Furthermore, the N-terminus of VipA is located at the interface between protomers (cyan circle, Fig. 3.15 a). The protofilaments are interconnected vertically and also diagonally. Protomers that come to lie directly on top of each other form contacts involving densities attributed to the β sheet rich N-terminus, the long helix HA3 and the connecting loop to HA4 in VipA, and loops between HB7 to HB9 in VipB (green marks, Fig. 3.15 a,b, 3.13). Consecutive hexameric rings are connected diagonally by interprotomer contacts involving HB15 and loop region N-terminal of HB13 (magenta marks, Fig. 3.15 a-c, 3.13).

The latter diagonal contact is supported by *in vitro* cross-linking experiments using engineered cysteines at E375 in the loop region before HB13 and Q429 in HB15 (inset, Fig. 3.15 c). When the double mutant VipA/VipB(E375C/Q429C) is treated with the oxidant copper phenanthroline (CoPhe), the non-reducing SDS gel shows bands at a higher molecular weight where cysteine cross-linked VipB multimers are expected. The VipA/VipB(Q429C) strain has been created by N. Kapitein and A. Mogk who also have purified and analyzed the mutant proteins. Additionally, XL-MS analysis of the cross-linked wild-type VipA/B tubules revealed four cross-link pairs that are more compatible with interprotomer contacts concerning their bridged Cα-Cα distances (Fig. 3.15 d).

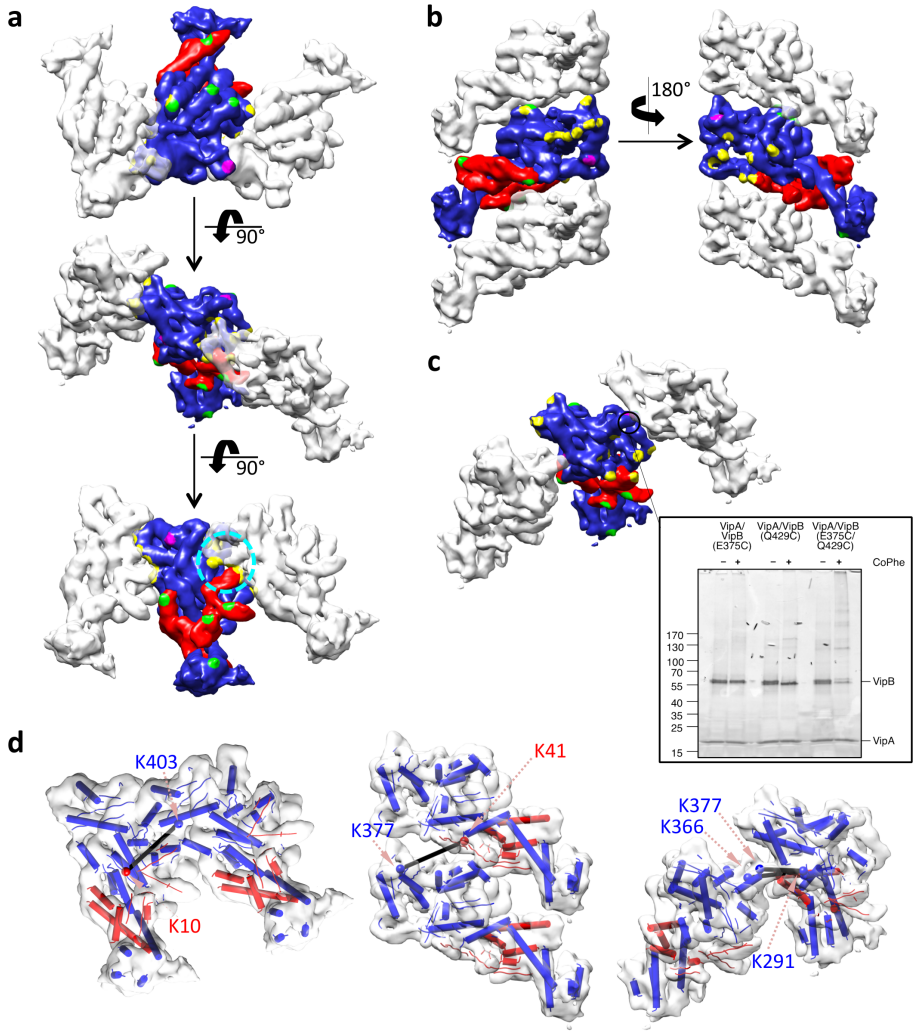

Fig. 3.15: Interprotomer contacts in contracted VipA/B tubules. (**a**) Intra-protofilament contacts in neighboring VipA/B protomers map are shown as top view, inside-out and bottom view. The middle protomer is segmented into VipA (red) and VipB (blue) densities. The VipA N-terminus is marked with a cyan circle. (**b**) Interprotofilament contacts between protomers that lie on top of each other are presented as side views. (**c**) Interprotofilament contacts between protomers of neighboring protofilaments are depicted as seen from inside the tubules. These contacts are investigated in VipA/VipB-E375C/Q429C single and double mutants under reducing (- copper phenanthroline, CoPhe) and oxidizing (+ CoPhe) conditions by non-reducing SDS-PAGE (c, inset, the experiment was performed by Nicole Kapitein and Axel Mogk at the DKFZ Heidelberg). Contact areas for protomer-protomer contacts are highlighted as follows: yellow, intraprotofilament contacts as seen in (a); green, interprotofilament contacts as seen in (b); magenta, interprotofilament contacts as seen in (c). (**d**) Intra-protofilament (left) and interprotofilament (middle and right) cross-links as detected in the cross-linking-MS analysis of wild-type VipA/B tubules. Two protomers with fitted secondary structure elements of VipA (red) and VipB (blue) are shown in the same orientations as seen in (a–c). The Cα atoms of cross-linked residues are depicted as spheres and lines indicate cross-links. The figure is reproduced from Kube et al., 2014, please see also section 6.3 Reprints.

3.5 Interaction with the AAA+ ATPase ClpV

The T6S system is a one-shot system that is at least partially disassembled by the AAA+ ATPase ClpV after a contraction event. ClpV binds to a specific recognition motif in helix HB2 at the N-terminus of VipB via its N-terminal domain and disassembles the contracted VipA/B tubule [Pietrosiuk et al., 2011]. Even though ClpV is not essential for T6S, T6S-dependent pathogenecity is attenuated in ClpV-defective mutants [Zheng et al., 2011, Basler et al., 2012]. Thus, the exact binding site of ClpV on the VipA/B tubule is examined in three experiments.

Firstly, co-purified His_6-ClpV-N and VipA/B are cross-linked with glutardialdehyde in a GraFix gradient [Kastner et al., 2008]. Analyzing the gradient fractions by SDS-PAGE and Western blot shows, that His_6-ClpV-N is detected in all gradient fractions whereas His_6-ClpV-N multimers appear only in the upper gradient fractions (Fig. 3.16 a). Typical VipA/B top views are visible on negative stain electron micrographs of the pellet fraction (Fig. 3.16 b) and multivariate statistical analysis of a negative stain dataset results in top view class averages with a additional density in between the cogs of the VipA/B top view (yellow arrows, Fig. 3.16 c).

Secondly, VipA/B tubules are decorated with hexameric complexes of full-length ClpV in the presence of slowly hydrolyzing ATPγS [Bönemann et al., 2009] . Class averages of a negatively stained dataset show that the ATPase is in close contacts with cogs of the tubule (Fig. 3.16 d).

In a third experiment, cysteines are introduced into ClpV-N and the ClpV binding motif of VipB based on the published structure of the ClpV-N and the corresponding peptide of VipB (Fig. 3.16 e) [Pietrosiuk et al., 2011]. Mutants ClpV-N(A86C) and VipA/VipB(T27C) have been created and purified by A. Pietrosiuk and A. Mogk. SDS-PAGE analysis shows that the cysteine cross-link is dissolved under reducing conditions (Fig. 3.16 f). Comparing class averages of wild-type tubules and the cross-linked sample in an overlay shows additional density attributed to ClpV-N(A86C) at the cogs in top views and at the tubule wall in side views (Fig. 3.16 g). Together with the VipA/B protomer model, these results show, that the N-terminal ClpV recognition motif of VipB is located in the cogs forming the surface ridges of the contracted tubule.

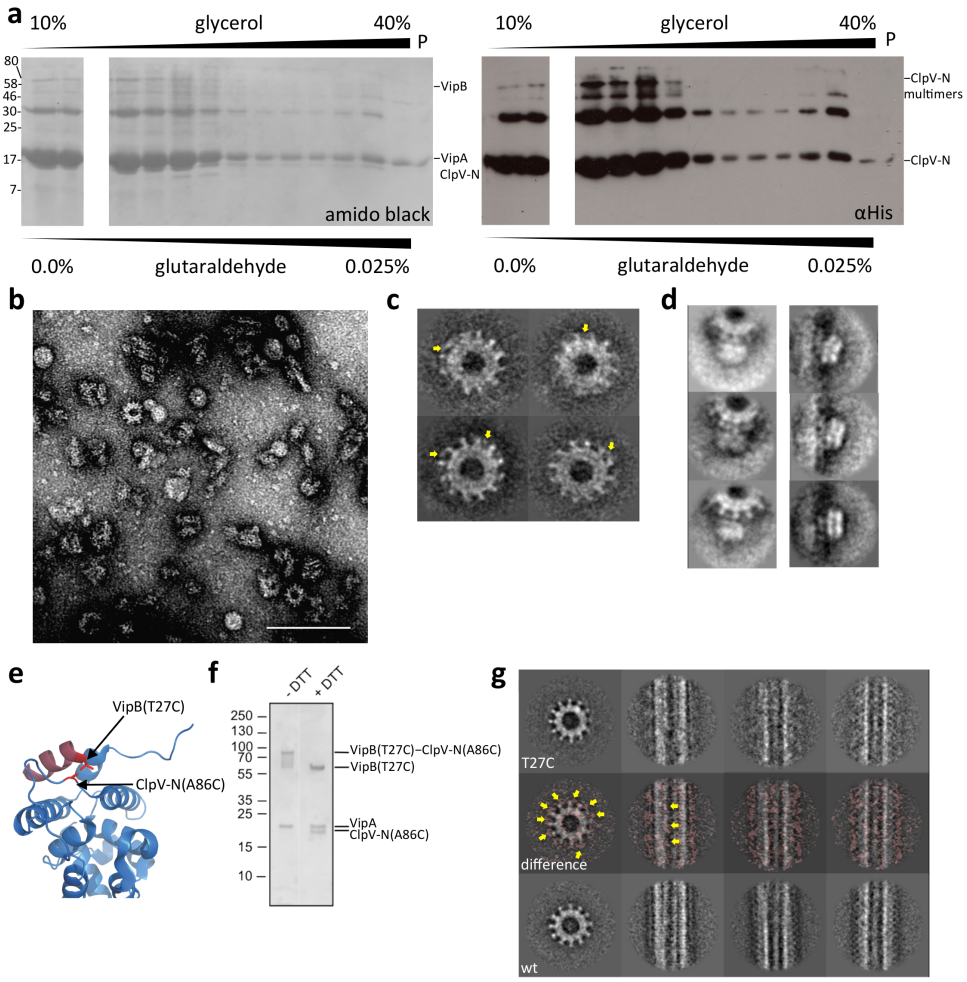

Fig. 3.16: Localization of the interaction site of ClpV on the VipA/B tubule. (**a**) VipA/B complexes co-purified with ClpV-N by IMAC are treated with the GRAFIX method [Kastner et al., 2008] on a 10% - 40 % glycerol and 0.0 % - 0.025% (v/v) glutardialdehyde gradient. TCA-precipitated gradient fractions are examined on a Western blot (*left:* Amido black stain, *right:* detection with αHis antibody, P: pellet fraction). The experiment has been performed by T. Hassler. (**b**) Micrograph of the pellet fraction stained with 2% uranyl acetate. (**c**) Classes from multivariate statistical analysis of negatively stained VipA/B top views from the pellet fraction represented as class sums. (**d**) VipA/B tubules bound to ClpV in the presence of ATPγS in negative stain are presented as class averages (*left:* top views, *right:* side views) derived from multivariate statistical analysis. (**e**) The location of cysteine residues used for cross-linking between VipB (red) and the N terminus of ClpV (blue) are shown on the basis of the crystal structure PDB ID 3ZRJ. (**f**) The reduced and oxidized (±DTT) VipA/B/ClpV-N assemblies are analyzed by non-reducing SDS-PAGE. The experiment has been performed by Nicole Kapitein and Axel Mogk at the DKFZ Heidelberg. (**g**) Multivariate statistical analysis of VipA/B tubules cross-linked to ClpV-N (*upper row*). The images were binarized and overlaid with images of class averages of negatively stained wild-type VipA/B tubules (*middle row*). Additional density is colored in red and indicated by yellow arrows. Class averages of negatively stained wild-type VipA/B tubules (*lower row*). Figures d-f are reproduced from Kube et al., 2014, please see also section 6.3 Reprints.

3.6 Comparison to the T4 phage tail sheath: model of the elongated VipA/B tubule

It is proposed that the T6S tubule formed by VipA and VipB is a functional homologue of bacteriophage tail sheaths [Basler et al., 2012] of which the T4 phage tail is characterized the most thoroughly [Leiman and Shneider, 2012]. In this work, it has been shown that VipB-C and VipB-M share also structural similarities to gp18 proteins. To visualize the protomer arrangement in the T4 phage tail, the hexameric gp18 model 3J2N [Fokine et al., 2013] is overlaid with the EM map of the contracted T4 tail sheath (EMD-1086, Leiman et al., 2004). Additionally, gp18-C and gp18-M domains represented as low-pass filtered electron density maps are fitted into three consecutive rings of the tail sheath and the T6S tubule into three consecutive rings. Comparing the two systems in their contracted states shows that the T4 phage tail contracts to a greater extent (Fig. 3.17 a). While the inner diameter of the T4 tail sheath extends from 100 Å to 150 Å, the T6S tubule widens from 95 Å only to 110 Å. However, the relative positions of the C-terminal and middle domains are very similar. The PRFI/II domains of T4 tail sheath proteins gp18 are pointing outwards like the T6S-specific VipB-N domain of the VipA/B protomer density which is fitted into VipA/B tubule map and rendered at a high threshold. In contrast to VipB-N in the VipA/B protomer, gp18-PRFI/II domains are turned away from the gp18-M domain giving the protomer a S-shaped appearance when seen from the top.

To test whether the VipA/B tubule reconstruction represents the system in its fully contracted state, the protomer arrangement of two consecutive protomers in a protofilament in the T6S system and T4 phage tail is compared. T4 tail sheath protomers rotate approximately 30 ° in plane upon contraction leading to an opening of the inner cavity of the tail sheath (Fig. 3.18 a). The relative position of VipA/B protomers in the contracted state is similar to those of the T4 tail sheath even though gp18 protomers show an additional rotation around the long axis of the protomer leading to a smaller helical rise of the contracted tail sheath compared to the T6S tubule. A superposition of two VipA/B protomers with gp18 subunits that come to lie on top of each other reveals that VipA/B protomers clash in densities mainly attributed to VipA when the shallower rise of the contracted T4 tail sheath is enforced upon them (Fig. 3.18 b).

Next, it is asked wether the analogies in the contracted states are found in the elongated states, too. For this, VipA/B protomer are overlaid with an EM map of the elongated T4 tail sheath (EMD-1126, Kostyuchenko et al., 2005) based upon the best fit of structurally similar middle and C-terminal domain of gp18 and VipB. It is assumed that only rigid-body movements of the protomers occur during contraction [Leiman and Shneider, 2012]. Generally, the symmetry of the elongated T4 phage tail is compatible with the VipA/B protomer, even though the overall protomer architectures are different in the position of the unique domains VipB-N and

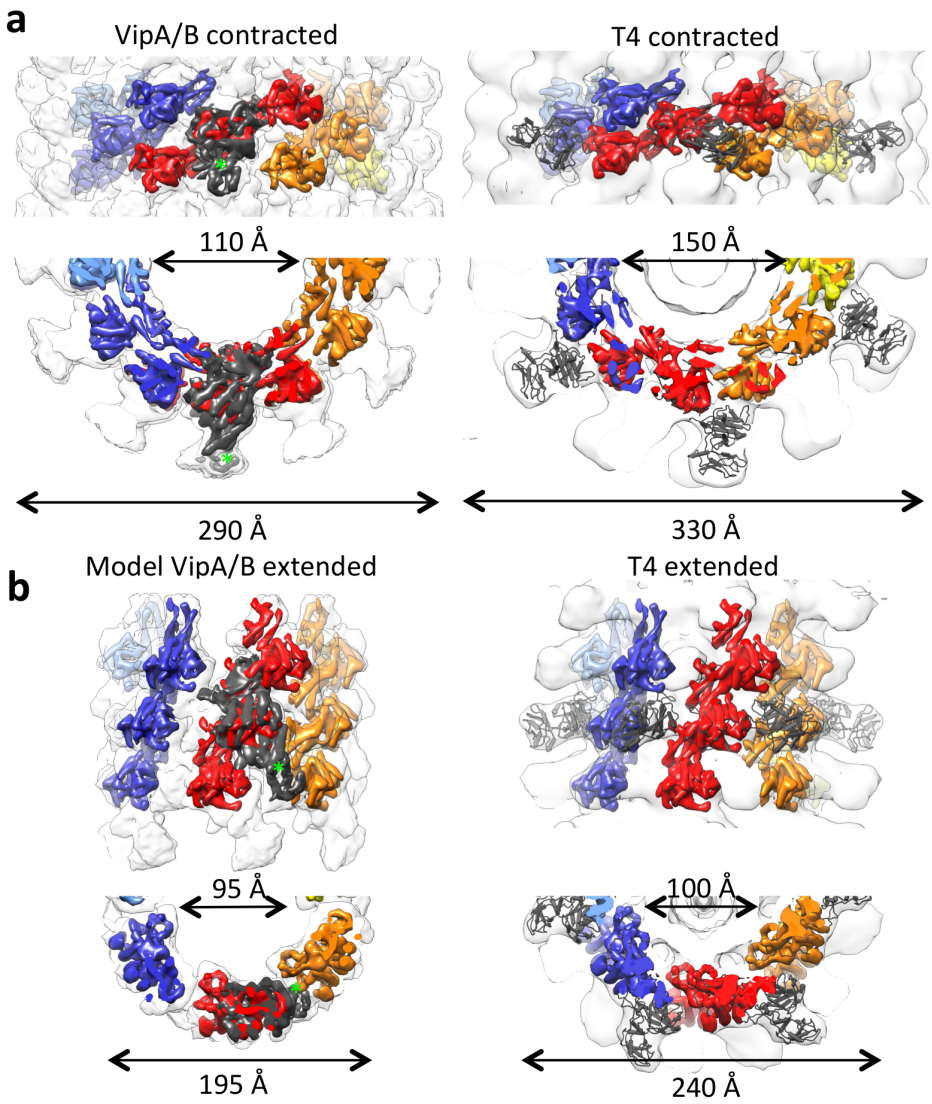

Fig. 3.17: Comparison between contracted VipA/B tubules and T4 phage tail sheaths. (**a**) The contracted VipA/B tubule (*left*) is compared with the contracted T4 tail sheath (EMD-1086; *right*) seen as a side view (*upper row*) and cut-away top view (*lower row*). The hexameric gp18 model (PDB ID 3J2N, gray) is overlaid with the contracted T4 sheath EM map (EMD-1086, transparent white) and shown as a side view (*top right*) and cut-away top view (*bottom right*). The low-pass filtered C-terminal and middle segments of gp18 (colored separately) are fitted into three consecutive rings of the contracted T4 sheath and the VipA/B tubule. One hexameric gp18 model is depicted as gray crystal structure (*right*). One VipA/B protomer is rendered at a high threshold (*left*) to illustrate the overlay and location of HB2 of VipB (green star). (**b**, *right*) C-terminal and middle gp18 segments are fitted into the elongated T4 sheath EM map (EMD-1126). The model of the elongated VipA/B is based on the best fit between these and homologous segments of VipB (*left*). The elongated VipA/B tubule and T4 sheath are shown as side (*upper row*) and top views (*lower row*). The color code of all maps, models and crystal structures is as seen in (a). The figure is adopted from Kube et al., 2014, please see also section 6.3 Reprints.

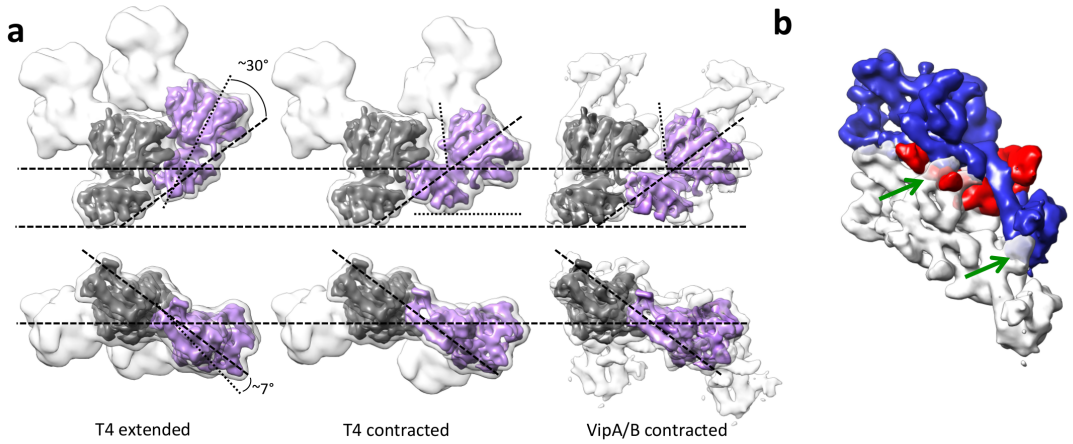

Fig. 3.18: Protomer arrangement in the VipA/B tubule and the T4 sheath. (**a**) Protomer arrangement in protofilaments of extended and contracted T4 tail sheath and VipA/B tubules. Two consecutive protomers are shown as transparent surface. Low-pass filtered C- and M-segments of gp18 are fitted into the densities and colored in gray and purple. All dimers are aligned to the gray gp18 segment. (**b**) Superposition of two VipA/B protomers onto contracted T4 sheath subunits that come to lie on top of each other. One VipA and VipB is colored in red and blue, respectively. Clashes between the protomers are indicated by green arrows. This figure is reproduced from Kube et al. [2014], please see also section 6.3 Reprints.

gp18-PRFI/II, respectively (Fig. 3.17 b). As a consequence of the differing positions, the VipB-N domains with the ClpV recognition motif is buried in the tubule wall while the gp18-PRFI/II domains are still pointing outwards in the elongated states of the tubules.

3.7 Towards the contraction mechanism of the VipA/B tubule

To explore the architecture of the elongated VipA/B tubule, a mutant VipA/B protein is designed, which is speculated to form elongated tubules. As the C-terminal domains are the most conserved parts in both viral tail sheath proteins and bacterial T6S tubules, they are likely involved in their common function. Comparing two VipA/B protomers in their proposed elongated and in their contracted state (Fig. 3.19 a) suggests an involvement of helix HB13 (orange) in the contraction movement. It is located directly in the interface between the VipB C-terminal domains of both protomers and could possibly move more towards the adjacent protomer in the elongated state. By this movement, the 90 ° kink between HB14 and HB13 would be relaxed. At sequence level, a conserved GxxxP motif is located in between the helices which might confer conformational flexibility. However, when investigating a VipA/VipB(P390I) mutant that was purified by IMAC and ultracentrifugation, tubules demonstrated a similar diameter as wild-type tubules, suggesting that they are in a contracted conformation (Fig. 3.19 b).

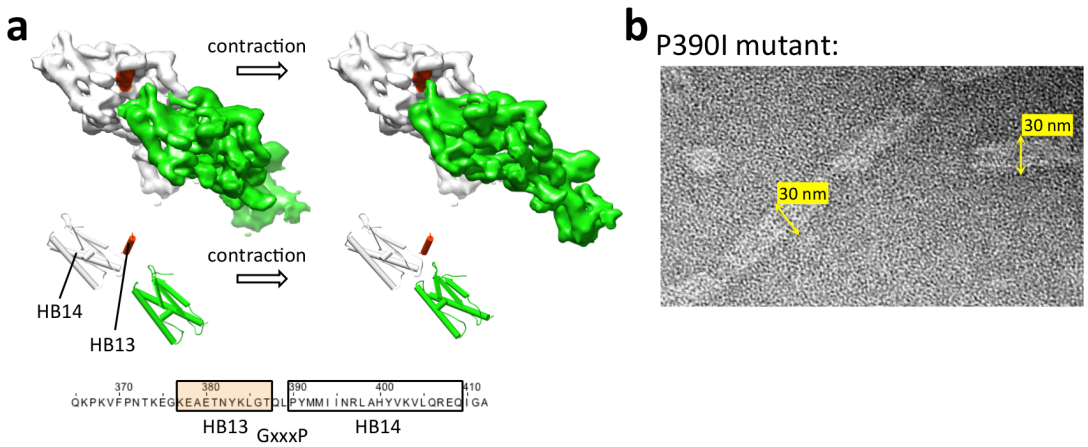

Fig. 3.19: Investigation of VipA/B tubule contraction mechanism. (**a**) *upper image:* Helix HB13 (orange) lies at the interface between adjacent protomers (white, green) in one protofilament. During contraction, protomers putatively rotate inwards, with HB13 at the center of movement; *middle image:* Predicted structures of C-terminal domains of adjacent protomers overlaid into the densities of the protomers in the elongated (*left*) and the contracted state (*right*); *lower image:* sequence of VipB between helices HB13 and HB14 with GxxxP motif in between predicted helices. (**b**) Negative stain micrograph of VipA/VipB (P390I) purified by IMAC and ultracentrifugation. The diameter of the observed tubules is reminiscent of the contracted state.

4 Discussion

Proteins VipA and VipB and their homologues in other bacteria are essential parts of the Type VI secretion system [Bönemann et al., 2009, Basler et al., 2012]. In the current understanding, the two proteins form a contractile tubule holding a needle complex which is ejected and penetrates bacterial membranes to deliver effector proteins. The energy for this action is stored in the elongated form of the T6S tubule as it is in its functional homologue, the bacteriophage tail sheath. However, the structures of VipA and VipB, as well as their assembly and functions in the tubule have not been known so far.

In this work, the contracted T6S tubule of *Vibrio cholerae* is presented at sub-nanometer resolution. In a hybrid methods approach, the VipA/B protomer of the tubule is modeled to the secondary structure level, allowing to compare the bacterial system to its viral counterpart structurally and also to conclude on functional relationships between their components. This results in a model of the VipA/B complex in its elongated state suggesting a mechanism for the observed contraction-state specific disassembly of the T6S tubule [Basler and Mekalanos, 2012].

4.1 The T6S tubule and viral tail sheath have a similar architecture defined by contacts between structurally conserved core regions

It has been shown, that T6S components Hcp, VgrG and VCA0105 are structural and functional homologues of proteins forming the tail tube and the spike of contractile bacteriophages [Leiman et al., 2009, Pell et al., 2009, Shneider et al., 2013]. Additionally, T6S protein TssE is a structural homologue of T4 baseplate wedge protein gp25 [Lossi et al., 2011]. Based on these findings and the appearance of the T6S tubules in negative stain micrographs, it has been suggested that also the T6S tubule is structurally similar to the T4 tail sheath [Leiman et al., 2009, Lossi et al., 2013]. Our cryo EM reconstruction of the contracted VipA/B tubule at sub-nanometer resolution generally corroborates this model.

Both, the T6S tubule and the T4 tail sheath consist of six right-handed protofilaments with similar helical parameters [Aksyuk et al., 2009, Leiman et al., 2010]. At this level of detail, the

main difference between the two systems is the opposite hand of the helical ridges due to the different extent of contraction. In the T6S tubule, the helical arrangement is largely governed by contacts between the C-terminal domains of VipB. The deletion of the C-terminal domain in the *P. aeruginosa* homologue completely abrogates tubule formation [Lossi et al., 2013]. This also holds true for the *vc*VipA/VipBΔC367 protomers as we confirmed in this study. A similar role in maintaining the integrity of the phage tail is also suggested for the C-terminal domain (domain IV) of gp18 [Aksyuk et al., 2009, Leiman et al., 2010, Fokine et al., 2013]. The functional similarity is mirrored in the structural conservation of the core regions comprising C-terminal and middle domains in both proteins. The structural conservation is only weakly detectable on the sequence level for the C-terminal regions [Lossi et al., 2013]. Hence, the parts of the contractile machinery that are dedicated to maintain the integrity of the structure and most likely are involved in the contraction process are conserved.

4.2 Tubule contraction mechanism

These structural similarities between the viral and the bacterial system are used to build a model of the extended state of the VipA/B tubule based on low-resolution EM maps of the extended T4 phage tail. In the extended state, tubule integrity is still maintained by the close interactions between VipB C-terminal domains in the protofilaments albeit the interface between neighboring protomers in a protofilament is changed. Individual protomers of one protofilament are rotated in plane against each other leading to an opening of the contact zone in the contracted state putatively involving loop regions SB10-SB11 and HB14-HB15 of one protomer to loop regions SB11-SB12 and HB13 of the consecutive protomer (Fig. 3.19). Instead, new contacts of SB10-SB11 and HB14-HB15 to β sheets SB8 and SB9 are formed. Additionally, the contact area to the first three N-terminal β strands of VipA is extended making new contacts to VipB-C. Interestingly, a loop region and a β hair pin in gp18 N- and C-terminal of the helix homologous to HB11 that are in the equivalent position to the VipA N-terminal region, have been shown to be crucial for tail sheath polymerization [Aksyuk et al., 2009]. Thus, the VipA N-terminal region which forms intra-protofilament contacts in both states of the tubule might also be involved in maintaining tubule integrity during the contraction process.

Due to VipA, the VipA/B protomer is bigger than gp18 and as a consequence, the T6S tubule can contract less compared to its viral counterpart. Comparing the helical parameters of the contracted forms of both systems shows that the T6S tubule is packed less compact. *In situ* measurements of elongated and contracted VipA/VipB tubules result in a length reduction of 45 % during the contraction while the tubule diameter expands to 126 % of its original width [Basler et al., 2012]. In comparison, the T4 tail sheath contracts by 55 % of its length and ex-

pands to 138 % of its diameter [Leiman et al., 2010]. However, the T6S tubule is generally longer than a phage tail and the reduced contraction ability of the system is more than compensated for by its length. It is assumed that the T6S system which can span a complete bacterial cell, has a maximal penetration length of 500 nm [Ho et al., 2014].

It has been observed that inter-protomer contacts within a protofilament (defined by the C-terminal regions of gp18) of the T4 tail sheath remain overall unchanged during the contraction event, while additional contacts between protomers of neighboring protofilaments are created. This led to the hypothesis that the energy necessary for the contraction is provided by additional inter-subunit binding and the contraction process only involves rigid-body movements of the tail sheath proteins [Aksyuk et al., 2009]. However, the comparative model of the extended VipA/B tubule hints more towards a conformational change in the protomer that drives tubule contraction and there is indirect evidence from spectroscopic data that the gp18 secondary structure content changes during contraction of the T4 tail [Venyaminov et al., 1975]. The C-terminal regions of gp18 and VipB are the most structurally conserved parts in both systems and also positioned at the hinge region between the two states. This makes them an obvious candidate harboring a conformational switch, although initial experiments to localize critical amino acids for the switch failed.

The possibility of linking protomers in a protofilament by “chain-swapping” has been described in section 1.6.2. A fit of the structurally conserved domains IV and III of DSY3957 into the EM density of the contracted and into the model of the elongated VipA/B tubule shows that - if the “chain-swapping” is not an crystallization artifact (“chain-swapping” tail sheath proteins in the crystal are not in a helical arrangement) and also conserved in the T6S system - the tubule geometry would only allow a link between protomers of adjacent protofilaments (Fig. 4.1). A ”chain-swapping” between protomers of the same protofilament is very likely not possible since the swapped peptide chain originating from the inner wall of the tubule cannot reach the C-terminal domain of the subsequent protomer as this domain faces the tubule exterior. However, the linking peptide chain could presumably be accommodated in the connecting density between protomers of neighboring protofilaments.

In the phage, the N-terminus of the tail sheath protein is involved in the “chain-swapping”, but the N-terminus of VipB is oriented towards the outer tubule surface and out of reach. In some bacteria, VipA and VipB occur as a fusion protein in which VipA is located at the N-terminus. This leaves the β strand rich N-terminus of VipA as the remaining possible candidate to take over the role of the DSY3957 N-terminus. Even though the proposed secondary structure model disagrees with this possibility, the obtained cross-link data cannot exclude the alternative fit of VipA under the assumption that the VipA N-terminus is flexible in the VipB truncation mutants.

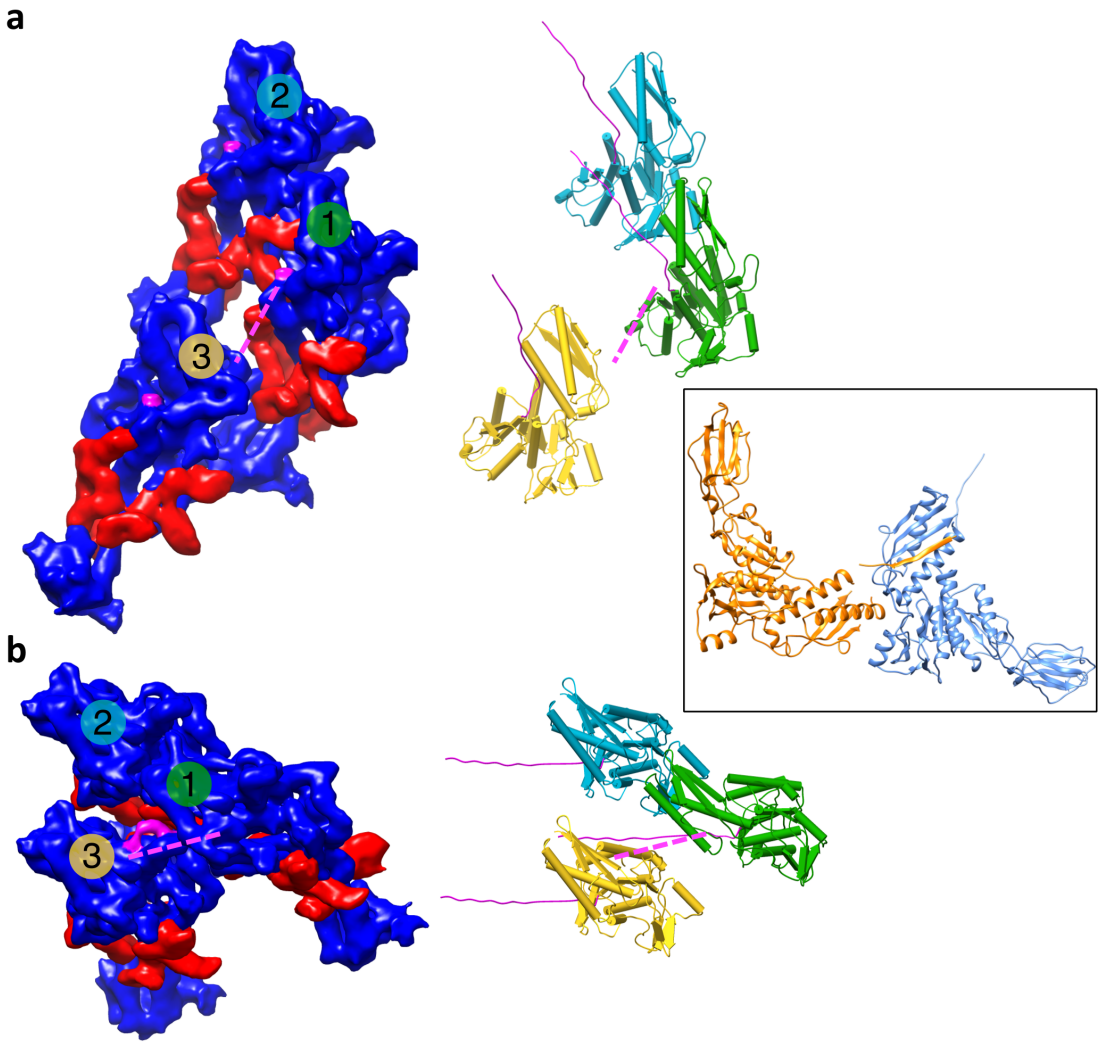

Fig. 4.1: "Chain swapping" hypothesis in the T6S tubule. (a) *left:* Three VipA/B protomer densities are displayed in the arrangement according to the model of the elongated T6S tubule as seen from inside the tubule. Density attributed to VipA in our secondary structure model of the protomer is shown in red, density attributed to VipB in blue. Protomers 1 (green) and 2 (light blue) belong to the same protofilament (contacts as in Fig. 3.15 a) while protomer 3 (yellow) belongs to the adjacent protomer (contacts as in Fig. 3.15 c). The position of the DSY3957 N-terminal β strand when fitted into each protomer is marked in magenta and the connection between neighboring protomers in a possible "chain swapping" model represented as a broken line. *right:* Domains IV and III of DSY3957 structure 3HXL are displayed in the same arrangement. The N-terminal β strand is shown in magenta and the "chain swapping" connection in broken lines. **(b)** *left:* Three VipA/B protomer densities are displayed in the arrangement according to the EM density map of the contracted VipA/B tubule as seen from inside the tubule. Connecting density between neighboring protomer is colored in magenta and marked with a broken line. Color code is defined as in (a). *right:* Domains IV and III of DSY3957 structure 3HXL are displayed in the same arrangement. *Inset:* Chain-swapping of the DSY3957 (3HXL) when symmetry as observed in the crystal is applied.

Yet, it is not clear if the N-terminus of VipA would be accessible for a protease as we have shown in trypsin digestion experiments (Fig. 3.7). Furthermore, Hcp has been shown to interact with homologues of VipA of EAEC and *A. tumefaciens* in co-immunoprecipitation and bacterial two-hybrid experiments [Lin et al., 2013, Brunet et al., 2014]. The interaction site on VipA has not been localized, but according to our model of the eloganted state and the secondary structure model of the protomer, the N-terminal region of VipA faces the tubule interior. In the chain-swapping model involving VipA, the area on VipA to interact with Hcp in the elongated state would be likely smaller, as the N-terminal region of VipA is bound to an adjacent VipB C-terminal domain on the outside of the tubule. In summary, the possibility of the chain-swapping in the VipA/B tubule cannot be completely ruled out, but currently little experimental evidence argues for it.

4.3 VipA and the VipB N-terminal domain are unique adaptions of the T6S

The structure of VipA according to the protomer model is completely unrelated to the viral tail sheath proteins. Thus, its function cannot be deduced from the viral system. In *V. cholerae,* VipB is not stably expressed in the absence of VipA and analytical SEC profiles show that the VipA/B protomer is quickly reassembled after the tubule is taken apart by ClpV in the presence of ATP [Bönemann et al., 2009]. According to two-hybrid data, the interaction is conserved throughout species borders and is mainly mediated by helix HA3 of VipA [Bröms et al., 2009, 2013, Zhang et al., 2013]. Impairing this interaction leads to a reduced stability of VipB and loss of T6S ability [Bröms et al., 2009]. Hence, VipA could serve as a chaperone of VipB. In the proposed structure of the VipA/B protomer, VipA wraps around the connecting helices HB4 and HB5 between the middle region of VipB and the N-terminal domain and has large contact areas to VipB at its termini. Thereby, it stabilizes the likely most flexible parts of the protomer, giving it a rigid structure that can withstand the forces during the quick contraction process.

Furthermore, the N-termini of VipA homologues in *P. aeruginosa* and *S. marcescens* are specifically adapted to interact with the non-essential TagJ protein [Lossi et al., 2012, Forster et al., 2014]. Recently, ClpV of the *P. aeruginosa* H1-T6S system has been shown to interact with TagJ homologue HsiE1 and also with the corresponding VipB homologue in a manner which does not involve the ClpV-N Terminus [Forster et al., 2014]. According to the proposed secondary structure model and the Nanogold labeling experiments, the VipA N-termini are accessible at tubule ends in the contracted form, VipA might therefore also act as a recruitment platform for ClpV in some T6S systems which have evolved an alternative disassembly mode independent of the N-terminus of VipB [Forster et al., 2014]. Finally, interaction with Hcp in

the elongated states suggests also a role in T6S complex assembly and in propelling the needle forward during contraction [Lin et al., 2013, Brunet et al., 2014, Zoued et al., 2014]. This is also consistent with the secondary structure model of the VipA/B protomer and the modeled elongated state of the VipA/B tubule, as here, the inner wall of the elongated VipA/B tubule is also formed by the N-terminal region of VipA.

As described before, there are indications that the N-terminal region of VipA is also involved in the contraction process and the ejection of the needle. Assuming that these mechanisms are indeed conserved in contractile bacteriophages, this suggests that even though there are no structural similarities to known viral structures, parts of VipA might at least be remotely structurally related to proteins in other phage-like systems. Apart from the T6S system and contractile bacteriophages, there is a variety of other phage tail-like structures such as the *Pseudomonas aeruginosa* R-type pyocins [Michel-Briand and Baysse, 2002], the PVC/Afp structures [Yang et al., 2006, Hurst et al., 2007, Leiman and Shneider, 2012, Rybakova et al., 2013], and the metamorphosis-associated contractile structure (MAC) of *Pseudoalteromonas luteoviolacea* [Shikuma et al., 2014]. As already shown by Aksyuk et al. [2011], *Myoviridae* tail sheath proteins, albeit having a conserved core, are modified by insertion domains. Also, considering the tail sheath proteins of related structures, this family of protein complexes demonstrates some structural plasticity. The tail sheath of R-type pyocins is formed by just one protein with around 40 kDa molecular weight [Nakayama et al., 2000, Gebhart et al., 2012] , while up to three sheath protein in the range of 40 -50 kDa are identified in PVC/Afp-like structures, and the putative MAC sheath protein has a molecular weight of 62 kDa. So far, no additional smaller sheath proteins that coexist in a contractile sheath with gp18-like proteins like in the case of VipA/B have been reported. However, there are indications that the Afp tail sheath consists of two different kinds of bigger gp18-like sheath proteins and that the three tail sheath proteins are functionally distinct [Heymann et al., 2013, Rybakova et al., 2013]. It is therefore likely that parts of VipA bound to VipB might still resemble their counterparts in other contractile systems, yet the overall structure of VipA is unique for the T6S system.

Also, VipB is distinct from other gp18-like proteins. Despite the observed structural conservations in the core regions of VipB to viral tail sheath proteins, its N-terminal domain is unique for the Type VI secretion system. Viral tail sheaths protein often present one or two protease-resistant insertion domains (PRF domains) on the outside of the tubule [Aksyuk et al., 2011], that putatively function as a protection against extracellular proteases secreted by their hosts. These PRF domains are replaced by a 4-helix bundle N-terminal domain in VipB that contains the recognition motif for the ATPase ClpV [Pietrosiuk et al., 2011]. When ClpV binds via its N-terminal domains to the VipB N-terminus and pulls on the assembly, the tractive force is directly transferred via helices HB4 and HB5 onto a large β sheet region in the core of VipB

that might serve as a scaffolding platform. Pulling on it, possibly destabilizes the whole structure, leading to a partial unfolding of VipB, and to an unhinging of a complete protomer from the tubule assembly. This would on the one hand explain the presence of intact protomers after ClpV-mediated disassembly and on the other hand it would be also more efficient as a new ready-to-fire T6S secretion system is faster available. Experiments testing the specificity of the ClpV N-terminal domain support this suggestion as only VipB is digested while VipA remains untouched when incubated with chimeras of the ClpV N-terminal domain and ClpA/P [Pietrosiuk et al., 2011]. To sum it up, VipA presumably enhances the stability of the T6S tubule while VipB provides an N-terminal domain dedicated to the recycling of the complex.

With the T6S system being the only known phage-tail like contractile machinery which acts intracellularly, it is not surprising, that it is greatly adapted towards quick recycling. Indeed, a phylogenetic analysis of the structurally homologous tail, sheath, and base plate proteins of T6S systems, phage tail-like structures, R-type pyocins and contractile bacteriophages shows that the T6S phylogenetic group is more distinct from the latter two, which are more closely related to each other [Sarris et al., 2014].

4.4 Mechanism for contraction-state specific recycling of the T6S tubule

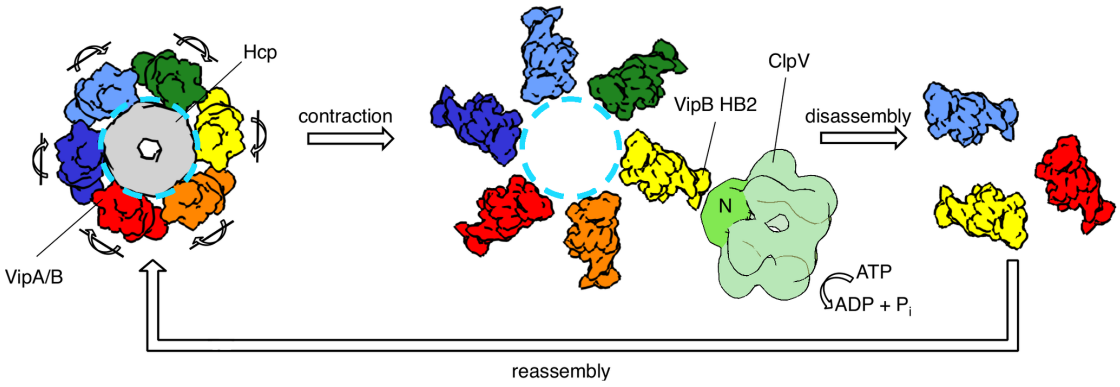

Fig. 4.2: Mechanism for T6S tubule recycling. The needle complex formed by Hcp (grey) is enclosed by the VipA/B tubule. The ClpV recognition motif in HB2 is buried in the tubule wall. Upon contraction, the VipA/B protomers swing up and outwards ejecting the needle complex. In the contracted form, the recognition motif is accessible for the ATPase ClpV and the tubule gets disassembled. Free VipA/B protomers are ready for reassembly into a loaded T6S complex. The figure is adopted from Kube et al. [2014], please see also section 6.3 Reprints.

The model of the elongated T6S tubule offers an insight into this efficient mechanism for the recycling of contracted tubules. It has been observed before, that ClpV binds specifically to the

contracted form of the VipA/B tubule [Basler and Mekalanos, 2012] and it has been suggested that this is due to a binding site at the N-terminus of VipB which is only accessible in the contracted state [Kapitein et al., 2013]. However, the exact molecular mechanism has not been known.

In contrast to the PRF domains of viral tail sheaths that are connected to the core protomer via flexible loops giving it a S-shape, the VipB N-terminal domain is rigidly connected to its core by HB4 and HB5 and VipA. Thus, the VipA/B protomer has a rather triangular shape with the ClpV recognition motif of the VipB-N-terminus located at the tip. As a consequence, even though the conserved C-terminal and middle regions are in similar positions in the elongated forms of both systems, the PRF domains are still pointing radially away from the virus tail to protect it, while the recycling domains of the T6S tubule are buried in the tubule wall. Hence, ClpV cannot access its binding motif on the elongated tubule and only contracted tubules get recycled (Fig. 4.2).

4.5 Summary and outlook

This work suggests that the contractile VipA/B tubule shares a similar architecture with other phage-like contractile structures maintained by structurally conserved VipB core regions. Thus, its conserved contraction mechanism is likely similar to bacteriophage tail sheaths. The contractile scaffold formed by structurally conserved parts is functionalized in both systems to adapt it to its individual purpose. On the one hand, viral tail sheaths are decorated with additional protease-resistant domains to protect them in the extracellular environment. On the other hand, the T6S tubule is complemented with a recycling domain on VipB and the putative chaperone VipA. Hence, the T6S tubule is adapted towards a quick recycling which is more advantageous considering its intracellular location.

Even though the structure of the VipA/B protomer is resolved up to 6 Å which allows to trace the peptide chain of VipA and VipB along discernible secondary structure elements, loops cannot be modeled reliably at this resolution and therefore have been let out. Hence, the obvious next step is a reconstruction of the tubule resolved to side chain level from a direct detector dataset and advanced processing techniques as it has been recently demonstrated for other helical structures [Wu et al., 2014]. A pseudo-atomic model of the full protomer will help to understand the exact contraction mechanism of the tubule and by analogy also of contractile bacteriophages and related complexes [Sarris et al., 2014]. However, to accomplish this, also a high-resolution structure of the elongated tubule is also needed. So far, the elongated T6S tubules could not be purified as they cannot be directly isolated from wild-type cells and VipA/B only form contracted tubules when heterologously expressed [Bönemann et al., 2009, Basler et al., 2012]. Here, a

combination of cryo-ET and helical reconstruction [Bharat et al., 2012] could be applied to get to sub-nanometer resolution which is sufficient to define conformational changes. Alternatively, the membrane complex with the T6S tubule bound to it, can be extracted and investigated by single particle methods as it has been demonstrated for the Type IV secretion system [Low et al., 2014] or the γ-secretase [Lu et al., 2014]. The contraction mechanism of the T6S tubule can also be investigated by mutating conserved residues at the interface between neighboring gp18-like C-terminal domains of VipB. Possible candidates can be drawn by analogy to TssE, which is predicted to have a very similar fold to the C-terminal domain of VipB [Lossi et al., 2011, Leiman and Shneider, 2012].

Apart from the T6S system, bacteria employ a variety of phage tail-like systems to interact with their own and other species in their environment. This makes the most likely conserved contractile machinery common to all the systems interesting for drug targeting. Alternatively, the systems are also suitable for a biotechnological use to deliver active components into cells [Sarris et al., 2014]. It is speculated, that the current problem of antibiotic resistance in many important pathogens might be circumvented by so called "anti-virulence drugs" [Clatworthy et al., 2007]. These drugs do not target the viability of the pathogen directly, but the virulence factors that are employed for infection. As a consequence, the "disarmed" pathogen can be efficiently exterminated by the immune system of the host. The T6S system is employed by bacteria to attack competitor species in their environment. For example, it confers a direct competitive advantage in the plant colonization of *A. tumefaciens* [Ma et al., 2014] and there are indications that it also plays role in gut colonization in *V. cholerae* [Fu et al., 2013]. Initial efforts have been undertaken to inhibit T6S by impairing the interaction between *V. cholerae* VipA and VipB in [Sun et al., 2014]. A future drug might strip *V. cholerae* of a functional T6S system. The pathogen can then be outcompeted by the commensal gut flora.

5 Bibliography

A A Aksyuk and M G Rossmann. Bacteriophage assembly. *Viruses*, 3(3):172–203, Mar 2011. doi: 10.3390/v3030172.

A A Aksyuk, P G Leiman, L P Kurochkina, M M Shneider, V A Kostyuchenko, V V Mesyanzhinov, and M G Rossmann. The tail sheath structure of bacteriophage T4: a molecular machine for infecting bacteria. *EMBO J*, 28(7):821–9, Apr 2009. doi: 10.1038/emboj.2009.36.

A A Aksyuk, L P Kurochkina, A Fokine, F Forouhar, V V Mesyanzhinov, L Tong, and M G Rossmann. Structural conservation of the *Myoviridae* phage tail sheath protein fold. *Structure*, 19(12):1885–94, Dec 2011. doi: 10.1016/j.str.2011.09.012.

K Amako, K Yasunaka, and K Takeya. Relationship between rhapidosome and pyocin in *Pseudomonas fluorescens*. *J Gen Microbiol*, 62(1):107–12, Jul 1970.

L A Amos and A Klug. Three-dimensional image reconstructions of the contractile tail of T4 bacteriophage. *J Mol Biol*, 99(1):51–64, Nov 1975.

P Arbeláez, B-G Han, D Typke, J Lim, R M Glaeser, and J Malik. Experimental evaluation of support vector machine-based and correlation-based approaches to automatic particle selection. *J Struct Biol*, 175(3):319–28, Sep 2011. doi: 10.1016/j.jsb.2011.05.017.

M-S Aschtgen, C S Bernard, S De Bentzmann, R Lloubes, and E Cascales. SciN is an outer membrane lipoprotein required for type VI secretion in enteroaggregative *Escherichia coli*. *Journal of bacteriology*, 190(22):7523–7531, 2008. doi: 10.1128/JB.00945-08.

M-S Aschtgen, M Gavioli, A Dessen, R Lloubes, and E Cascales. The SciZ protein anchors the enteroaggregative *Escherichia coli* Type VI secretion system to the cell wall. *Molecular microbiology*, 75(4):886–899, 2010a. doi: 10.1111/j.1365-2958.2009.07028.x.

M-S Aschtgen, M S Thomas, and E Cascales. Anchoring the type VI secretion system to the peptidoglycan: TssL, TagL, TagP... what else? *Virulence*, 1(6):535–540, 2010b.

M-S Aschtgen, A Zoued, R Lloubès, L Journet, and E Cascales. The C-tail anchored TssL subunit, an essential protein of the enteroaggregative *Escherichia coli* Sci-1 Type VI secretion system, is inserted by YidC . *Microbiologyopen*, 1(1):71–82, Mar 2012. doi: 10.1002/mbo3.9.

D F Aubert, R S Flannagan, and M A Valvano. A novel sensor kinase-response regulator hybrid controls biofilm formation and type VI secretion system activity in *Burkholderia cenocepacia*. *Infect Immun*, 76(5):1979–91, May 2008. doi: 10.1128/IAI.01338-07.

D F Aubert, D K MacDonald, and M A Valvano. BcsKC is an essential protein for the type VI secretion system activity in *Burkholderia cenocepacia* that forms an outer membrane complex with BcsLB. *J Biol Chem*, 285(46):35988–98, Nov 2010. doi: 10.1074/jbc.M110.120402.

J R Barker, A Chong, T D Wehrly, J-J Yu, S A Rodriguez, J Liu, J Celli, B P Arulanandam, and K E Klose. The *Francisella tularensis* pathogenicity island encodes a secretion system that is required for phagosome escape and virulence. *Mol Microbiol*, 74(6):1459–70, Dec 2009.

M Basler and J J Mekalanos. Type 6 secretion dynamics within and between bacterial cells. *Science*, 337(6096):815, Aug 2012. doi: 10.1126/science.1222901.

M Basler, M Pilhofer, G P Henderson, G J Jensen, and J J Mekalanos. Type VI secretion requires a dynamic contractile phage tail-like structure. *Nature*, 483(7388):182–6, Mar 2012. doi: 10.1038/nature10846.

M Basler, B T Ho, and J J Mekalanos. Tit-for-tat: type VI secretion system counterattack during bacterial cell-cell interactions. *Cell*, 152(4):884–94, Feb 2013. doi: 10.1016/j.cell.2013.01.042.

C S Bernard, Y R Brunet, M Gavioli, R Lloubès, and E Cascales. Regulation of type VI secretion gene clusters by sigma54 and cognate enhancer binding proteins and cognate enhancer binding proteins. *J Bacteriol*, 193(9):2158–67, May 2011. doi: 10.1128/JB.00029-11.

T A M Bharat, N E Davey, P Ulbrich, J D Riches, A de Marco, M Rumlova, C Sachse, T Ruml, and J A G Briggs. Structure of the immature retroviral capsid at 8 Å resolution by cryo-electron microscopy. *Nature*, 487(7407):385–9, Jul 2012. doi: 10.1038/nature11169.

L E Bingle, C M Bailey, and M J Pallen. Type VI secretion: a beginner's guide. *Curr Opin Microbiol*, 11(1):3–8, Feb 2008. doi: 10.1016/j.mib.2008.01.006.

N M C Bleumink-Pluym, L B van Alphen, Li I Bouwman, M M S M Wösten, and J P M van Putten. Identification of a functional type VI secretion system in *Campylobacter jejuni* conferring capsule polysaccharide sensitive cytotoxicity. *PLoS Pathog*, 9(5):e1003393, 2013. doi: 10.1371/journal.ppat.1003393.

G Bönemann, A Pietrosiuk, A Diemand, H Zentgraf, and A Mogk. Remodelling of VipA/VipB tubules by ClpV-mediated threading is crucial for type VI protein secretion. *EMBO J*, 28(4): 315–25, Feb 2009. doi: 10.1038/emboj.2008.269.

G Bönemann, A Pietrosiuk, and A Mogk. Tubules and donuts: a type VI secretion story. *Mol Microbiol*, 76(4):815–21, May 2010. doi: 10.1111/j.1365-2958.2010.07171.x.

F Boyer, G Fichant, J Berthod, Y Vandenbrouck, and I Attree. Dissecting the bacterial type VI secretion system by a genome wide in silico analysis: what can be learned from available microbial genomic resources? *BMC Genomics*, 10:104, 2009. doi: 10.1186/1471-2164-10-104.

J E Bröms, M Lavander, and A Sjöstedt. A conserved alpha-helix essential for a type VI secretion-like system of *Francisella tularensis*. *J Bacteriol*, 191(8):2431–46, Apr 2009. doi: 10.1128/JB.01759-08.

J E Bröms, A Sjöstedt, and M Lavander. The Role of the *Francisella tularensis* Pathogenicity Island in Type VI Secretion, Intracellular Survival, and Modulation of Host Cell Signaling. *Front Microbiol*, 1:136, 2010. doi: 10.3389/fmicb.2010.00136.

J E Bröms, L Meyer, M Lavander, P Larsson, and A Sjöstedt. DotU and VgrG, core components of type VI secretion systems, are essential for *Francisella* LVS pathogenicity. *PLoS One*, 7 (4):e34639, 2012. doi: 10.1371/journal.pone.0034639.

J E Bröms, T Ishikawa, S N Wai, and A Sjöstedt. A functional VipA-VipB interaction is required for the type VI secretion system activity of *Vibrio cholerae* O1 strain A1552. *BMC Microbiol*, 13:96, 2013. doi: 10.1186/1471-2180-13-96.

T M Brooks, D Unterweger, V Bachmann, B Kostiuk, and S Pukatzki. Lytic activity of the *Vibrio cholerae* type VI secretion toxin VgrG-3 is inhibited by the antitoxin TsaB. *J Biol Chem*, 288(11):7618–25, Mar 2013. doi: 10.1074/jbc.M112.436725.

Y R Brunet, C S Bernard, M Gavioli, R Lloubès, and E Cascales. An epigenetic switch involving overlapping fur and DNA methylation optimizes expression of a type VI secretion gene cluster. *PLoS Genet*, 7(7):e1002205, Jul 2011. doi: 10.1371/journal.pgen.1002205.

Y R Brunet, L Espinosa, S Harchouni, T Mignot, and E Cascales. Imaging type VI secretion-mediated bacterial killing. *Cell Rep*, 3(1):36–41, Jan 2013. doi: 10.1016/j.celrep.2012.11.027.

Y R Brunet, J Hénin, H Celia, and E Cascales. Type VI secretion and bacteriophage tail tubes share a common assembly pathway. *EMBO Rep*, 15(3):315–21, Mar 2014. doi: 10.1002/embr.201337936.

D W A Buchan, F Minneci, T C O Nugent, K Bryson, and D T Jones. Scalable web services for the PSIPRED Protein Analysis Workbench. *Nucleic Acids Res*, 41(Web Server issue): W349–57, Jul 2013. doi: 10.1093/nar/gkt381.

B J Burkinshaw and N C J Strynadka. Assembly and structure of the T3SS. *Biochim Biophys Acta*, 1843(8):1649–63, Aug 2014. doi: 10.1016/j.bbamcr.2014.01.035.

W N Burnette. "Western blotting": electrophoretic transfer of proteins from sodium dodecyl sulfate–polyacrylamide gels to unmodified nitrocellulose and radiographic detection with antibody and radioiodinated protein A. *Anal Biochem*, 112(2):195–203, Apr 1981.

J N Busby, S Panjikar, M J Landsberg, M R H Hurst, and J S Lott. The BC component of ABC toxins is an RHS-repeat-containing protein encapsulation device. *Nature*, 501(7468):547–50, Sep 2013. doi: 10.1038/nature12465.

M Bush and R Dixon. The role of bacterial enhancer binding proteins as specialized activators of sigma54-dependent transcription. *Microbiol Mol Biol Rev*, 76(3):497–529, Sep 2012. doi: 10.1128/MMBR.00006-12.

M G Casabona, J M Silverman, K M Sall, F Boyer, Y Couté, J Poirel, D Grunwald, J D Mougous, S Elsen, and I Attree. An ABC transporter and an outer membrane lipoprotein participate in posttranslational activation of type VI secretion in *Pseudomonas aeruginosa*. *Environ Microbiol*, 15(2):471–86, Feb 2013. doi: 10.1111/j.1462-2920.2012.02816.x.

S Chakraborty, M Li, C Chatterjee, J Sivaraman, K Y Leung, and Y-K Mok. Temperature and Mg2+ sensing by a novel PhoP-PhoQ two-component system for regulation of virulence in *Edwardsiella tarda*. *J Biol Chem*, 285(50):38876–88, Dec 2010. doi: 10.1074/jbc.M110.179150.

Y-W Chang, S Chen, E I Tocheva, A Treuner-Lange, S Löbach, L Søgaard-Andersen, and G J Jensen. Correlated cryogenic photoactivated localization microscopy and cryo-electron tomography. *Nat Methods*, 11(7):737–9, Jul 2014. doi: 10.1038/nmeth.2961.

P J Christie, N Whitaker, and C González-Rivera. Mechanism and structure of the bacterial type IV secretion systems. *Biochim Biophys Acta*, 1843(8):1578–91, Aug 2014. doi: 10.1016/j.bbamcr.2013.12.019.

D K Clare and E V Orlova. 4.6 Å Cryo-EM reconstruction of tobacco mosaic virus from images recorded at 300 keV on a 4k x 4k CCD camera. *J Struct Biol*, 171(3):303–8, Sep 2010. doi: 10.1016/j.jsb.2010.06.011.

A E Clatworthy, E Pierson, and D T Hung. Targeting virulence: a new paradigm for antimicrobial therapy. *Nat Chem Biol*, 3(9):541–8, Sep 2007. doi: 10.1038/nchembio.2007.24.

C Cole, J D Barber, and G J Barton. The Jpred 3 secondary structure prediction server. *Nucleic Acids Res*, 36(Web Server issue):W197–201, Jul 2008. doi: 10.1093/nar/gkn238.

S J Coulthurst. The Type VI secretion system - a widespread and versatile cell targeting system. *Research in microbiology*, 164(6):640–654, 2013. doi: 10.1016/j.resmic.2013.03.017.

S Das and K Chaudhuri. Identification of a unique IAHP (IcmF associated homologous proteins) cluster in *Vibrio cholerae* and other proteobacteria through in silico analysis. *In Silico Biol*, 3 (3):287–300, 2003.

A R Davidson, L Cardarelli, L G Pell, D R Radford, and K L Maxwell. Long noncontractile tail machines of bacteriophages. *Adv Exp Med Biol*, 726:115–42, 2012.

O M de Bruin, B N Duplantis, J S Ludu, R F Hare, E B Nix, C L Schmerk, C S Robb, A B Boraston, K Hueffer, and F E Nano. The biochemical properties of the *Francisella* pathogenicity island (FPI)-encoded proteins IglA, IglB, IglC, PdpB and DotU suggest roles in type VI secretion. *Microbiology*, 157(Pt 12):3483–91, Dec 2011. doi: 10.1099/mic.0.052308-0.

R Diaz, W J Rice, and D L Stokes. Fourier-Bessel reconstruction of helical assemblies. *Methods Enzymol*, 482:131–65, 2010. doi: 10.1016/S0076-6879(10)82005-1.

T G Dong and J J Mekalanos. Characterization of the RpoN regulon reveals differential regulation of T6SS and new flagellar operons in *Vibrio cholerae* O37 strain V52. *Nucleic Acids Res*, 40(16):7766–75, Sep 2012. doi: 10.1093/nar/gks567.

T G Dong, B T Ho, Dh R Yoder-Himes, and J J Mekalanos. Identification of T6SS-dependent effector and immunity proteins by Tn-seq in *Vibrio cholerae*. *Proc Natl Acad Sci U S A*, 110 (7):2623–8, Feb 2013. doi: 10.1073/pnas.1222783110.

B Douzi, S Spinelli, S Blangy, A Roussel, E Durand, Y R Brunet, E Cascales, and C Cambillau. Crystal structure and self-interaction of the type VI secretion tail-tube protein from enteroaggregative *Escherichia coli*. *PLoS One*, 9(2):e86918, 2014. doi: 10.1371/journal.pone.0086918.

E Durand, E Derrez, G Audoly, S Spinelli, M Ortiz-Lombardia, D Raoult, E Cascales, and C Cambillau. Crystal structure of the VgrG1 actin cross-linking domain of the *Vibrio cholerae* type VI secretion system. *J Biol Chem*, 287(45):38190–9, Nov 2012a. doi: 10.1074/jbc.M112.390153.

E Durand, A Zoued, S Spinelli, P J H Watson, M-S Aschtgen, L Journet, C Cambillau, and E Cascales. Structural characterization and oligomerization of the TssL protein, a component shared by bacterial type VI and type IVb secretion systems. *J Biol Chem*, 287(17):14157–68, Apr 2012b. doi: 10.1074/jbc.M111.338731.

E Durand, C Cambillau, E Cascales, and L Journet. VgrG, Tae, Tle, and beyond: the versatile arsenal of Type VI secretion effectors. *Trends Microbiol*, 22(9):498–507, Sep 2014. doi: 10.1016/j.tim.2014.06.004.

G Effantin, R Hamasaki, T Kawasaki, M Bacia, C Moriscot, W Weissenhorn, T Yamada, and G Schoehn. Cryo-electron microscopy three-dimensional structure of the jumbo phage phiRSL1 infecting the phytopathogen *Ralstonia solanacearum*. *Structure*, 21(2):298–305, Feb 2013. doi: 10.1016/j.str.2012.12.017.

E H Egelman. Single-particle reconstruction from EM images of helical filaments. *Curr Opin Struct Biol*, 17(5):556–61, Oct 2007a. doi: 10.1016/j.sbi.2007.07.006.

E H Egelman. The iterative helical real space reconstruction method: surmounting the problems posed by real polymers. *J Struct Biol*, 157(1):83–94, Jan 2007b. doi: 10.1016/j.jsb.2006.05.015.

N Eswar, B Webb, Marc A Marti-Renom, M S Madhusudhan, MY Eramian, Dand Shen, U Pieper, and A Sali. Comparative protein structure modeling using MODELLER. *Curr Protoc Protein Sci*, Chapter 2:Unit 2.9, Nov 2007. doi: 10.1002/0471140864.ps0209s50.

C Felisberto-Rodrigues, E Durand, M-S Aschtgen, S Blangy, M Ortiz-Lombardia, B Douzi, C Cambillau, and E Cascales. Towards a structural comprehension of bacterial type VI secretion systems: characterization of the TssJ-TssM complex of an *Escherichia coli* pathovar. *PLoS Pathog*, 7(11):e1002386, Nov 2011. doi: 10.1371/journal.ppat.1002386.

A Fokine, Z Zhang, S Kanamaru, V D Bowman, A A Aksyuk, F Arisaka, V B Rao, and M G Rossmann. The molecular architecture of the bacteriophage T4 neck. *J Mol Biol*, 425(10):1731–44, May 2013. doi: 10.1016/j.jmb.2013.02.012.

A Forster, S Planamente, E Manoli, N S Lossi, P S Freemont, and A Filloux. Coevolution of the ATPase ClpV, the Sheath Proteins TssB and TssC and the Accessory Protein TagJ/HsiE1 Distinguishes Type VI Secretion Classes. *J Biol Chem*, Oct 2014. doi: 10.1074/jbc.M114.600510.

J Frank, M Radermacher, P Penczek, J Zhu, Y Li, M Ladjadj, and A Leith. SPIDER and WEB: processing and visualization of images in 3D electron microscopy and related fields. *J Struct Biol*, 116(1):190–9, 1996. doi: 10.1006/jsbi.1996.0030.

M J Fritsch, K Trunk, J A Diniz, M Guo, Matthias Trost, and S J Coulthurst. Proteomic identification of novel secreted antibacterial toxins of the *Serratia marcescens* type VI secretion system. *Mol Cell Proteomics*, 12(10):2735–49, Oct 2013. doi: 10.1074/mcp.M113.030502.

Y Fu, M K Waldor, and J J Mekalanos. Tn-Seq analysis of *Vibrio cholerae* intestinal colonization reveals a role for T6SS-mediated antibacterial activity in the host. *Cell Host Microbe*, 14(6): 652–63, Dec 2013. doi: 10.1016/j.chom.2013.11.001.

D Gebhart, S R Williams, K A Bishop-Lilly, G R Govoni, K M Willner, A Butani, S Sozhamannan, D Martin, L-C Fortier, and D Scholl. Novel high-molecular-weight, R-type bacteriocins of *Clostridium difficile*. *J Bacteriol*, 194(22):6240–7, Nov 2012. doi: 10.1128/JB.01272-12.

A L Goodman, B Kulasekara, A Rietsch, D Boyd, R S Smith, and S Lory. A signaling network reciprocally regulates genes associated with acute infection and chronic persistence in *Pseudomonas aeruginosa*. *Dev Cell*, 7(5):745–54, Nov 2004. doi: 10.1016/j.devcel.2004.08.020.

A L Goodman, M Merighi, M Hyodo, I Ventre, A Filloux, and S Lory. Direct interaction between sensor kinase proteins mediates acute and chronic disease phenotypes in a bacterial pathogen. *Genes Dev*, 23(2):249–59, Jan 2009. doi: 10.1101/gad.1739009.

S G Grant, J Jessee, F R Bloom, and D Hanahan. Differential plasmid rescue from transgenic mouse DNAs into *Escherichia coli* methylation-restriction mutants. *Proc Natl Acad Sci U S A*, 87(12):4645–9, Jun 1990.

D Hanahan. Studies on transformation of *Escherichia coli* with plasmids. *J Mol Biol*, 166(4): 557–80, Jun 1983.

R Henderson, A Sali, M L Baker, B Carragher, B Devkota, K H Downing, E H Egelman, Z Feng, J Frank, N Grigorieff, W Jiang, S J Ludtke, O Medalia, P A Penczek, P B Rosenthal, M G Rossmann, M F Schmid, G F Schröder, A C Steven, D L Stokes, J D Westbrook, W Wriggers, H Yang, J Young, H M Berman, W Chiu, G J Kleywegt, and C L Lawson. Outcome of the first electron microscopy validation task force meeting. *Structure*, 20(2):205–14, Feb 2012. doi: 10.1016/j.str.2011.12.014.

F Herzog, A Kahraman, D Boehringer, R Mak, A Bracher, T Walzthoeni, A Leitner, M Beck, F-U Hartl, N Ban, L Malmström, and R Aebersold. Structural probing of a protein phosphatase

2A network by chemical cross-linking and mass spectrometry. *Science*, 337(6100):1348–52, Sep 2012. doi: 10.1126/science.1221483.

J B Heymann, J D Bartho, D Rybakova, H P Venugopal, D C Winkler, A Sen, M R H Hurst, and A K Mitra. Three-dimensional structure of the toxin-delivery particle antifeeding prophage of *Serratia entomophila*. *J Biol Chem*, 288(35):25276–84, Aug 2013. doi: 10.1074/jbc.M113.456145.

B T Ho, M Basler, and J J Mekalanos. Type 6 secretion system-mediated immunity to type 4 secretion system-mediated gene transfer. *Science*, 342(6155):250–3, Oct 2013. doi: 10.1126/science.1243745.

B T Ho, T G Dong, and J J Mekalanos. A view to a kill: the bacterial type VI secretion system. *Cell Host Microbe*, 15(1):9–21, Jan 2014. doi: 10.1016/j.chom.2013.11.008.

R D Hood, P Singh, F Hsu, T Güvener, M A Carl, R R S Trinidad, J M Silverman, B B Ohlson, K G Hicks, R L Plemel, M Li, S Schwarz, W Y Wang, A J Merz, D R Goodlett, and J D Mougous. A type VI secretion system of *Pseudomonas aeruginosa* targets a toxin to bacteria. *Cell Host Microbe*, 7(1):25–37, Jan 2010. doi: 10.1016/j.chom.2009.12.007.

E N G Houben, K V Korotkov, and W Bitter. Take five - Type VII secretion systems of Mycobacteria. *Biochim Biophys Acta*, 1843(8):1707–16, Aug 2014. doi: 10.1016/j.bbamcr.2013.11.003.

F Hsu, S Schwarz, and J D Mougous. TagR promotes PpkA-catalysed type VI secretion activation in *Pseudomonas aeruginosa*. *Mol Microbiol*, 72(5):1111–25, Jun 2009. doi: 10.1111/j.1365-2958.2009.06701.x.

M R H Hurst, T R Glare, and T A Jackson. Cloning *Serratia entomophila* antifeeding genes–a putative defective prophage active against the grass grub *Costelytra zealandica*. *J Bacteriol*, 186(15):5116–28, Aug 2004. doi: 10.1128/JB.186.15.5116-5128.2004.

M R H Hurst, S S Beard, T A Jackson, and S M Jones. Isolation and characterization of the *Serratia entomophila* antifeeding prophage. *FEMS Microbiol Lett*, 270(1):42–8, May 2007. doi: 10.1111/j.1574-6968.2007.00645.x.

S I Ishii, Y Nishi, and F Egami. The fine structure of a pyocin. *J Mol Biol*, 13(2):428–31, Sep 1965.

T Ishikawa, P K Rompikuntal, B Lindmark, D L Milton, and S N Wai. Quorum sensing regulation of the two hcp alleles in *Vibrio cholerae* O1 strains. *PLoS One*, 4(8):e6734, 2009. doi: 10.1371/journal.pone.0006734.

T Ishikawa, D Sabharwal, J Bröms, D L Milton, A Sjöstedt, B E Uhlin, and S N Wai. Pathoadaptive conditional regulation of the type VI secretion system in *Vibrio cholerae* O1 strains. *Infect Immun*, 80(2):575–84, Feb 2012. doi: 10.1128/IAI.05510-11.

F Jiang, N R Waterfield, J Yang, G Yang, and Q Jin. A *Pseudomonas aeruginosa* type VI secretion phospholipase D effector targets both prokaryotic and eukaryotic cells. *Cell Host Microbe*, 15(5):600–10, May 2014. doi: 10.1016/j.chom.2014.04.010.

C Jobichen, S Chakraborty, M Li, J Zheng, L Joseph, Y K Mok, K Y Leung, and J Sivaraman. Structural basis for the secretion of EvpC: a key type VI secretion system protein from *Edwardsiella tarda*. *PloS one*, 5(9):e12910, 2010. doi: 10.1371/journal.pone.0012910.

N Kapitein and A Mogk. Type VI secretion system helps find a niche. *Cell Host Microbe*, 16 (1):5–6, Jul 2014. doi: 10.1016/j.chom.2014.06.012.

N Kapitein, G Bönemann, A Pietrosiuk, F Seyffer, I Hausser, J K Locker, and A Mogk. ClpV recycles VipA/VipB tubules and prevents non-productive tubule formation to ensure efficient type VI protein secretion. *Mol Microbiol*, 87(5):1013–28, Mar 2013. doi: 10.1111/mmi.12147.

B Kastner, N Fischer, M M Golas, B Sander, P Dube, D Boehringer, K Hartmuth, J Deckert, F Hauer, E Wolf, H Uchtenhagen, H Urlaub, F Herzog, J M Peters, D Poerschke, R Lührmann, and H Stark. GraFix: sample preparation for single-particle electron cryomicroscopy. *Nat Methods*, 5(1):53–5, Jan 2008. doi: 10.1038/nmeth1139.

E Kellenberger and E B De la Tour. On the fine structure of normal and "polymerized" tail sheath of phage T4. *J Ultrastruct Res*, 11:545–63, Dec 1964. doi: 10.1016/S0022-5320(64)80081-2.

M Kitaoka, S T Miyata, T M Brooks, D Unterweger, and S Pukatzki. VasH is a transcriptional regulator of the type VI secretion system functional in endemic and pandemic *Vibrio cholerae*. *J Bacteriol*, 193(23):6471–82, Dec 2011. doi: 10.1128/JB.05414-11.

S Koskiniemi, J G Lamoureux, K C Nikolakakis, C t'Kint de Roodenbeke, M D Kaplan, D A Low, and C S Hayes. Rhs proteins from diverse bacteria mediate intercellular competition. *Proc Natl Acad Sci U S A*, 110(17):7032–7, Apr 2013. doi: 10.1073/pnas.1300627110.

V A Kostyuchenko, P R Chipman, P G Leiman, F Arisaka, V V Mesyanzhinov, and M G Rossmann. The tail structure of bacteriophage T4 and its mechanism of contraction. *Nat Struct Mol Biol*, 12(9):810–3, Sep 2005. doi: 10.1038/nsmb975.

S Kube, N Kapitein, T Zimniak, F Herzog, A Mogk, and P Wendler. Structure of the VipA/B type VI secretion complex suggests a contraction-state-specific recycling mechanism. *Cell Rep*, 8(1):20–30, Jul 2014. doi: 10.1016/j.celrep.2014.05.034.

A Kucukelbir, F J Sigworth, and H D Tagare. Quantifying the local resolution of cryo-EM density maps. *Nat Methods*, 11(1):63–5, Jan 2014. doi: 10.1038/nmeth.2727.

U K Laemmli. Cleavage of structural proteins during the assembly of the head of bacteriophage T4. *Nature*, 227(5259):680–5, Aug 1970.

G C Lander, H R Saibil, and E Nogales. Go hybrid: EM, crystallography, and beyond. *Curr Opin Struct Biol*, 22(5):627–35, Oct 2012. doi: 10.1016/j.sbi.2012.07.006.

K Lapouge, M Schubert, F H-T Allain, and D Haas. Gac/Rsm signal transduction pathway of gamma-proteobacteria: from RNA recognition to regulation of social behaviour. *Mol Microbiol*, 67(2):241–53, Jan 2008. doi: 10.1111/j.1365-2958.2007.06042.x.

P G Leiman and M M Shneider. Contractile tail machines of bacteriophages. *Adv Exp Med Biol*, 726:93–114, 2012. doi: 10.1007/978-1-4614-0980-9_5.

P G Leiman, P R Chipman, V A Kostyuchenko, V V Mesyanzhinov, and M G Rossmann. Three-dimensional rearrangement of proteins in the tail of bacteriophage T4 on infection of its host. *Cell*, 118(4):419–29, Aug 2004. doi: 10.1016/j.cell.2004.07.022.

P G Leiman, M Basler, U A Ramagopal, J B Bonanno, J M Sauder, S Pukatzki, S K Burley, S C Almo, and J J Mekalanos. Type VI secretion apparatus and phage tail-associated protein complexes share a common evolutionary origin. *Proc Natl Acad Sci U S A*, 106(11):4154–9, Mar 2009. doi: 10.1073/pnas.0813360106.

P G Leiman, F Arisaka, M J van Raaij, V A Kostyuchenko, A A Aksyuk, S Kanamaru, and M G Rossmann. Morphogenesis of the T4 tail and tail fibers. *Virol J*, 7:355, 2010. doi: 10.1186/1743-422X-7-355.

K Lertpiriyapong, E R Gamazon, Y Feng, D S Park, J Pang, G Botka, M E Graffam, Z Ge, and J G Fox. *Campylobacter jejuni* type VI secretion system: roles in adaptation to deoxycholic acid, host cell adherence, invasion, and in vivo colonization. *PLoS One*, 7(8):e42842, 2012. doi: 10.1371/journal.pone.0042842.

R A Lewin. Rod-shaped Particles in *Saprospira*. *Nature*, 198(4875):103–104, 04 1963. doi: 10.1038/198103b0.

J-S Lin, L-S Ma, and E-M Lai. Systematic dissection of the agrobacterium type VI secretion system reveals machinery and secreted components for subcomplex formation. *PLoS One*, 8 (7):e67647, 2013. doi: 10.1371/journal.pone.0067647.

J-S Lin, H-H Wu, P-H Hsu, L-S Ma, Y-Y Pang, M-D Tsai, and E-M Lai. Fha interaction with phosphothreonine of TssL activates type VI secretion in *Agrobacterium tumefaciens*. *PLoS Pathog*, 10(3):e1003991, Mar 2014. doi: 10.1371/journal.ppat.1003991.

N S Lossi, R Dajani, P Freemont, and A Filloux. Structure-function analysis of HsiF, a gp25-like component of the type VI secretion system, in *Pseudomonas aeruginosa*. *Microbiology*, 157 (Pt 12):3292–305, Dec 2011. doi: 10.1099/mic.0.051987-0.

N S Lossi, E Manoli, P Simpson, C Jones, K Hui, R Dajani, S J Coulthurst, P Freemont, and A Filloux. The archetype *Pseudomonas aeruginosa* proteins TssB and TagJ form a novel subcomplex in the bacterial type VI secretion system. *Mol Microbiol*, 86(2):437–56, Oct 2012. doi: 10.1111/j.1365-2958.2012.08204.x.

N S Lossi, E Manoli, A Förster, R Dajani, T Pape, P Freemont, and A Filloux. The HsiB1C1 (TssB-TssC) complex of the *Pseudomonas aeruginosa* type VI secretion system forms a bacteriophage tail sheath-like structure. *J Biol Chem*, 288(11):7536–48, Mar 2013. doi: 10.1074/jbc.M112.439273.

H H Low, F Gubellini, A Rivera-Calzada, N Braun, S Connery, A Dujeancourt, F Lu, A Redzej, R Fronzes, E V Orlova, and G Waksman. Structure of a type IV secretion system. *Nature*, 508(7497):550–3, Apr 2014. doi: 10.1038/nature13081.

P Lu, X-C Bai, D Ma, T Xie, C Yan, L Sun, G Yang, Y Zhao, R Zhou, S H W Scheres, and Y Shi. Three-dimensional structure of human gamma-secretase. *Nature*, 512(7513):166–70, Aug 2014. doi: 10.1038/nature13567.

S J Ludtke, P R Baldwin, and W Chiu. EMAN: semiautomated software for high-resolution single-particle reconstructions. *J Struct Biol*, 128(1):82–97, Dec 1999. doi: 10.1006/jsbi.1999.4174.

A T Ma and J J Mekalanos. *In vivo* actin cross-linking induced by *Vibrio cholerae* type VI secretion system is associated with intestinal inflammation. *Proc Natl Acad Sci U S A*, 107 (9):4365–70, Mar 2010. doi: 10.1073/pnas.0915156107.

A T Ma, S McAuley, S Pukatzki, and J J Mekalanos. Translocation of a *Vibrio cholerae* type VI secretion effector requires bacterial endocytosis by host cells. *Cell Host Microbe*, 5(3): 234–43, Mar 2009a. doi: 10.1016/j.chom.2009.02.005.

L-S Ma, J-S Lin, and E-M Lai. An IcmF family protein, ImpLM, is an integral inner membrane protein interacting with ImpKL, and its walker a motif is required for type VI secretion system-mediated Hcp secretion in *Agrobacterium tumefaciens*. *J Bacteriol*, 191(13):4316–29, Jul 2009b. doi: 10.1128/JB.00029-09.

L-S Ma, F Narberhaus, and E-M Lai. IcmF family protein TssM exhibits ATPase activity and energizes type VI secretion. *J Biol Chem*, 287(19):15610–21, May 2012. doi: 10.1074/jbc.M111.301630.

L-S Ma, A Hachani, J-S Lin, A Filloux, and E-M Lai. *Agrobacterium tumefaciens* deploys a superfamily of type VI secretion DNase effectors as weapons for interbacterial competition *in planta*. *Cell Host Microbe*, 16(1):94–104, Jul 2014. doi: 10.1016/j.chom.2014.06.002.

H Matsui, Y Sano, H Ishihara, and T Shinomiya. Regulation of pyocin genes in *Pseudomonas aeruginosa* by positive (prtN) and negative (prtR) regulatory genes. *J Bacteriol*, 175(5):1257–63, Mar 1993.

Y Michel-Briand and C Baysse. The pyocins of *Pseudomonas aeruginosa*. *Biochimie*, 84(5-6):499–510, 2002.

J A Mindell and N Grigorieff. Accurate determination of local defocus and specimen tilt in electron microscopy. *J Struct Biol*, 142(3):334–47, Jun 2003.

S T Miyata, M Kitaoka, T M Brooks, S B McAuley, and S Pukatzki. *Vibrio cholerae* requires the type VI secretion system virulence factor VasX to kill *Dictyostelium discoideum*. *Infect Immun*, 79(7):2941–9, Jul 2011. doi: 10.1128/IAI.01266-10.

S T Miyata, V Bachmann, and S Pukatzki. Type VI secretion system regulation as a consequence of evolutionary pressure. *J Med Microbiol*, 62(Pt 5):663–76, May 2013a. doi: 10.1099/jmm.0.053983-0.

S T Miyata, D Unterweger, S P Rudko, and S Pukatzki. Dual expression profile of type VI secretion system immunity genes protects pandemic *Vibrio cholerae*. *PLoS Pathog*, 9(12):e1003752, 2013b. doi: 10.1371/journal.ppat.1003752.

M F Moody. Structure of the sheath of bacteriophage T4. I. Structure of the contracted sheath and polysheath. *J Mol Biol*, 25(2):167–200, Apr 1967.

J D Mougous, M E Cuff, S Raunser, A Shen, M Zhou, C A Gifford, A L Goodman, G Joachimiak, C L Ordoñez, S Lory, T Walz, A Joachimiak, and J J Mekalanos. A virulence locus of *Pseudomonas aeruginosa* encodes a protein secretion apparatus. *Science*, 312(5779):1526–30, Jun 2006. doi: 10.1126/science.1128393.

J D Mougous, C A Gifford, T L Ramsdell, and J J Mekalanos. Threonine phosphorylation post-translationally regulates protein secretion in *Pseudomonas aeruginosa*. *Nat Cell Biol*, 9(7): 797–803, Jul 2007. doi: 10.1038/ncb1605.

K Nakayama, K Takashima, H Ishihara, T Shinomiya, M Kageyama, S Kanaya, M Ohnishi, T Murata, H Mori, and T Hayashi. The R-type pyocin of *Pseudomonas aeruginosa* is related to P2 phage, and the F-type is related to lambda phage. *Mol Microbiol*, 38(2):213–31, Oct 2000. doi: 10.1046/j.1365-2958.2000.02135.x.

M Nivaskumar and O Francetic. Type II secretion system: a magic beanstalk or a protein escalator. *Biochim Biophys Acta*, 1843(8):1568–77, Aug 2014. doi: 10.1016/j.bbamcr.2013.12.020.

K N Parent, R S Sinkovits, M M Suhanovsky, C M Teschke, E H Egelman, and T S Baker. Cryo-reconstructions of P22 polyheads suggest that phage assembly is nucleated by trimeric interactions among coat proteins. *Phys Biol*, 7(4):045004, 2010. doi: 10.1088/1478-3975/7/4/045004.

M Pazirandeh and J R Campbell. Protein composition of rhapidosomes isolated from *Aquaspirillum itersonii*. *J Gen Microbiol*, 139(4):859–64, Apr 1993.

L G Pell, V Kanelis, L W Donaldson, P L Howell, and A R Davidson. The phage lambda major tail protein structure reveals a common evolution for long-tailed phages and the type VI bacterial secretion system. *Proc Natl Acad Sci U S A*, 106(11):4160–5, Mar 2009. doi: 10.1073/pnas.0900044106.

J E Peters, T E Thate, and N L Craig. Definition of the *Escherichia coli* MC4100 genome by use of a DNA array. *J Bacteriol*, 185(6):2017–21, Mar 2003.

E F Pettersen, T D Goddard, C C Huang, G S Couch, D M Greenblatt, E C Meng, and T E Ferrin. UCSF Chimera–a visualization system for exploratory research and analysis. *J Comput Chem*, 25(13):1605–12, Oct 2004. doi: 10.1002/jcc.20084.

R Pieper, S-T Huang, J M Robinson, D J Clark, H Alami, P P Parmar, R D Perry, R D Fleischmann, and S N Peterson. Temperature and growth phase influence the outer-membrane proteome and the expression of a type VI secretion system in *Yersinia pestis*. *Microbiology*, 155(Pt 2):498–512, Feb 2009. doi: 10.1099/mic.0.022160-0.

A Pietrosiuk, E D Lenherr, S Falk, G Bönemann, J Kopp, H Zentgraf, I Sinning, and A Mogk. Molecular basis for the unique role of the AAA+ chaperone ClpV in type VI protein secretion. *J Biol Chem*, 286(34):30010–21, Aug 2011. doi: 10.1074/jbc.M111.253377.

G D Pintilie, J Zhang, T D Goddard, W Chiu, and D C Gossard. Quantitative analysis of cryo-EM density map segmentation by watershed and scale-space filtering, and fitting of structures by alignment to regions. *J Struct Biol*, 170(3):427–38, Jun 2010. doi: 10.1016/j.jsb.2010.03.007.

A Puhar and P J Sansonetti. Type III secretion system. *Curr Biol*, 24(17):R784–91, Sep 2014. doi: 10.1016/j.cub.2014.07.016.

S Pukatzki, A T Ma, D Sturtevant, B Krastins, D Sarracino, W C Nelson, J F Heidelberg, and J J Mekalanos. Identification of a conserved bacterial protein secretion system in *Vibrio cholerae* using the *Dictyostelium* host model system. *Proc Natl Acad Sci U S A*, 103(5):1528–33, Jan 2006. doi: 10.1073/pnas.0510322103.

S Pukatzki, A T Ma, A T Revel, D Sturtevant, and J J Mekalanos. Type VI secretion system translocates a phage tail spike-like protein into target cells where it cross-links actin. *Proc Natl Acad Sci U S A*, 104(39):15508–13, Sep 2007. doi: 10.1073/pnas.0706532104.

S Pukatzki, S B McAuley, and S T Miyata. The type VI secretion system: translocation of effectors and effector-domains. *Curr Opin Microbiol*, 12(1):11–7, Feb 2009. doi: 10.1016/j.mib.2008.11.010.

V A Rao, S M Shepherd, G English, S J Coulthurst, and W N Hunter. The structure of *Serratia marcescens* Lip, a membrane-bound component of the type VI secretion system. *Acta Crystallogr D Biol Crystallogr*, 67(Pt 12):1065–72, Dec 2011. doi: 10.1107/S0907444911046300.

C S Robb, F E Nano, and A B Boraston. The structure of the conserved type six secretion protein TssL (DotU) from *Francisella novicida*. *J Mol Biol*, 419(5):277–83, Jun 2012. doi: 10.1016/j.jmb.2012.04.003.

C S Robb, M Assmus, F E Nano, and A B Boraston. Structure of the T6SS lipoprotein TssJ1 from *Pseudomonas aeruginosa*. *Acta Crystallogr Sect F Struct Biol Cryst Commun*, 69(Pt 6):607–10, Jun 2013. doi: 10.1107/S1744309113012220.

A Rodou, D O Ankrah, and C Stathopoulos. Toxins and secretion systems of *Photorhabdus luminescens*. *Toxins (Basel)*, 2(6):1250–64, Jun 2010. doi: 10.3390/toxins2061250.

A M Roseman. FindEM–a fast, efficient program for automatic selection of particles from electron micrographs. *J Struct Biol*, 145(1-2):91–9, 2004.

B Rost, G Yachdav, and J Liu. The PredictProtein server. *Nucleic Acids Res*, 32(Web Server issue):W321–6, Jul 2004. doi: 10.1093/nar/gkh377.

A B Russell, R D Hood, N K Bui, M LeRoux, W Vollmer, and J D Mougous. Type VI secretion delivers bacteriolytic effectors to target cells. *Nature*, 475(7356):343–347, 2011. doi: 10.1038/nature10244.

A B Russell, P Singh, M Brittnacher, N K Bui, R D Hood, M A Carl, D M Agnello, S Schwarz, D R Goodlett, W Vollmer, and J D Mougous. A widespread bacterial type VI secretion effector superfamily identified using a heuristic approach. *Cell host & microbe*, 11(5):538–549, 2012. doi: 10.1016/j.chom.2012.04.007.

A B Russell, M LeRoux, K Hathazi, D M Agnello, T Ishikawa, P A Wiggins, S N Wai, and J D Mougous. Diverse type VI secretion phospholipases are functionally plastic antibacterial effectors. *Nature*, 496(7446):508–12, Apr 2013. doi: 10.1038/nature12074.

A B Russell, S B Peterson, and J D Mougous. Type VI secretion system effectors: poisons with a purpose. *Nat Rev Microbiol*, 12(2):137–48, Feb 2014a. doi: 10.1038/nrmicro3185.

A B Russell, A G Wexler, B N Harding, J C Whitney, A J Bohn, Y A Goo, B Q Tran, N A Barry, H Zheng, S B Peterson, S Chou, T Gonen, D R Goodlett, A L Goodman, and J D Mougous. A type VI secretion-related pathway in Bacteroidetes mediates interbacterial antagonism. *Cell Host Microbe*, 16(2):227–36, Aug 2014b. doi: 10.1016/j.chom.2014.07.007.

D Rybakova, M Radjainia, A Turner, A Sen, A K Mitra, and M R H Hurst. Role of antifeeding prophage (Afp) protein Afp16 in terminating the length of the Afp tailocin and stabilizing its sheath. *Mol Microbiol*, 89(4):702–14, Aug 2013. doi: 10.1111/mmi.12305.

D Salomon, L N Kinch, D C Trudgian, X Guo, J A Klimko, N V Grishin, H Mirzaei, and K Orth. Marker for type VI secretion system effectors. *Proc Natl Acad Sci U S A*, 111(25):9271–6, Jun 2014. doi: 10.1073/pnas.1406110111.

P F Sarris, E D Ladoukakis, N J Panopoulos, and E V Scoulica. A phage tail-derived element with wide distribution among both prokaryotic domains: a comparative genomic and phylogenetic study. *Genome Biol Evol*, 6(7):1739–47, Jul 2014. doi: 10.1093/gbe/evu136.

K J F Satchell. Bacterial martyrdom: phagocytes disabled by type VI secretion after engulfing bacteria. *Cell Host Microbe*, 5(3):213–4, Mar 2009. doi: 10.1016/j.chom.2009.03.001.

S H W Scheres. RELION: implementation of a Bayesian approach to cryo-EM structure determination. *J Struct Biol*, 180(3):519–30, Dec 2012a. doi: 10.1016/j.jsb.2012.09.006.

S H W Scheres. A Bayesian view on cryo-EM structure determination. *J Mol Biol*, 415(2):406–18, Jan 2012b. doi: 10.1016/j.jmb.2011.11.010.

S H W Scheres and S Chen. Prevention of overfitting in cryo-EM structure determination. *Nat Methods*, 9(9):853–4, Sep 2012. doi: 10.1038/nmeth.2115.

C Schlieker, H Zentgraf, P Dersch, and A Mogk. ClpV, a unique Hsp100/Clp member of pathogenic proteobacteria. *Biol Chem*, 386(11):1115–27, Nov 2005. doi: 10.1515/BC.2005.128.

C A Schneider, W S Rasband, and K W Eliceiri. NIH Image to ImageJ: 25 years of image analysis. *Nat Methods*, 9(7):671–5, Jul 2012.

D Scholl, M Cooley, S R Williams, D Gebhart, D Martin, A Bates, and R Mandrell. An engineered R-type pyocin is a highly specific and sensitive bactericidal agent for the food-borne pathogen *Escherichia coli* O157:H7. *Antimicrob Agents Chemother*, 53(7):3074–80, Jul 2009. doi: 10.1128/AAC.01660-08.

G Shalom, J G Shaw, and M S Thomas. *In vivo* expression technology identifies a type VI secretion system locus in *Burkholderia pseudomallei* that is induced upon invasion of macrophages. *Microbiology*, 153(Pt 8):2689–99, Aug 2007. doi: 10.1099/mic.0.2007/006585-0.

N J Shikuma, M Pilhofer, G L Weiss, M G Hadfield, G J Jensen, and D K Newman. Marine tubeworm metamorphosis induced by arrays of bacterial phage tail-like structures. *Science*, 343(6170):529–33, Jan 2014. doi: 10.1126/science.1246794.

M M Shneider, S A Buth, B T Ho, M Basler, J J Mekalanos, and P G Leiman. PAAR-repeat proteins sharpen and diversify the type VI secretion system spike. *Nature*, 500(7462):350–3, Aug 2013. doi: 10.1038/nature12453.

J M Silverman, L S Austin, F Hsu, K G Hicks, R D Hood, and J D Mougous. Separate inputs modulate phosphorylation-dependent and -independent type VI secretion activation. *Mol Microbiol*, 82(5):1277–90, Dec 2011. doi: 10.1111/j.1365-2958.2011.07889.x.

J M Silverman, Y R Brunet, E Cascales, and J D Mougous. Structure and regulation of the type VI secretion system. *Annu Rev Microbiol*, 66:453–72, 2012. doi: 10.1146/annurev-micro-121809-151619.

J M Silverman, D M Agnello, H Zheng, Be T Andrews, M Li, C E Catalano, T Gonen, and J D Mougous. Haemolysin coregulated protein is an exported receptor and chaperone of type VI secretion substrates. *Mol Cell*, 51(5):584–93, Sep 2013. doi: 10.1016/j.molcel.2013.07.025.

J Söding. Protein homology detection by HMM-HMM comparison. *Bioinformatics*, 21(7):951–60, Apr 2005. doi: 10.1093/bioinformatics/bti125.

F W Studier and B A Moffatt. Use of bacteriophage T7 RNA polymerase to direct selective high-level expression of cloned genes. *J Mol Biol*, 189(1):113–30, May 1986.

G Suarez, J C Sierra, T E Erova, J Sha, A J Horneman, and A K Chopra. A type VI secretion system effector protein, VgrG1, from *Aeromonas hydrophila* that induces host cell toxicity by ADP ribosylation of actin. *J Bacteriol*, 192(1):155–68, Jan 2010. doi: 10.1128/JB.01260-09.

K Sun, J E Bröms, M Lavander, B K Gurram, P-A Enquist, C D Andersson, M Elofsson, and A Sjöstedt. Screening for inhibition of *Vibrio cholerae* VipA-VipB interaction identifies small-molecule compounds active against type VI secretion. *Antimicrob Agents Chemother*, 58(7): 4123–30, Jul 2014. doi: 10.1128/AAC.02819-13.

S Thomas, I B Holland, and L Schmitt. The Type 1 secretion pathway - the hemolysin system and beyond. *Biochim Biophys Acta*, 1843(8):1629–41, Aug 2014. doi: 10.1016/j.bbamcr.2013.09.017.

K Uchida, P G Leiman, F Arisaka, and S Kanamaru. Structure and properties of the C-terminal beta-helical domain of VgrG protein from *Escherichia coli* O157. *J Biochem*, 155(3):173–82, Mar 2014. doi: 10.1093/jb/mvt109.

Y Uratani. A circular dichroism study of sheath contraction in pyocin R1. *Biochim Biophys Acta*, 703(2):196–203, May 1982.

Y Uratani and T Hoshino. Pyocin R1 inhibits active transport in *Pseudomonas aeruginosa* and depolarizes membrane potential. *J Bacteriol*, 157(2):632–6, Feb 1984.

M van Heel, G Harauz, E V Orlova, R Schmidt, and M Schatz. A new generation of the IMAGIC image processing system. *J Struct Biol*, 116(1):17–24, 1996. doi: 10.1006/jsbi.1996.0004.

P van Ulsen, S Rahman, W S P Jong, M H Daleke-Schermerhorn, and J Luirink. Type V secretion: from biogenesis to biotechnology. *Biochim Biophys Acta*, 1843(8):1592–611, Aug 2014. doi: 10.1016/j.bbamcr.2013.11.006.

I Ventre, A L Goodman, I Vallet-Gely, P Vasseur, C Soscia, S Molin, S Bleves, A Lazdunski, S Lory, and A Filloux. Multiple sensors control reciprocal expression of *Pseudomonas aeruginosa* regulatory RNA and virulence genes. *Proc Natl Acad Sci U S A*, 103(1):171–6, Jan 2006. doi: 10.1073/pnas.0507407103.

S Y Venyaminov, L P Rodikova, A L Metlina, and B F Poglazov. Secondary structure change of bacteriophage T4 sheath protein during sheath contraction. *J Mol Biol*, 98(4):657–64, Nov 1975.

A Walther-Mauruschat and F Mayer. Isolation and characterization of polysheaths, phage tail-like defective bacteriophages of *alcaligenes eutrophus* h 16. *J Gen Virol*, 41(2):239–54, Nov 1978.

B Webb and A Sali. Comparative Protein Structure Modeling Using MODELLER. *Curr Protoc Bioinformatics*, 47:5.6.1–5.6.32, 2014. doi: 10.1002/0471250953.bi0506s47.

J C Whitney, S Chou, A B Russell, J Biboy, T E Gardiner, M A Ferrin, M Brittnacher, W Vollmer, and J D Mougous. Identification, structure, and function of a novel type VI secretion peptidoglycan glycoside hydrolase effector-immunity pair. *J Biol Chem*, 288(37):26616–24, Sep 2013. doi: 10.1074/jbc.M113.488320.

J C Whitney, C M Beck, Y A Goo, A B Russell, B N Harding, J A De Leon, D A Cunningham, B Q Tran, D A Low, D R Goodlett, C S Hayes, and J D Mougous. Genetically distinct pathways guide effector export through the type VI secretion system. *Mol Microbiol*, 92(3): 529–42, May 2014. doi: 10.1111/mmi.12571.

S R Williams, D Gebhart, D W Martin, and D Scholl. Retargeting R-type pyocins to generate novel bactericidal protein complexes. *Appl Environ Microbiol*, 74(12):3868–76, Jun 2008. doi: 10.1128/AEM.00141-08.

B Wu, A Peisley, D Tetrault, Z Li, E H Egelman, K E Magor, T Walz, P A Penczek, and S Hur. Molecular Imprinting as a Signal-Activation Mechanism of the Viral RNA Sensor RIG-I. *Mol Cell*, 55(4):511–23, Aug 2014. doi: 10.1016/j.molcel.2014.06.010.

D Xu and Y Zhang. *Ab initio* protein structure assembly using continuous structure fragments and optimized knowledge-based force field. *Proteins*, 80(7):1715–35, Jul 2012. doi: 10.1002/prot.24065.

T Yamamoto. Presence of rhapidosomes in various species of bacteria and their morphological characteristics. *J Bacteriol*, 94(5):1746–56, Nov 1967.

G Yang, A J Dowling, U Gerike, R H ffrench Constant, and N R Waterfield. *Photorhabdus* virulence cassettes confer injectable insecticidal activity against the wax moth. *J Bacteriol*, 188(6):2254–61, Mar 2006. doi: 10.1128/JB.188.6.2254-2261.2006.

W Zhang, Sh Xu, J Li, X Shen, Y Wang, and Z Yuan. Modulation of a thermoregulated type VI secretion system by AHL-dependent quorum sensing in *Yersinia pseudotuberculosis*. *Arch Microbiol*, 193(5):351–63, May 2011. doi: 10.1007/s00203-011-0680-2.

X Y Zhang, Y R Brunet, L Logger, B Douzi, C Cambillau, L Journet, and E Cascales. Dissection of the TssB-TssC interface during type VI secretion sheath complex formation. *PLoS One*, 8 (11):e81074, 2013. doi: 10.1371/journal.pone.0081074.

J Zheng and K Y Leung. Dissection of a type VI secretion system in *Edwardsiella tarda*. *Mol Microbiol*, 66(5):1192–206, Dec 2007. doi: 10.1111/j.1365-2958.2007.05993.x.

J Zheng, B Ho, and J J Mekalanos. Genetic analysis of anti-amoebae and anti-bacterial activities of the type VI secretion system in *Vibrio cholerae*. *PLoS One*, 6(8):e23876, 2011. doi: 10.1371/journal.pone.0023876.

A Zoued, E Durand, C Bebeacua, Y R Brunet, B Douzi, C Cambillau, E Cascales, and L Journet. TssK is a trimeric cytoplasmic protein interacting with components of both phage-like and membrane anchoring complexes of the type VI secretion system. *J Biol Chem*, 288(38): 27031–41, Sep 2013. doi: 10.1074/jbc.M113.499772.

A Zoued, Y R Brunet, E Durand, M-S Aschtgen, L Logger, B Douzi, L Journet, C Cambillau, and E Cascales. Architecture and assembly of the Type VI secretion system. *Biochim Biophys Acta*, 1843(8):1664–73, Aug 2014. doi: 10.1016/j.bbamcr.2014.03.018.

6 Appendix

6.1 Cross-links detected by mass spectrometry

Table 6.1: Cross-links detected in XL-MS experiments and correlating Cα distances as deduced from the secondary structure model of the VipA/B protomer.

VipA	VipA'	VipB	VipB'	interprotomer ?	wild-type	VipA/VipBΔC^{209}	VipA/VipBΔC^{366}	distance [Å]
K10N		K403HB14		x	x			29.4
K10N		K213HB9					x	29.1
K10N		K220HB10					x	29.9
K10N		K291HB11					x	19.0
K10N		K100HB5				x	x	5.2
K16SA1		K223HB10					x	28.8
K16SA1		K213HB9					x	29.3
K16SA1		K291HB11					x	23.9
K16SA1		K75HB4				x		27.2
K16SA1		K100HB5				x		18.8
K16SA1	K10N					x	x	14.2
K41SA3-HA1		K377HB13		x	x			30.0
K41SA3-HA1		K100HB5				x		9.2
K41SA3-HA1	K10N					x	x	4.5
K59SA4-HA2		K291HB11					x	26.5
K59SA4-HA2		K100HB5				x	x	9.7
K59SA4-HA2	K10N						x	8.0
K59SA4-HA2	K16SA1					x	x	14.9
K59SA4-HA2	K41SA3-HA1					x		7.8
K72HA2-SA5	K59SA4-HA2					x	x	23.9
K72HA2-SA5	K41SA3-HA1					x	x	29.9
K72HA2-SA5	K10N					x	x	29.7
K78SA5		K40HB3					x	22.0

Table 6.1: Cross-links detected in XL-MS experiments and correlating Cα distances as deduced from the secondary structure model of the VipA/B protomer.

VipA	VipA'	VipB	VipB'	interprotomer ?	wild-type	VipA/VipBΔC^{209}	VipA/VipBΔC^{366}	distance [Å]
K78SA5		K100HB5				x		13.3
K78SA5	K41SA3-HA1					x	x	13.2
K78SA5	K16SA1						x	18.0
K78SA5	K10N					x	x	14.0
K78SA5	K59SA4-HA2					x	x	15.4
K80SA5-SA6	K41SA3-HA1					x		9.9
K80SA5-SA6	K10N					x		10.8
K80SA5-SA6	K72HA2-SA5					x		20.1
K96SA6-HA3	K72HA2-SA5						x	3.9
K114HA3	K78SA5						x	22.1
K115HA3		K41HB3				x	x	20.8
K115HA3		K75HB4				x	x	12.7
K115HA3	K59SA4-HA2					x	x	15.7
K115HA3	K41SA3-HA1					x	x	23.4
K115HA3	K16SA1						x	29.9
K115HA3	K10N					x	x	22.1
K115HA3	K78SA5					x	x	20.6
K115HA3	K152HA5					x	x	8.6
K115HA3	K80SA5-SA6					x	x	18.2
K115HA3	K72HA2-SA5					x	x	17.5
K127HA3		K40HB3					x	30.9
K127HA3	K127HA3						x	soluble dimer
K127HA3	K59SA4-HA2					x	x	21.9
K127HA3	K41SA3-HA1					x	x	25.7
K127HA3	K10N					x	x	21.6
K127HA3	K115HA3						x	18.7
K127HA3	K114HA3					x	x	20.2
K127HA3	K78SA5						x	26.1
K127HA3	K80SA5-SA6						x	24.3
K152HA3	K127HA3					x	x	17.9
		K74HB4	K100HB5			x		26.7
		K100HB5	K113SB1			x		16.0

Table 6.1: Cross-links detected in XL-MS experiments and correlating Cα distances as deduced from the secondary structure model of the VipA/B protomer.

VipA	VipA'	VipB	VipB'	interprotomer ?	wild-type	VipA/VipBΔC^{209}	VipA/VipBΔC^{366}	distance [Å]
		K213HB9	K223HB10				x	8.0
		K291HB11	K351SB8		x			14.7
		K291HB11	K366SB9-HB13	x	x			23.7
		K291HB11	K377HB13	x	x			22.1
		K291HB11	K213HB9				x	27.9
		K291HB11	K220HB10				x	25.0
		K291HB11	K223HB10				x	21.2
		K291HB11	K100HB5				x	21.1
		K291HB11	K113SB1				x	16.1
		K335HB12	K213HB9				x	18.9

6.2 Abbreviations

AAA+	ATPases associated with diverse cellular activities
Akt	protein kinase B
ATP	adenosine triphosphate
Bam	β-barrel assembly machine
CCD	charge-coupled device
ClpV	caseionlytic protease V (virulent strain)
ddH_2O	desalted water
dH_2O	distilled water
DNA	deoxyribonucleic acid
DTT	dithiothreitol
DotU	defect in organelle trafficking U
ECL	enhanced chemiluminescence
EDTA	ethylenediaminetetraacetic acid
EM	electron microscopy
ET	electron tomography
FSC	Fourier shell correlation
Gac(X)	global activator of antibiotic and cyanide production (X)
gp#	gene product #
HA	human influenza hemagglutinin

Hcp	haemolysin co-regulated protein
HRP	horseradish peroxidase
IcmF	intracellular multiplication F
Igl(X)	intracellular growth locus (X)
IHRSR	iterative helical real space refinement
kDa	kilo-Dalton
LB	lysogeny broth
LC-MS/MS	liquid chromatography tandem mass spectrometry
Ni-NTA	nickel nitrilotriacetic acid
OmpA	outer membrane protein A
PCR	polymerase chain reaction
PdpB	pathogenecity determinant protein B
PI3K	phosphatidylinositol-3-kinase
PpkA	polyphosphate kinase A
PppA	polyphosphate phosphatase A
retS	regulator of exopolysaccharide and type III secretion S
RpoN	alternative cofactor for RNA polymerase
rpm	revolutions per minute
Rsm(X)	regulation of secondary metabolites
SDS	sodium dodecyl sulfate
Sec	secretory
sRNA	small RNA
Tae	Type VI secretion amidase effector
Tat	twin-arginine translocation
TCA	trichloroacetic acid
Tde	Type VI secretion DNase effector
Tge	Type VI secretion glycoside hydrolase effector
Tle	Type VI secretion lipase effector
Vas(X)	virulence associated secretion X
VgrG	valine-glycine repeat G
VipA	ClpV-interacting protein A
VipB	ClpV-interacting protein B
XL-MS	cross-link mass spectrometry
YFP	yellow fluorescent protein
2YT	yeast-tryptone

6.3 Reprints

Figure 3.5 e:
Comparison of class averages and corresponding reprojections: reprinted from Cell Reports, Vol. 8 , Issue 1, S Kube, N Kapitein, T Zimniak, F Herzog, A Mogk, P Wendler, Structure of the VipA/B type VI secretion complex suggests a contraction-state-specific recycling mechanism, p. 20-30, Copyright 2014, with permission from Elsevier

Figure 3.7:
Analytical tryotic digest of VipA/B tubules: reprinted from Cell Reports, Vol. 8 , Issue 1, S Kube, N Kapitein, T Zimniak, F Herzog, A Mogk, P Wendler, Structure of the VipA/B type VI secretion complex suggests a contraction-state-specific recycling mechanism, p. 20-30, Copyright 2014, with permission from Elsevier

Figure 3.8 a, b and parts of c:
Localization of protein termini in VipA/VipB tubules: reprinted from Cell Reports, Vol. 8 , Issue 1, S Kube, N Kapitein, T Zimniak, F Herzog, A Mogk, P Wendler, Structure of the VipA/B type VI secretion complex suggests a contraction-state-specific recycling mechanism, p. 20-30, Copyright 2014, with permission from Elsevier

Figure 3.9 a:
Overlay of viral tail sheath protein structures: reprinted from Cell Reports, Vol. 8 , Issue 1, S Kube, N Kapitein, T Zimniak, F Herzog, A Mogk, P Wendler, Structure of the VipA/B type VI secretion complex suggests a contraction-state-specific recycling mechanism, p. 20-30, Copyright 2014, with permission from Elsevier

Figure 3.10 a:
Diffration pattern of T4 polysheath: reprinted from Journal of Molecular Biology, Vol. 25, Issue 2, M F Moody, Structure of the sheath of bacteriophage T4 I. Structure of the contracted sheath and polysheath, p. 167-174, Copyright 1967, with permission from Elsevier

Figure 3.11:
Predicted structure of the VipB N-terminus: reprinted from Cell Reports, Vol. 8 , Issue 1, S Kube, N Kapitein, T Zimniak, F Herzog, A Mogk, P Wendler, Structure of the VipA/B type VI secretion complex suggests a contraction-state-specific recycling mechanism, p. 20-30, Copyright 2014, with permission from Elsevier

Figure 3.12 b:
Topology diagrams of gp18 and VipA/B: reprinted from Cell Reports, Vol. 8 , Issue

1, S Kube, N Kapitein, T Zimniak, F Herzog, A Mogk, P Wendler, Structure of the VipA/B type VI secretion complex suggests a contraction-state-specific recycling mechanism, p. 20-30, Copyright 2014, with permission from Elsevier

Figure 3.13:

Predicted secondary structure profiles of VipA and VipB: reprinted from Cell Reports, Vol. 8 , Issue 1, S Kube, N Kapitein, T Zimniak, F Herzog, A Mogk, P Wendler, Structure of the VipA/B type VI secretion complex suggests a contraction-state-specific recycling mechanism, p. 20-30, Copyright 2014, with permission from Elsevier

Figure 3.14 d:

Inter- and intraprotein cross-links of VipB lysines K291 and K100: reprinted from Cell Reports, Vol. 8 , Issue 1, S Kube, N Kapitein, T Zimniak, F Herzog, A Mogk, P Wendler, Structure of the VipA/B type VI secretion complex suggests a contraction-state-specific recycling mechanism, p. 20-30, Copyright 2014, with permission from Elsevier

Figure 3.15:

Interprotomer contacts in contracted VipA/B tubules: reprinted from Cell Reports, Vol. 8 , Issue 1, S Kube, N Kapitein, T Zimniak, F Herzog, A Mogk, P Wendler, Structure of the VipA/B type VI secretion complex suggests a contraction-state-specific recycling mechanism, p. 20-30, Copyright 2014, with permission from Elsevier

Figure 3.16 d-f:

Localization of the interaction site of ClpV on the VipA/B tubule: reprinted from Cell Reports, Vol. 8 , Issue 1, S Kube, N Kapitein, T Zimniak, F Herzog, A Mogk, P Wendler, Structure of the VipA/B type VI secretion complex suggests a contraction-state-specific recycling mechanism, p. 20-30, Copyright 2014, with permission from Elsevier

Figure 3.17:

Comparison between contracted VipA/B tubules and T4 phage tail sheaths: reprinted from Cell Reports, Vol. 8 , Issue 1, S Kube, N Kapitein, T Zimniak, F Herzog, A Mogk, P Wendler, Structure of the VipA/B type VI secretion complex suggests a contraction-state-specific recycling mechanism, p. 20-30, Copyright 2014, with permission from Elsevier

Figure 3.18:
Protomer arrangement in the VipA/B tubule and the T4 sheath: reprinted from Cell Reports, Vol. 8 , Issue 1, S Kube, N Kapitein, T Zimniak, F Herzog, A Mogk, P Wendler, Structure of the VipA/B type VI secretion complex suggests a contraction-state-specific recycling mechanism, p. 20-30, Copyright 2014, with permission from Elsevier

Figure 4.2:
Mechanism for T6S tubule recycling: reprinted from Cell Reports, Vol. 8 , Issue 1, S Kube, N Kapitein, T Zimniak, F Herzog, A Mogk, P Wendler, Structure of the VipA/B type VI secretion complex suggests a contraction-state-specific recycling mechanism, p. 20-30, Copyright 2014, with permission from Elsevier